Computer simulation of simple and complex electrolyte solutions

by

Farhat Khurshid

B.Sc. (Hons), University of Calcutta, India, 2013
M.Sc., Indian Institute of Engineering Science and Technology, 2015

AN ABSTRACT OF A DISSERTATION

submitted in partial fulfillment of the requirements for the degree

DOCTOR OF PHILOSOPHY

Department of Chemistry
College of Arts and Sciences

KANSAS STATE UNIVERSITY
Manhattan, Kansas

2024

Abstract

The computer simulation of simple and complex electrolyte solutions is a powerful tool for understanding the behavior of ions in various environments, ranging from fundamental studies to practical applications. In these simulations, computational models mimic the behavior of ions in solution by considering their interactions with solvent molecules and other ions. Classical molecular dynamics simulations are often used for simple electrolyte solutions. These simulations provide insights into ion solvation, pairing, etc. In contrast, simulating complex electrolyte solutions, such as seawater, requires more effort. By elucidating the microscopic details of electrolyte solutions, computer simulations can aid in the design of new materials, the optimization of industrial processes, and provide fundamental advances in fields as diverse as electrochemistry, geochemistry, and biophysics.

This thesis is divided into two main parts. The first part involves the simulation of simple ionic solutions and the development of a classical force field for alkali metal nitrate and alkaline earth nitrate aqueous solutions. We adjust the charges on N and O atoms of the nitrate ion, along with Lennard-Jones parameters (σ and ϵ) to optimize the model. We then test the parameters by determining Kirkwood-Buff Integrals (KBIs) for a series of alkali and alkaline earth metal nitrates at various concentrations in water and comparing them to their experimental KBIs. Good agreement between the simulated and experimental KBIs was observed.

The second part of the thesis deals with more complex electrolyte solutions. We simulate 2 M pure alkali chloride aqueous solutions, together with mixtures of two 1 M alkali chloride aqueous

solutions, both placed between Au plates. The Au layers were either charged or uncharged. We could identify the preference of the different alkali metal ions for the charged Au plates that varies with the charge on the plates. The two main competing factors were the loss of the solvation shell and the effect of ion pair formation in the bulk solution. We also simulated a second set of complex electrolyte solutions. We compare and contrast the properties of regular seawater, Red Sea water, and Dead Sea water using a Kirkwood Buff theory approach. This was achieved by separating the KBIs into thermodynamic and charge neutralization contributions, which represents a new approach for the comparison of electrolyte solutions.

Computer simulation of simple and complex electrolyte solutions

by

Farhat Khurshid

B.Sc. (Hons), University of Calcutta, India, 2013
M.Sc., Indian Institute of Engineering Science and Technology, 2015

A DISSERTATION

submitted in partial fulfillment of the requirements for the degree

DOCTOR OF PHILOSOPHY

Department of Chemistry
College of Arts and Sciences

KANSAS STATE UNIVERSITY
Manhattan, Kansas

2024

Approved by:

Major Professor
Dr. Paul E. Smith

Copyright

Abstract

The computer simulation of simple and complex electrolyte solutions is a powerful tool for understanding the behavior of ions in various environments, ranging from fundamental studies to practical applications. In these simulations, computational models mimic the behavior of ions in solution by considering their interactions with solvent molecules and other ions. Classical molecular dynamics simulations are often used for simple electrolyte solutions. These simulations provide insights into ion solvation, pairing, etc. In contrast, simulating complex electrolyte solutions, such as seawater, requires more effort. By elucidating the microscopic details of electrolyte solutions, computer simulations can aid in the design of new materials, the optimization of industrial processes, and provide fundamental advances in fields as diverse as electrochemistry, geochemistry, and biophysics.

This thesis is divided into two main parts. The first part involves the simulation of simple ionic solutions and the development of a classical force field for alkali metal nitrate and alkaline earth nitrate aqueous solutions. We adjust the charges on N and O atoms of the nitrate ion, along with Lennard-Jones parameters (σ and ϵ) to optimize the model. We then test the parameters by determining Kirkwood-Buff Integrals (KBIs) for a series of alkali and alkaline earth metal nitrates at various concentrations in water and comparing them to their experimental KBIs. Good agreement between the simulated and experimental KBIs was observed.

The second part of the thesis deals with more complex electrolyte solutions. We simulate 2 M pure alkali chloride aqueous solutions, together with mixtures of two 1 M alkali chloride aqueous

solutions, both placed between Au plates. The Au layers were either charged or uncharged. We could identify the preference of the different alkali metal ions for the charged Au plates that varies with the charge on the plates. The two main competing factors were the loss of the solvation shell and the effect of ion pair formation in the bulk solution. We also simulated a second set of complex electrolyte solutions. We compare and contrast the properties of regular seawater, red sea water, and dead sea water using a Kirkwood Buff theory approach. This was achieved by separating the KBIs into thermodynamic and charge neutralization contributions, which represents a new approach for the comparison of electrolyte solutions.

Table of Contents

List of Figures

List of Tables

Acknowledgements

I would like to express my sincere gratitude to my major advisor, Dr. Paul E. Smith, for his endless guidance and support. Without his patience, it would not have been possible for me to obtain this degree.

I would like to extend my heartfelt thanks to my PhD committee members, Dr. Christine Aikens, Dr. Daniel Higgins, and Dr. Bret Flanders. Their guidance and suggestions have been crucial in shaping my PhD journey and I am truly grateful for them.

I would also like to thank the current and previous Smith group members, Dr. Nilusha Kariyawasam, Dr. Shin Suh, and Trust Ekama, for being awesome lab mates and sharing their knowledge and time with me. I would like to especially thank Dr. Elizabeth Ploetz for helping me with codes and for her invaluable suggestions and ideas, without which this PhD would not have been possible.

I would like to thank the Department of Chemistry at Kansas State University for giving me the opportunity to pursue a PhD. I would also like to thank the Office of Student Life for their support.

I would like to thank my friends from Manhattan for their love and endless support and for helping me keep my mind straight during one of the most difficult phases of my life. I never imagined getting such support here, thousands of miles away from my home.

I would like to thank my friends back in India, who have been a part of my journey through thick and thin.

Last but not the least, I would like to thank my parents, brother, and some special extended family members for their love, support, and belief in me.

Dedication

To my parents

Chapter 1 - Introduction

1.1. History of Computational Chemistry

Computer simulation plays a vital role in the development of Chemistry. Understanding molecular structures and dynamics to molecular docking, drug delivery, and predicting the properties of complex systems often involve computer simulations. Indeed, nowadays, computer simulation is often intertwined with experimental studies. In the 1950s, John Pople developed a method to predict the approximate electronic structures of molecules. Later, in 1998, John Pople 'for the development of computational models in quantum chemistry' and Walter Kohn 'for the development of density functional theory' received the Nobel Prize in Chemistry.[1] During a similar period (1959), the first molecular dynamics simulation of simple gases was performed by Alder and Wainright.[2] In 2013, the Nobel Prize in Chemistry was awarded to Martin Karplus, Michael Levitt, and Arieh Warshel 'for the development of multiscale models for complex chemical systems.'[3] They established the method of combining quantum mechanics with molecular mechanics (QM/MM). The development of QM/MM methods has allowed scientists to model large systems computationally.

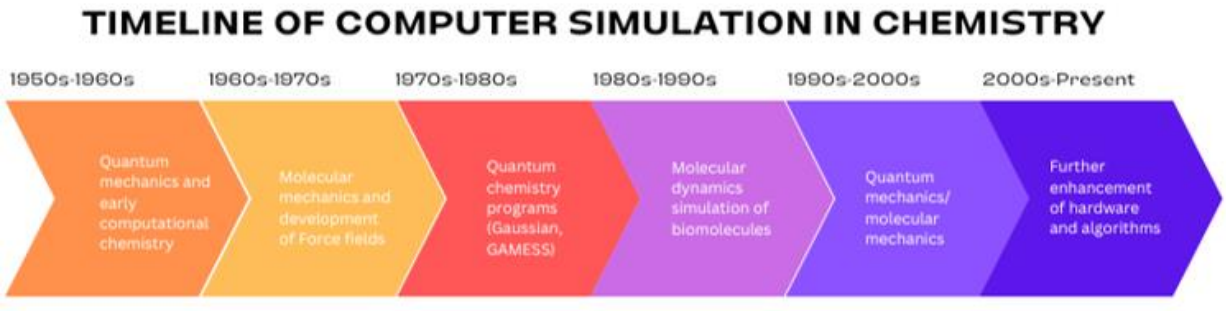

Figure 1.1.Timeline of computer simulation in Chemistry

In practice, different types of computer simulation methods are used depending on the various aspects of Chemistry being studied.[4,5]

1. Molecular Dynamics (MD) simulation[6] is used for studying the dynamics of molecules, understanding thermodynamic properties, and modeling biomolecular systems. It has applications in material science, biochemistry, and biophysics.
2. Monte Carlo (MC) simulation[7] in chemistry samples and generates representations of system configurations under certain thermodynamic conditions. It is useful for studying phase transition and several other thermodynamic properties.
3. Quantum mechanical calculations and density functional theory (DFT)[8] are used to calculate electronic structures and predict molecular properties.
4. Metadynamics[9] and other enhanced sampling approaches are used for sampling rare events and studying reaction pathways, transition states, conformational changes, etc.
5. Hybrid methods such as QM/MM[10], QM/MD, and ab initio MD[11] combine the strength of different techniques and help us to simulate complex molecular systems.

This thesis focuses on Molecular Dynamics simulation and its application to study electrolyte solutions.

1.2. Molecular dynamics simulation

1.2.1. Basics of molecular dynamics simulation

Molecular Dynamics (MD) simulation is a very useful tool for studying the dynamic behavior of atoms and molecules. Classical MD approaches treat only the atoms (not electrons) in a system and are popular for studying biological systems, as well as other applications in Material Science,

Chemistry, Physics, Engineering, etc. A simple MD simulation algorithm scheme is provided below.

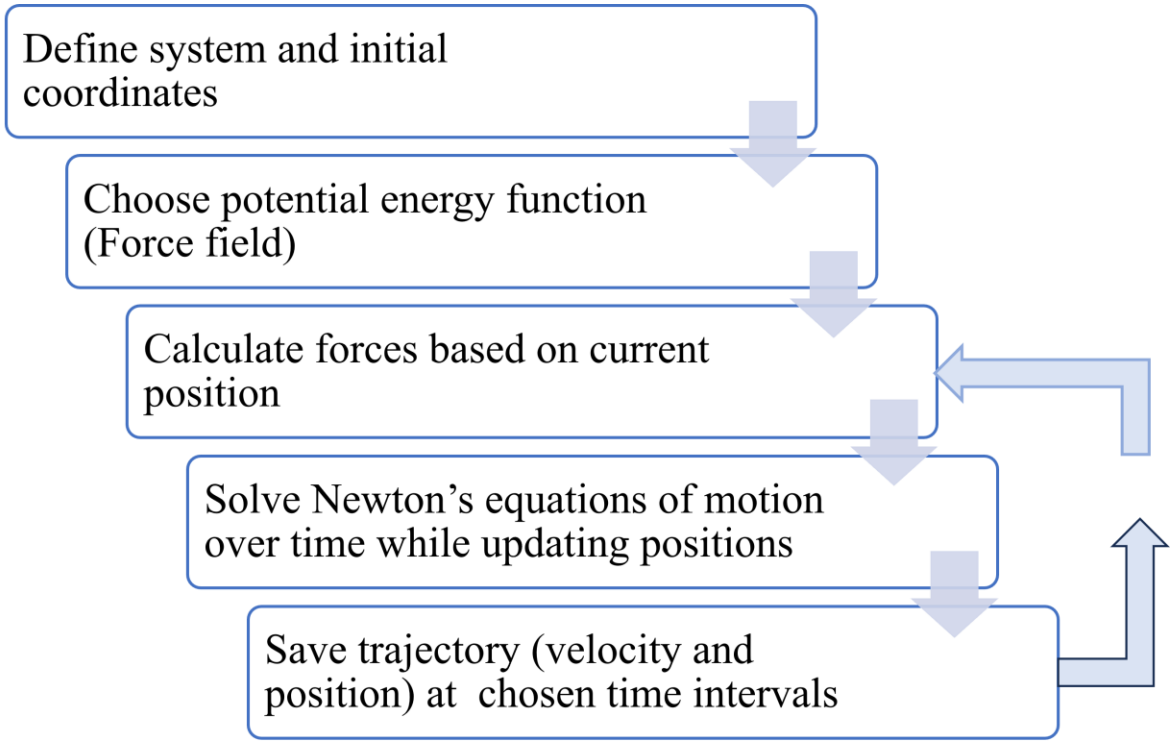

Figure 1.2. MD simulation algorithm

As shown in Figure 1.2, the first step in an MD simulation is to define the system of interest. Depending on what kind of MD simulation one wants to perform, the model system can be a united atom, all atom, or a mix of both. In the united atom approach nonpolar hydrogen atoms are considered as part of the atoms they are bonded to (usually a carbon atom). Initial coordinates can be generated based on experimental data such as crystal or NMR structures, or by assuming random initial positions. Random initial velocities are generated in the same manner. Then, the interaction energies and forces between the atoms have to be determined. These energies are generated from a collection of equations and parameters collectively known as a force field (a

detailed description of a force field will be given later). The MD simulation method involves solving Newton's equations of motion iteratively for successive small steps in time where the forces are recalculated at each point in time, resulting in trajectories (positions as a function of time) for each particle in the system. To do this accurately, numerical integration methods such as velocity-verlet or leapfrog, etc., are used.[12] The trajectories are saved at a chosen time interval, and the simulation time is extended as needed.

1.2.2. Role of classical mechanics in molecular dynamics simulation

Classical molecular dynamics simulations are based on classical mechanics. Atoms are considered to be hard spheres that follow Newton's equations of motion. Newton's second law of motion is,

$$F = ma \tag{1.1}$$

where F is the force on an atom, m is the atom mass, and a is the acceleration in a given direction (x, y or z). The force in a particular direction F_x is related to the potential energy U by,

$$F_x = -dU / dx \tag{1.2}$$

with similar equations for the other directions. Consequently,

$$v = \frac{dr}{dt} \tag{1.3}$$

$$a = \frac{dv}{dt} = \frac{F}{m} \tag{1.4}$$

as velocity (v) is the time derivative of the position, and acceleration (a) is the time derivative of the velocity. Equations 1.3 and 1.4 cannot be solved algebraically for systems consisting of more than two atoms. However, solving numerically using the finite difference method we find,

$$v_{i+1} = v_i + \delta t \; F(r_i) / m \tag{1.5}$$

$$r_{i+1} = r_i + \delta t \; v_i \tag{1.6}$$

where, δt is the time step between step *i* and step *i*+1. The initial configuration is then updated to a new one, new forces are then determined, and the whole process is repeated until the desired simulation time is reached.

1.2.3. Timestep and constraints

The total MD simulation time is divided into small discrete timesteps. The timestep determines the time between recalculating the forces on each atom required due to the movement of the atoms. The timestep depends on the properties of the system. It is usually on the order of femtoseconds (10^{-15} s). If the timestep is too small, the computational time required for a given simulation time will be longer, and the simulation will become inefficient. If the timestep is too long, important aspects of the dynamics will be missed. One approach to increase the timestep is to use constraint algorithms to maintain any bond lengths at a fixed value thereby removing the fastest degrees of motions. The equations of motion are then modified to use constraints using algorithms such as SETTLE, SHAKE, LINCS, etc.[4,5]

1.2.4. Conservation of energy and application of a thermostat and barostat

The total energy of a system is given by the Hamiltonian (*H*),

$$H = \sum_i \frac{p_i^2}{2m} + U \tag{1.7}$$

where the first term is the kinetic energy (*K*), and the second is the total potential energy (U). If these two energies do not depend explicitly on time then,

$$\frac{\partial H}{\partial t} = 0 \tag{1.8}$$

Hence, the total energy of the system remains constant, or energy is conserved. However, in practice it is often observed that the total energy increases slowly due to numerical errors (approximations). Specific measures must then be taken to keep the energy fixed and/or ensure a reasonable temperature is obtained. Furthermore, the final pressure is difficult to control as it depends strongly on the simulation density and quality of the force field. Additional approaches have been developed to control the pressure and temperature of an MD simulation. This is necessary for comparison to experiments that are often performed at constant pressure (P) and/or constant temperature (T).

Algorithms used to maintain a specific T are referred to as thermostats.[13–16] There are two ways to apply thermostats: velocity randomizing and velocity scaling.[17] Examples of the former include the Andersen,[18] and Stochastic dynamics algorithmns,[19] while examples of the latter include the Berendsen,[20] V-rescale,[21] and Nosé-Hoover algorithmns.[22,23] Maintaining a fixed system pressure is achieved by using a barostat.[15,16,20] The most popular examples are the Berendsen[20] and Parrinello-Rahman[24] barostats. The Berendsen barostat keeps the pressure fixed by scaling the box vectors and thereby changing coordinates. The Parinello-Rahman barostat allows each unit vector of the unit cell to vary independently, resulting in a change of both the box size and shape.[17]

1.2.5. Time averages and ensembles

The state of a microscopic system comprising N atoms can be described by 3N positions and 3N momenta. Together, these make a 6N dimensional space called phase space. In an MD simulation, the position and momenta of each atom change with time. Each point in phase space corresponds to a specific combination of position and momenta of the atoms in the system. These points are represented by Γ. A property of the system, such as A (for example, the potential energy), depends on Γ. With time, Γ changes, and so does $A(\Gamma)$. The macroscopic property of the system is then expressed as the time average of the corresponding microscopic property such that,

$$A_{obs} = \langle A \rangle = \langle A(\Gamma(t)) \rangle = \lim_{t_{obs} \to \infty} \int_0^{t_{obs}} A(\Gamma(t)) dt \tag{1.9}$$

It is often useful to remove time dependence. This is done using a hypothesis from statistical mechanics, known as the Ergodic hypothesis. This in turn connects the time averages from a computer simulation with ensemble averages that form the basis of statistical mechanics. According to this hypothesis, time averages can be replaced with ensemble averages, where an ensemble is a collection of systems corresponding to the points in phase space with the same macroscopic properties (such as volume and temperature). These points are distributed based on a normalized probability distribution $\rho(\Gamma)$. The ensemble average for the property A can be written as,

$$A_{obs} = \langle A \rangle_{ens} = \sum_{\Gamma} A(\Gamma) \rho_{ens}(\Gamma) \tag{1.10}$$

Each point in phase space has a different weight, $w(\Gamma)$. A normalization factor Q_{ens}, can be introduced, which is the sum over the states of the system. Q_{ens} is also known as the partition function. Thus,

$$\rho_{ens} = w_{ens}(\Gamma) / Q_{ens} \tag{1.11}$$

$$Q_{ens} = \sum_{\Gamma} w_{ens}(\Gamma) \tag{1.12}$$

$$\langle A \rangle_{ens} = \sum_{\Gamma} A(\Gamma) w_{ens}(\Gamma) / \sum_{\Gamma} w_{ens}(\Gamma) \tag{1.13}$$

The partition function Q_{ens} is related to thermodynamic potential, Ψ, as,

$$\Psi_{ens} = -\ln Q_{ens} \tag{1.14}$$

In MD simulation, there are four commonly used ensembles:

1. Microcanonical ensemble (NVE)
2. Canonical ensemble (NVT)
3. Isothermal-Isobaric ensemble (NPT)
4. Grand Canonical or Gibbs ensemble (μVT)

where N is the number of atoms, V is the volume, E is the internal energy, P is the pressure, T is the temperature, and μ is the chemical potential. The properties given in the parenthesis are kept constant in that ensemble. MD simulations can be performed in any of the above ensembles, although simulations in the Grand Canonical ensemble are difficult due to the required insertion/deletion of molecules.

1.2.6. Steps in a molecular dynamics simulation

A typical MD simulation involves three main stages: energy minimization, equilibration, and production.

1.2.6.1. Energy Minimization

Energy minimization involves relaxing the initial atomic positions to reduce steric clashes or unfavourable interactions in the system. It is mainly done using the steepest descent or the conjugate gradient method. These methods iteratively adjust the atomic positions to reduce the energy of the system until a set tolerance value of potential energy is reached. Different constraints can also be applied to maintain the molecular geometry.

1.2.6.2. Equilibration

In this step, the system is brought into equilibrium, in the chosen thermodynamic ensemble, by performing molecular dynamics and monitoring the energy, pressure, and other properties of the system until they no longer change with time. A thermostat and barostat can be applied during this stage.

1.2.6.3. Production

Production is the final step of an MD simulation. The simulation is extended to a specific time, and data is collected. This step also maintains the conditions based on the chosen ensemble. As this is a dynamic process, a trajectory is produced, which describes the motion of the molecules over time. This trajectory is then analyzed to study the properties of the system.

1.2.7. Periodic boundary condition

An essential part of the MD simulation is building the system. For the simulation of a finite-sized system, the system is represented by a virtual box, such as a cubic box. That means the system is limited by the box's surfaces or boundaries. In a real macroscopic system, 10^{23} molecules or atoms can be present. For example, at room temperature, 1 L of water contains $3.3x10^{25}$ molecules, among which up to ten layers of water molecules can interact with the surface. This includes around $2x10^{19}$ water molecules (only 0.00006% of the total number of water molecules).[25] The current MD simulations can only incorporate a few million molecules. In that case, the wall boundary assumption causes an exaggeration of surface effects. It occurs because of the larger ratio of the surface atoms to the total number of atoms. In an MD simulation, this can cause several artifacts. The use of periodic boundary condition (PBC) was introduced to solve this problem. The PBC concept assumes that a simulation box is surrounded by an infinite number of similar imaginary boxes or images in all three dimensions. The surface of the simulation boxes is open. When a particle leaves the system from one side, another similar particle, or an image of the particle, enters from the other side. Figure 1.3 demonstrates the application of PBC in a 2D system.[26] The main simulation box is shown to be surrounded by its imaginary replicas. The minimum image convention is applied, i.e., any particle interacts with its nearest image as determined by the PBC. A cut-off distance is set beyond which the interactions are not calculated. It is done so that a particle does not see or interact with its replica twice. The contributions from molecules beyond the cut-off radius are not calculated. It is acceptable for the bonded interactions, as those are short-range interactions. But for non-bonded interactions, this process is inaccurate. Non-bonded interactions are long-range forces that still have a significant contribution at a larger distance. The Coulombic interaction, which is the interaction between charged (and polar)

particles, is treated using the Ewald method.[27] This method computes the interaction between all charged particles in the simulation box and the particles in their periodic images without the use of cutoffs.

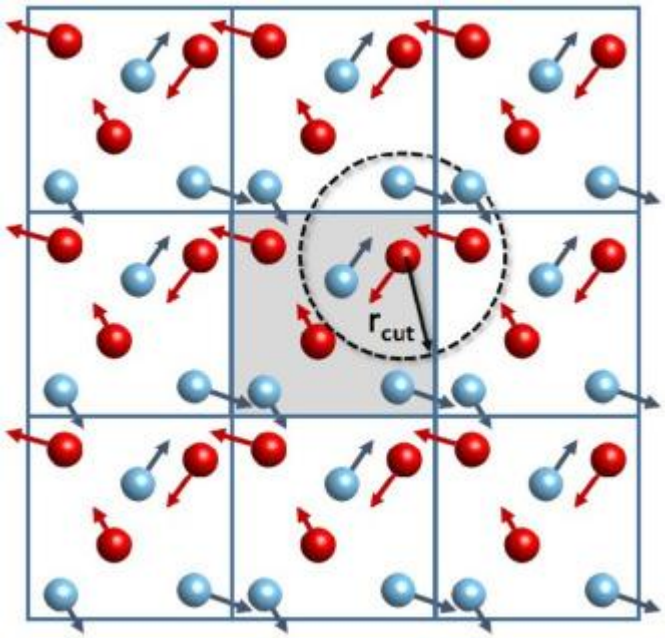

Figure 1.3. A main simulation box surrounded by its replicas applying PBC[25]

The Ewald method splits the electrostatic potential into two contributions. The short-range contribution is treated in real space, while the long-range contribution is calculated in reciprocal space or k-space. Although this method gives very accurate results, it can be computationally expensive. An improvement of this method is Particle Mesh Ewald (PME).[28] In PME, the charge is distributed on a mesh. This method eliminates the need to use cut-offs, thereby eliminating artifacts generated by cut-offs.

1.2.8. Advantages and limitations of molecular dynamics simulation

MD simulation is a powerful tool for research at the atomic and molecular levels for several complex systems. Like any other theoretical or experimental procedure, it has advantages and limitations.[29]

The advantages are:

i. It only requires atomic and intermolecular parameters for simulation.
ii. Temperature and pressure effects can be included and studied.
iii. Complex systems, such as polymers, proteins, and many other biomolecules, can be studied at the atomic level.
iv. MD simulations can predict various thermodynamic properties, structural characteristics, and dynamic behavior.
v. MD simulations allow observation of molecular processes in real-time, which may be challenging to study experimentally.

Limitations of MD simulation include:

i. Time and size scales: MD simulation can be computationally expensive for large systems and long simulation times. Even with powerful computational resources, 2.1 milliseconds is the longest simulation length achieved.[30]
ii. Force field accuracy: The accuracy of MD simulation depends on the accuracy of the force field. Force fields are inherently approximate as they only estimate the forces between atoms/molecules when calculating the potential energy.

iii. Dependence on classical mechanics: MD simulation follows the rules of classical mechanics, neglecting quantum effects. Chemical bond breaking or formation, presence of hydrogen bonds, etc., cannot be simulated using MD alone.

iv. Hardware: Computer hardware is crucial in running MD simulations. GPUs are used extensively to reduce computational time. However, parallelization with multiple GPUs still needs to be solved.

1.2.9. Applications of molecular dynamics simulation

Molecular dynamics is a powerful computational tool with applications in chemistry, biochemistry, physics, material science, etc. Some notable applications are listed below.

i. Biomolecular systems: MD simulations are used to study the structure and dynamics of biomolecular systems. Protein folding, protein-ligand interactions, lipid bilayers, membrane proteins, enzyme catalysts, etc., can be analyzed using MD simulation. Cellular processes, such as ion transport through ion channels, can be studied using MD simulation.

ii. Material science: Mechanical properties of materials, such as strength, elasticity, deformation behavior, etc., can be studied using MD simulations.

iii. Polymers: Conformation of polymers, phase transitions, and other mechanical properties of polymers are studied using MD simulations.

iv. Electrochemistry: MD simulations are used to study the properties of ions and molecules in electrolytic systems. It provides information about the electrochemical processes.

v. Drug design and discovery: MD simulations can predict the binding affinity of drug molecules to their targets, thus playing a crucial role in drug design and discovery.

vi. MD simulations have applications in supramolecular chemistry, environmental chemistry, nanotechnology, and many other parts of chemistry.

vii. Experiment validation: MD simulations are used to validate structures obtained from X-ray crystallography, cryo-electron microscopy, etc.

1.2.10. Molecular dynamics software

Many software packages are widely available and used by the scientific community for MD simulation. Some of the most common ones and their primary applications are given below.

i. GROMACS (GROningen MAchine for Chemical Simulations)[31]: Biomolecular simulations, small organic molecules, materials science.

ii. AMBER (Assisted Model Building with Energy Refinement)[32]: Biomolecular systems, other macromolecules.

iii. CHARMM (Chemistry at HARvard Macromolecular Mechanics)[33]: Biomolecular simulation, complex molecular systems.

iv. NAMD (Not Another Molecular Dynamics program)[34]: Biomolecular simulation, simulation on large-scale systems, highly parallelizable.

v. LAMMPS (Large-scale Atomic/Molecular Massively Parallel Simulator)[35]: Materials simulation, polymers, biological systems, granular materials.

vi. Desmond[36]: Drug discovery and development

vii. OpenMM[37]: General MD simulations, highly customizable.

viii. Schrodinger Suite: Drug discovery, quantum mechanics/molecular mechanics (QM/MM) simulation.

Due to its unrivaled speed, performance-centric optimization, and application in biomolecular and materials science, GROMACS is our choice of software.

1.3. Force fields for molecular dynamics simulation

The accuracy of MD simulations or molecular mechanics (MM) methods is highly dependent on the accuracy of the force field. A force field is a set of parameters and equations describing the potential energy of a system. The central assumption of any MM method is the Born-Oppenheimer approximation. This approximation allows the separation of nuclear motion and electronic motion. Due to their light weight, the electrons move much faster than the nuclei of a molecule and rapidly adjust to any changes in the nuclei. The electrons are supposed to be in their electronic ground state at each nuclear configuration. Therefore, the energy of a system can be written as a function of the nuclear coordinates only.[38]

According to classical mechanics, the total energy is divided into two terms: kinetic energy and potential energy. Kinetic energy (K) can be calculated easily using the atoms' mass (m) and velocity (v),

$$K = \sum_i \frac{1}{2} m v^2 \tag{1.15}$$

The potential energy (U) is the sum of bonded and non-bonded terms for classical pairwise additive force fields,

$$U(r) = U_{bond} + U_{angle} + U_{dihedral} + U_{improper} + U_{electrostatic} + U_{vdw} \tag{1.16}$$

The first four terms are the bonded, and the last two are the non-bonded terms. The energy is written as a function of the atomic coordinates. There are several different ways of representing each term of equation 1.16. The most common ones are given below,

$$
\begin{aligned}
U_{bond} &= \sum_{bond} \frac{1}{2} k_b (r - r_0)^2 \\
U_{angle} &= \sum_{angle} \frac{1}{2} k_\theta (\theta - \theta_0)^2 \\
U_{\substack{proper \\ dihedral}} &= \sum_{torsion} k_\phi [1 + \cos(n\phi - \delta)] \\
U_{\substack{improper \\ dihedral}} &= \sum_{improper} \frac{1}{2} k_\phi \left(\phi - \phi_0\right)^2 \\
U_{vdw} &= \sum_{i,j} 4\varepsilon \left[\left(\frac{\sigma}{r} \right)^{12} - \left(\frac{\sigma}{r} \right)^{6} \right] \\
U_{electrostatic} &= \sum_{i,j} \frac{q_i q_j}{4\pi\varepsilon_0 \varepsilon_r r}
\end{aligned}
\tag{1.17}
$$

In the above equations, k_b is the bond force constant and r_0 is the equilibrium bond length. k_θ is the angle constant and θ_0 is the equilibrium angle. For the proper dihedral term k_ϕ is the force constant, n is the multiplicity, ϕ is the dihedral angle and δ is the phase shift. In the improper dihedral term k_ϕ is the improper dihedral constant and ϕ_0 is the equilibrium improper dihedral. The last two terms are the non-bonded terms. The first is van der Waals (vdw) contribution and the second is the electrostatic interaction. For the vdw term, ε determines interaction strength between the two atoms and σ represents the size parameter or contact distance between the two atoms. For the last term q_i and q_j are partial atomic charges on the atoms *i* and *j*, while ε_0 is the permittivity of vacuum, ε_r is the relative permittivity of the system, and r is the distance between two atoms. A visual representation of the different interactions is given in Figure 1.4.[39]

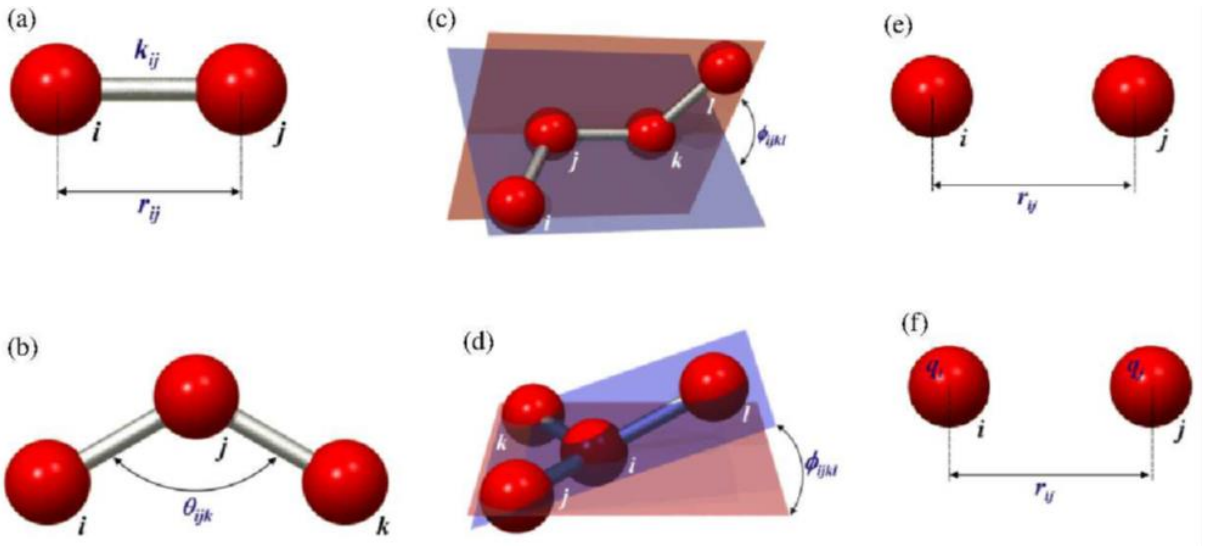

Figure 1.4. Schematic representation of the (a) bond, (b) angle, (c) proper torsion, (d) improper-dihedral angle, (e) van der Waals interaction, and (f) electrostatic interaction.[39]

The parameters for each of these terms can be obtained from either simulation or experiment. The value of r_0, θ_0 and ϕ_0 can be obtained from X-ray crystallography data, while k_b, k_θ and k_ϕ are often obtained from spectroscopic (IR, NMR) data. There is little experimental data available for determining k_ϕ, n and δ. Therefore, these are taken from quantum mechanical (QM) calculations. The charges on the atoms are not known, so those are usually taken from gas phase QM calculations, and then scaled to include polarization effects that occur in the condensed phase (especially for polar solvents). Equation of state data can be used to determine σ and ε of the van der Waals interaction equation. Usually, σ_{ii} and ε_{ii} are known for the interaction between pairs of *i* atoms. The interatomic van der Waals interactions between pairs of *i* and *j* molecules are calculated using the combination rules. Different force fields use different combination rules. The two most common ones are Lorentz-Berthelot or arithmetic combination rules and the geometric combination rules. The arithmetic combination rules are given by,

$$\sigma_{ij} = \frac{\sigma_{ii} + \sigma_{jj}}{2}$$
$$\varepsilon_{ij} = \sqrt{\varepsilon_{ii}\varepsilon_{jj}} \tag{1.18}$$

while the geometric combination rules are given by,

$$\sigma_{ij} = \sqrt{\sigma_{ii}\sigma_{jj}}$$
$$\varepsilon_{ij} = \sqrt{\varepsilon_{ii}\varepsilon_{jj}} \tag{1.19}$$

There are several force fields available specializing in different types of systems. Some examples of common force fields with their application areas are given below.

i. AMBER[40]: Proteins, nucleic acids, small organic molecules
ii. CHARMM[41]: Proteins, nucleic acids, lipids, carbohydrates
iii. GROMOS[42]: Biomolecules, organic compounds
iv. KBFF and KBFF20[43,44]: Biomolecules, materials
v. OPLS[45]: Organic compounds, peptides, proteins
vi. COMPASS[46]: Organic compounds, polymers, materials
vii. LAMMPS Force Fields[47]: Biomolecules, materials, polymer
viii. ReaxFF[48]: Reactive systems, combustion reactions, chemical transformation
ix. MARTINI[49]: Coarse-grained simulations for large biomolecular systems
x. AMOEBA[50]: Polarizable force field

1.4. Building a force field

1.4.1. A historical background

Although the first molecular mechanics calculations were done in the 1940s[51] significant progress in force field (FF) development was not made until after computers became available in the 1960s. The pioneers in this area were Shenior Lifson (Weizmann Institute, Israel), Harold Scheraga (Cornell University, USA), and Norman Allinger (Wayne State and University of Georgia, USA).[38] The first FF was built to reproduce the structure, properties, and vibrational spectra of some organic molecules in 1968.[52] Later, in the mid-1970s, the first atomistic simulation of protein,[53] the first coarse-grained model,[54] and the first QM/MM[10] simulations were performed. After that, the area of FF development became consistent. FF development has been a massive area of research since then.

An important part of FF development is deciding whether to include polarization in an explicit manner or not. Polarization effects in molecular dynamics simulations involve changes in the distribution of charges within molecules or materials that may occur during the simulation due to changes in the external electric fields surrounding molecules. These effects play an important role in accurately modeling atomic and molecular interactions, especially in cases where nearby charges, such as polar molecules like water, are present or external electric fields cause charge redistribution. There are different methods for accounting for the effects of polarizability in a simulation. In a polarizable force field, this is done by adding explicitly polarizable sites or allowing atomic charges to fluctuate.[55,56] All atom polarizable force fields capture the effects of polarizability well, but these are computationally expensive. In a non-polarizable force field, the

charges are scaled to produce effective fixed charges, which attempt to implicitly capture the polarization effect.[57] However, this method may not capture the important electronic structural details of the system.

Other approximations can be used to enhance the computational efficiency of MD simulations and therefore extend the approach to larger system sizes. A technique to simulate a micron-scale system without the large computational cost was developed by Rudd and Broughton: coarse-grained molecular dynamics (CGMD).[58] The CGMD equations of motion are derived directly from finite temperature MD through a statistical coarse-graining procedure, so they agree with MD as the mesh size is reduced to the atomic scale. The use of efficient CGMD allows for atomistic simulation of significantly larger systems compared to MD alone. CGMD models consist of interacting mass points (CG beads) that correspond to a group of atoms in an atomistic simulation of the same system. They can thus be viewed as relatively low-resolution models, compared to more detailed atomistic models. The challenge in CGMD lies in determining the appropriate level of detail to capture the essential chemistry of the system while still simplifying it enough to make computations tractable.

1.4.2. Force field development process

Some basic steps are involved in generating a new force field. The steps are described below.[59]

1. Selecting the function to model the system energy: How to describe intramolecular interactions, whether to add polarization explicitly, what form of the van der Waal's equations to use, etc., needs to be determined first.

2. Choose the data set required to determine all the parameters needed in the previously selected function, such as equilibrium bond lengths obtained from x-ray or neutron diffraction, force constants from vibrational spectroscopy, heats of sublimation or vaporization, densities, etc. Use ab initio or quantum calculations when experimental data are scarce.
3. Parameter optimization: When a large number of parameters are involved, they are often refined in stages as most of them are interconnected, meaning that a change in one value may affect some other parameter. Therefore, optimization becomes an iterative procedure. An alternative approach is using a least-squares fitting to determine the entire set of parameters that best agree with the input information. A new and attractive approach is the force-matching method, which directly provides the potential energy surface derived from QM calculations.
4. Validation of force field: It is essential to validate the final set of parameters by computing the properties of systems that were not used in the parametrization process.

1.4.3. Difficulties of current force field development processes

Developing a FF is not a trivial job. Several underlying challenges make this task complex and time-consuming. Some of the difficulties encountered during the process of FF development include:

1. The scarcity of experimental data.
2. No standard way of parameterization is known.
3. Trying to mimic condensed phase polarization by simply scaling charges does not work. For example, water in the gaseous phase will be less polarized than in the condensed phase.

Thus, it will polarize the other polar molecules in the system more than the gaseous phase. Therefore, the charges applicable in the gaseous phase do not work for the condensed phase.

Recently, our group has employed Kirkwood-Buff theory in an attempt to increase the quantity of relevant condensed phase data that can be used to develop accurate FF parameters. These Kirkwood-Buff-derived force fields involve a focus on the development of improved partial atomic charges as well as the changes to the Lennard-Jones (LJ) parameters (σ and ϵ).

1.5. Kirkwood-Buff theory

1.5.1. Introduction to Kirkwood-Buff theory

First published in 1951 by John G. Kirkwood and Frank P. Buff, Kirkwood-Buff (KB) theory is an exact statistical mechanics theory that relates solution structure (a microscopic property) to the solution thermodynamics (a macroscopic property).[60] KB theory uses properties of the grand canonical ensemble, where the chemical potential (μ), volume (V), and temperature (T) are fixed, to describe the thermodynamics of open, semi-open and closed systems. The central part of the KB theory is the KB integrals (KBI). The KBIs are defined as,

$$G_{\alpha\beta} = G_{\beta\alpha} = 4\pi \int_0^\infty [g_{\alpha\beta}(r) - 1]\ r^2 dr \tag{1.20}$$

where $g_{\alpha\beta}$ is the radial distribution function (RDF) or pair correlation function between two species α and β, separated by a distance r. The KBI represents the net affinity between two species in the

system. A positive KBI value indicates the net interaction is favorable, and a negative value indicates the net interaction is not favorable between two species.

It is crucial to calculate the RDFs correctly as their integral is required to calculate the KBIs. In statistical mechanics, the RDF is defined as the change in local density of a species surrounding another species in the system, with respect to distance *r*. In other words, it is the probability of finding a particular species at a distance *r* from a reference species. A visual representation depicting the concept behind RDF is provided in Figure 1.5. In Figure 1.5, the red particle is the reference species. The RDF determines the number of other species between r and r + dr.

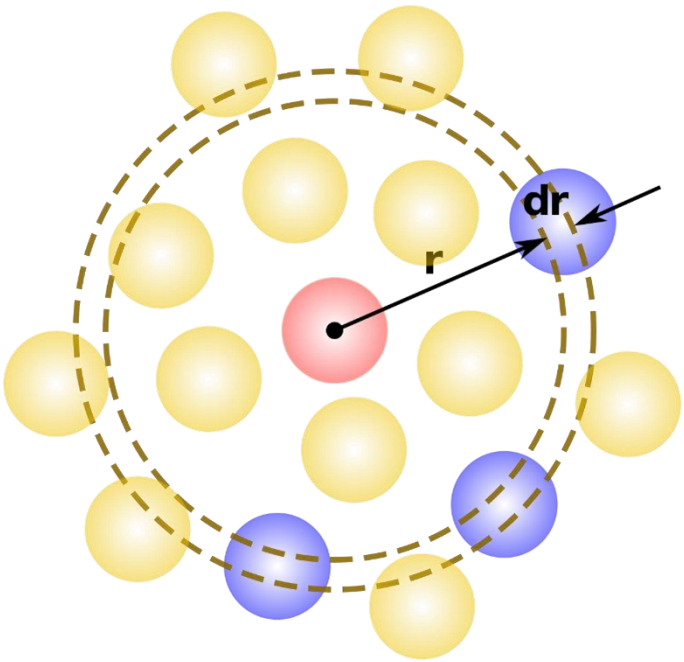

Figure 1.5. Illustration of an RDF[61]

Although KB theory was published in 1951, it was not until 1977 that it became famous after Ben-Naim published an inversion of the KB theory.[62] During the 1950s, there was no experimental way

of calculating RDFs, and even the computers were not advanced enough to provide examples. In 1977, Ben-Naim used experimental data to calculate experimental KBI values. In 2003, the Smith Group started to used KB theory and the KB inversion technique to build a new force field (KBFF) for urea and water.[63] No other computational studies in previous literature displayed the correct urea and water mixture behavior. In the KBFF model, a hybrid charge distribution that reproduced the KBIs accurately over a range of concentrations was discovered. As a result, the solution thermodynamics, including the activity of urea, were well-described. The model also reproduced other physical properties, such as the density, diffusion constants, and compressibility. In agreement with experimental data, the model showed little or no urea self-aggregation. The ideal nature of urea mixtures on a molar activity scale seemed to result from a balance between water-water and urea-water interactions, with a smaller urea-urea interaction. Although initially developed for use with SPC/E water, the new model performed equally well with the SPC and TIP3P water models.

1.5.3. Advantages and disadvantages of Kirkwood-Buff theory

There are certain advantages and disadvantages associated with using KB theory for FF development. The advantages are:[64]

i. It is an exact statistical mechanical theory, meaning no approximations are involved.
ii. It applies to any solution mixture containing any number of components, as long as those are miscible.
iii. It can be applied to molecules of any size and complexity.
iv. Pairwise additivity of interactions is not assumed in this theory.

v. It is well suited for computational studies.

Some disadvantages of using a KB theory approach include:

i. Longer simulations and larger system sizes are required to obtain KBIs.

ii. RDFs of open systems are required to calculate KBIs. But typically, RDFs of closed and finite systems are obtained from simulations. Therefore, further corrections are needed.[65]

iii. For macromolecules that are too large, difficulties may arise.

1.5.3. Inversion of KB theory

In 1977, Arieh Ben-Naim suggested a new approach to using KB theory. Instead of using KBIs to describe thermodynamic properties, he proposed to use experimental thermodynamic properties to extract experimental KBIs.[66] This approach provides valuable information about the mixing behavior of solutions. The KB inversion equation for a binary solution is expressed as,

$$\delta_{\alpha\beta} + \rho_\beta G_{\alpha\beta} = \rho_\beta RT\kappa_T + \frac{1}{x_1 x_2}.\frac{x_\beta}{x_\alpha}.\frac{(1-\rho_\alpha \bar{V}_\alpha)(1-\rho_\beta \bar{V}_\beta)}{(\partial\beta\mu_\alpha / \partial x_\beta)_{T,P}} \tag{1.21}$$

where, $\delta_{\alpha\beta}$ is the Kronecker delta, ρ_β is the number density, R is the ideal gas constant, T is the temperature, κ_T is the isothermal compressibility, x_α is the mole fraction of species α and x_β is the mole fraction of the species β. $\bar{V}_\alpha$ and $\bar{V}_\beta$ are partial molar volumes of α and β, respectively. Finally, $(\partial\beta\mu_\alpha / \partial x_\beta)_{T,P}$ is the derivative of the chemical potential. Thus, we need to know only three pieces of experimental data: the isothermal compressibility, partial molar volume as a function of composition, and a derivative of chemical potential (activity) as a function of

composition. Using these three composition dependent values in equation 1.21, we can obtain KBIs as a function of composition.

1.6. Kirkwood-Buff theory developed force field (KBFF)

As mentioned in section 1.5.1, in 2003, the Smith Group used the KB theory and the KB inversion technique to build a new force field (KBFF) for urea and water mixture.[63] Since then, a tremendous amount of work has been performed to develop improved KBFF model for a series of small solutes. The most recent work was published in 2021, which described a complete FF for peptides and proteins. The FF was named KBFF20.[44] The method of development of KBFF models is illustrated in Figure 1.6.

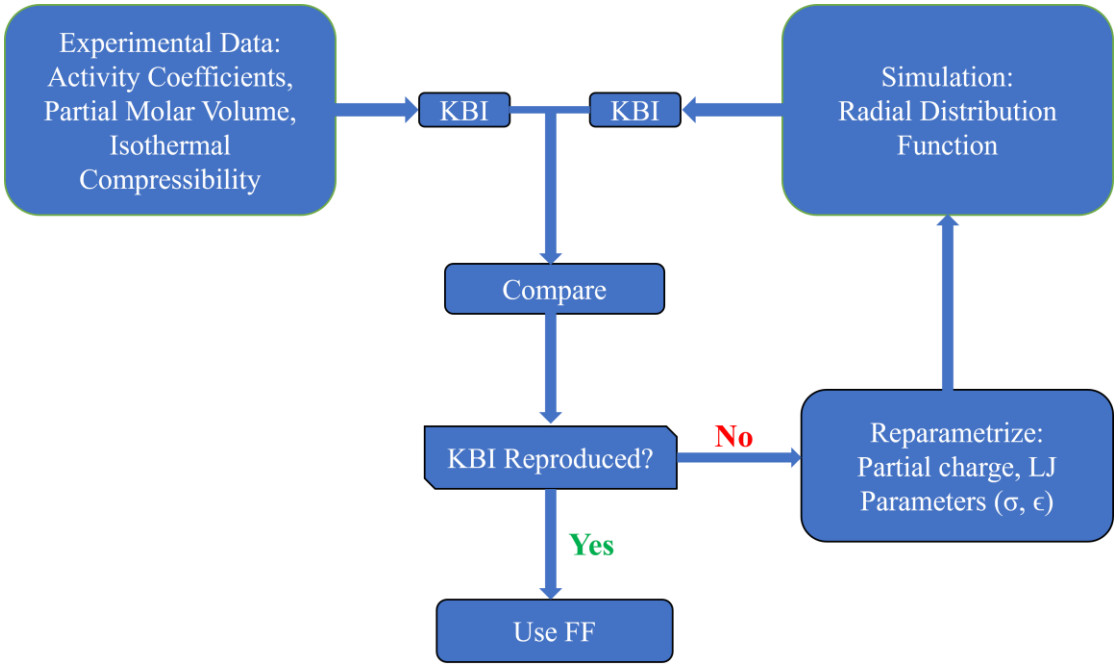

Figure 1.6. Flowchart for the method of development of KBFF

1.6.1. Extracting KBIs from experimental data

The first step for developing a KBFF model is to obtain KBIs from the corresponding experimental data. We need isothermal compressibility, partial molar volume or density as a function of composition, and the chemical potential (activity) as a function of composition. The isothermal compressibility data is often not available. In that case, the isothermal compressibility can be assumed to be,

$$\kappa_T = \varphi_1 \kappa_{T_1}^0 + \varphi_2 \kappa_{T_2}^0 \tag{1.22}$$

where 1 represents the solvent and 2 represents the solute. $\kappa_{T_1}^0$ is the compressibility of the pure solvent and $\kappa_{T_2}^0$ is the compressibility of the pure solute. φ represents the volume fraction. Fortunately, the quality of the compressibility data does not significantly affect the final KBI values. The general method for obtaining partial molar volumes (PMVs) is to fit the density versus composition data. If density data is unavailable, then the density of pure solute crystal and pure solvent density can be used to determine the PMV, which is then assumed to be independent of composition.[67] The most important data is the activity data.[43] It can be obtained from phase equilibria or osmotic pressure studies. For systems that have low solubility, the activity data might be limited or not available at all. In that case, those systems cannot be studied using KBFF approach.

1.6.3. Obtaining KBIs from MD simulations

KB theory is set up in the Grand Canonical Ensemble (μVT constant), which is an open system. Therefore, particle numbers can fluctuate to keep the chemical potential constant. It is challenging to perform MD simulations in an open system. Most MD simulations are done in the Gibbs Ensemble (NPT constant). In that case, the equation for the KBI can be modified to,[60]

$$G_{\alpha\beta} = 4\pi\int_0^R [g_{\alpha\beta}(r) - 1]r^2 dr \tag{1.23}$$

where *R* is the integration distance. The integration distance needs to be large enough that no "structure" remains in the RDF, but small enough that the closed NPT system can act as a particle bath for the smaller open system defined by *R*.

Using LJ parameters (σ, ϵ) and partial charge values (available or parametrized), an MD simulation can be performed, the RDFs can then be generated and integrated to give KBI values. An example of the conversion of RDFs into KBIs is given in the Figure 1.7.[43] The top panel shows simulated RDFs for an N-methylacetamide (NMA) and water system. The bottom panel shows corresponding KBIs.

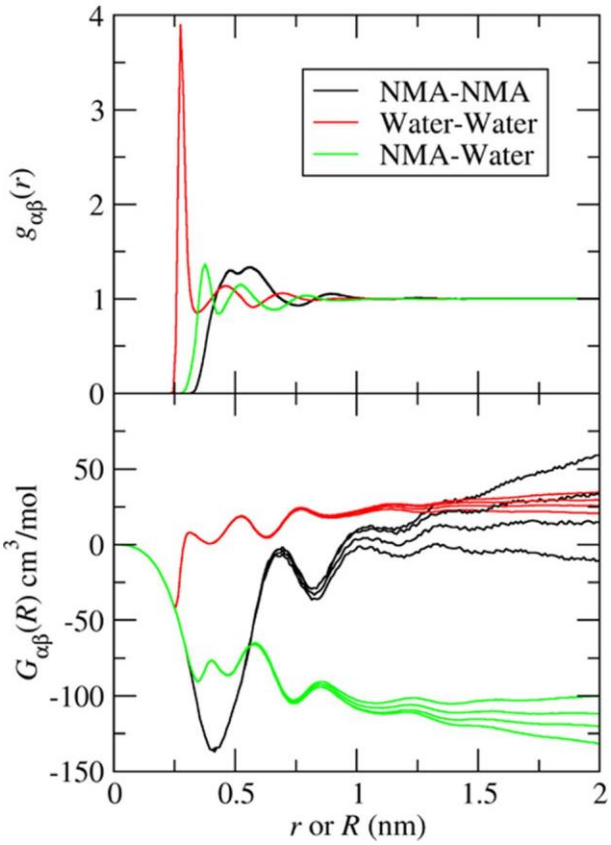

Figure 1.7. Simulated RDFs and its conversion to KBIs[43] for NMA+water system at 313K and 1 bar. In the bottom panel, each line of the same color represents different time averages

Another method of calculating KBIs was established by Hill and Schnell.[68,69] They investigated the finite-size scaling of small nonperiodic systems embedded in a large periodic reservoir. The reservoir was simulated in the grand canonical ensemble (μVT). The macroscopic thermodynamic properties were extracted by considering the scaling of the small system properties with the system size. Both methods described above have advantages and limitations. However, the common problem in both processes is ambiguity in determining the KBI analysis region. Ploetz et al. have provided a good comparison of the results from both processes.[70] They generally agree for large system sizes.

1.6.4. Comparing experimental and simulated results and validating FFs

Once the KBIs are obtained from the MD simulation, they can be used to compare them with the experimental KBIs and calculate other thermodynamic properties using equation 1.24 and compare them to their experimental values. The PMVs and an activity derivative are given by,

$$\begin{aligned} \bar{V}_1 &= \frac{1+\rho_1(G_{22}-G_{12})}{\eta} \\ \bar{V}_2 &= \frac{1+\rho_2(G_{11}-G_{12})}{\eta} \\ \eta &= \rho_1+\rho_2+\rho_1\rho_2(G_{11}+G_{22}-2G_{12}) \\ a_{cc} &= \left(\frac{\partial \ln a_c}{\partial \ln \rho_c}\right)_{P,T} = \frac{1}{1+\rho_2(G_{22}-G_{12})} \end{aligned} \tag{1.24}$$

for binary mixtures.

1.7. KBFF for aqueous alkali and alkaline earth nitrates

Alkali and alkaline earth nitrates are interesting materials to study because of their wide range of applications in chemistry, biology, therapeutics, environmental science, industry, etc. In previous studies by our group parameters for alkali metal and alkaline earth metal ions were developed as a part of KBFF.[71,72] Those ions were paired with halide ions. To make the KBFF applicable in a wide range of computational studies, one needs parameters for all commonly available ions and molecules. In the current thesis, the development of a nitrate ion FF, compatible with existing KBFF models, is discussed. Although the nitrate ion has an overall charge of -1, the partial charges on N and O atoms are unknown. Also, the LJ parameters (σ and ϵ), which correctly define the interaction between the solute and solvent ions, have not been published yet. These issues make

the task of modeling nitrate ions difficult. For instance, in a recent study an alkali nitrate FF was developed.[73] But, after testing, it showed significant aggregation for KNO_3 molecules at 1 m concentration. In our research, we have extensively tested different partial charges on N and O atoms and different LJ parameters in an attempt to obtain the correct interaction between solvent and ions. The values obtained are then tested against other physical properties to validate the results. Ultimately, we successfully built a FF for aqueous alkali and alkaline earth nitrate solutions.

1.8. Studying the effects of local electroneutrality on mixed electrolyte systems

Electroneutrality is a fundamental principle in electrochemistry. It is essential in studying electrolytes and their behavior in batteries, fuel cells, electrochemical cells, etc. In most cases, a mixture of electrolytes is used in electrochemical systems. A naturally occurring system like seawater is also a mixture of multiple electrolytes. Electroneutrality affects the properties of solutions, such as charge neutrality, ionic mobility, pH, solubility of salts, conductivity, osmotic pressure, etc. More details about this will be given in chapter 4.

Local electroneutrality refers to the balance of charges within a small localized region of an electrolyte solution. It plays a huge role in the formation and properties of ion atmosphere. Depending on the components of the solution, ion atmospheres will have different structures and properties. For example, ion atmospheres and local electroneutrality effects near a charged surface will differ from an uncharged solution. Also, depending on their size, charge, and concentration, different ions contribute differently toward local electroneutrality. In this thesis, we have examined

the contribution of different species in solution towards local electroneutrality. We have tested two types of mixed electrolyte systems. Mixed electrolytes with a common ion near a charged surface and seawater, and also a mixture of multiple ionic species.

1.9. Organization of the dissertation

This thesis is centered around inorganic ionic solutions. In Chapter 2, KB theory is applied to build a FF for aqueous alkali metal nitrate. Different partial charges on the N and O atoms of the nitrate ion are tested, and LJ parameters are optimized to obtain a FF that reproduces several properties of aqueous alkali metal nitrate solution. Chapter 3 discusses the process of building a FF for aqueous alkaline earth metal nitrates. Magnesium nitrate, Calcium nitrate, and Strontium nitrate are chosen for the FF optimization process. Barium nitrate could not be studied due to its low solubility in water. In Chapter 4, we investigate how local electroneutrality affects the properties of mixed electrolytes with a common ion near a charged surface. We have chosen alkali chlorides as the system of interest, as KBFF already has all the parameters available for alkali metals and chloride ions. In Chapter 5, we have studied the role of local electroneutrality in seawater. We have chosen three types of seawater (standard seawater, Dead Sea brine, and Red Sea brine). Some of the ions have very low concentrations in seawater. Hence, large systems were required, and longer simulations were needed to be performed to provide statistically meaningful results. These made the simulations computationally expensive. Chapter 6 comprises a conclusion and future directions.

1.10. References

(1) *The Nobel Prize in Chemistry 1998*. NobelPrize.org. https://www.nobelprize.org/prizes/chemistry/1998/summary/ (accessed 2023-12-14).

(2) Alder, B. J.; Wainwright, T. E. Studies in Molecular Dynamics. I. General Method. *The Journal of Chemical Physics* **2004**, *31* (2), 459–466. https://doi.org/10.1063/1.1730376.

(3) *The Nobel Prize in Chemistry 2013*. NobelPrize.org. https://www.nobelprize.org/prizes/chemistry/2013/summary/ (accessed 2023-12-14).

(4) *Settle: An analytical version of the SHAKE and RATTLE algorithm for rigid water models - Miyamoto - 1992 - Journal of Computational Chemistry - Wiley Online Library*. https://onlinelibrary.wiley.com/doi/abs/10.1002/jcc.540130805 (accessed 2024-05-15).

(5) Hess, B.; Bekker, H.; Berendsen, H. J. C.; Fraaije, J. G. E. M. LINCS: A Linear Constraint Solver for Molecular Simulations. *Journal of Computational Chemistry* **1997**, *18* (12), 1463–1472. https://doi.org/10.1002/(SICI)1096-987X(199709)18:12<1463::AID-JCC4>3.0.CO;2-H.

(6) Alder, B. J.; Wainwright, T. E. Studies in Molecular Dynamics. I. General Method. *The Journal of Chemical Physics* **1959**, *31* (2), 459–466.

(7) von Neumann, J.; Ulam, S. Monte Carlo Simulation.

(8) Kohn, W. Nobel Lecture: Electronic Structure of Matter—Wave Functions and Density Functionals. *Reviews of Modern Physics* **1999**, *71* (5), 1253.

(9) Laio, A.; Parrinello, M. Escaping Free-Energy Minima. *Proceedings of the National academy of sciences* **2002**, *99* (20), 12562–12566.

(10) Warshel, A.; Levitt, M. Theoretical Studies of Enzymic Reactions: Dielectric, Electrostatic and Steric Stabilization of the Carbonium Ion in the Reaction of Lysozyme. *Journal of Molecular Biology* **1976**, *103* (2), 227–249. https://doi.org/10.1016/0022-2836(76)90311-9.

(11) Car, R.; Parrinello, M. Unified Approach for Molecular Dynamics and Density-Functional Theory. *Phys. Rev. Lett.* **1985**, *55* (22), 2471–2474. https://doi.org/10.1103/PhysRevLett.55.2471.

(12) van Gunsteren, W. F.; Berendsen, H. J. C. Computer Simulation of Molecular Dynamics: Methodology, Applications, and Perspectives in Chemistry. *Angewandte Chemie International Edition in English* **1990**, *29* (9), 992–1023. https://doi.org/10.1002/anie.199009921.

(13) Hünenberger, P. H. Thermostat Algorithms for Molecular Dynamics Simulations. In *Advanced Computer Simulation: Approaches for Soft Matter Sciences I*; Dr. Holm, C., Prof. Dr. Kremer, K., Eds.; Advances in Polymer Science; Springer: Berlin, Heidelberg, 2005; pp 105–149. https://doi.org/10.1007/b99427.

(14) Basconi, J. E.; Shirts, M. R. Effects of Temperature Control Algorithms on Transport Properties and Kinetics in Molecular Dynamics Simulations. *J. Chem. Theory Comput.* **2013**, *9* (7), 2887–2899. https://doi.org/10.1021/ct400109a.

(15) Allen, M. P.; Tildesley, D. J. *Computer Simulation of Liquids*; Oxford University Press, 2017.

(16) Frenkel, D.; Smit, B.; Ratner, M. A. *Understanding Molecular Simulation: From Algorithms to Applications*. *Physics Today* **1997**, *50* (7), 66–66. https://doi.org/10.1063/1.881812.

(17) Ke, Q.; Gong, X.; Liao, S.; Duan, C.; Li, L. Effects of Thermostats/Barostats on Physical Properties of Liquids by Molecular Dynamics Simulations. *Journal of Molecular Liquids* **2022**, *365*, 120116. https://doi.org/10.1016/j.molliq.2022.120116.

(18) Andersen, H. C. Molecular Dynamics Simulations at Constant Pressure and/or Temperature. *The Journal of Chemical Physics* **2008**, *72* (4), 2384–2393. https://doi.org/10.1063/1.439486.

(19) Van Gunsteren, W. F.; Berendsen, H. J. C. A Leap-Frog Algorithm for Stochastic Dynamics. *Molecular Simulation* **1988**, *1* (3), 173–185. https://doi.org/10.1080/08927028808080941.

(20) Berendsen, H. J. C.; Postma, J. P. M.; van Gunsteren, W. F.; DiNola, A.; Haak, J. R. Molecular Dynamics with Coupling to an External Bath. *The Journal of Chemical Physics* **1984**, *81* (8), 3684–3690. https://doi.org/10.1063/1.448118.

(21) Bussi, G.; Donadio, D.; Parrinello, M. Canonical Sampling through Velocity Rescaling. *The Journal of Chemical Physics* **2007**, *126* (1), 014101. https://doi.org/10.1063/1.2408420.

(22) Nosé, S. A Unified Formulation of the Constant Temperature Molecular Dynamics Methods. *The Journal of Chemical Physics* **1984**, *81* (1), 511–519. https://doi.org/10.1063/1.447334.

(23) Hoover, W. G. Canonical Dynamics: Equilibrium Phase-Space Distributions. *Phys. Rev. A* **1985**, *31* (3), 1695–1697. https://doi.org/10.1103/PhysRevA.31.1695.

(24) Parrinello, M.; Rahman, A. Polymorphic Transitions in Single Crystals: A New Molecular Dynamics Method. *Journal of Applied Physics* **1981**, *52* (12), 7182–7190. https://doi.org/10.1063/1.328693.

(25) Zendehboudi, S. 4 - Molecular Dynamics Simulation in Energy and Chemical Systems. In *Modelling of Chemical Process Systems*; Imtiaz, S. A., Ed.; Elsevier, 2023; pp 91–148. https://doi.org/10.1016/B978-0-12-823869-1.00002-8.

(26) Chapman, J. B. J. Improving the Functional Control of Ferroelectrics Using Insights from Atomistic Modelling. Doctoral, UCL (University College London), 2018, pp i–271. https://discovery.ucl.ac.uk/id/eprint/10056036/ (accessed 2024-01-04).

(27) Ewald, P. P.

(28) Darden, T.; York, D.; Pedersen, L. Particle Mesh Ewald: An N·log(N) Method for Ewald Sums in Large Systems. *The Journal of Chemical Physics* **1993**, *98* (12), 10089–10092. https://doi.org/10.1063/1.464397.

(29) Seyyedattar, M.; Zendehboudi, S.; Butt, S. Invited Review - Molecular Dynamics Simulations in Reservoir Analysis of Offshore Petroleum Reserves: A Systematic Review

of Theory and Applications. *Earth-Science Reviews* **2019**, *192*, 194–213. https://doi.org/10.1016/j.earscirev.2019.02.019.

(30) Russell, J. *Anton 3 Is a "Fire-Breathing" Molecular Simulation Beast*. HPCwire. https://www.hpcwire.com/2021/09/01/anton-3-is-a-fire-breathing-molecular-simulation-beast/ (accessed 2024-01-04).

(31) *Welcome to the GROMACS documentation! — GROMACS documentation*. https://manual.gromacs.org/ (accessed 2024-02-17).

(32) Case, D. A.; Aktulga, H. M.; Belfon, K.; Cerutti, D. S.; Cisneros, G. A.; Cruzeiro, V. W. D.; Forouzesh, N.; Giese, T. J.; Götz, A. W.; Gohlke, H.; Izadi, S.; Kasavajhala, K.; Kaymak, M. C.; King, E.; Kurtzman, T.; Lee, T.-S.; Li, P.; Liu, J.; Luchko, T.; Luo, R.; Manathunga, M.; Machado, M. R.; Nguyen, H. M.; O'Hearn, K. A.; Onufriev, A. V.; Pan, F.; Pantano, S.; Qi, R.; Rahnamoun, A.; Risheh, A.; Schott-Verdugo, S.; Shajan, A.; Swails, J.; Wang, J.; Wei, H.; Wu, X.; Wu, Y.; Zhang, S.; Zhao, S.; Zhu, Q.; Cheatham, T. E.; Roe, D. R.; Roitberg, A.; Simmerling, C.; York, D. M.; Nagan, M. C.; Merz, K. M. AmberTools. *J. Chem. Inf. Model.* **2023**, *63* (20), 6183–6191. https://doi.org/10.1021/acs.jcim.3c01153.

(33) *CHARMM: Home*. https://www.charmm.org/ (accessed 2024-04-17).

(34) Phillips, J. C.; Hardy, D. J.; Maia, J. D. C.; Stone, J. E.; Ribeiro, J. V.; Bernardi, R. C.; Buch, R.; Fiorin, G.; Hénin, J.; Jiang, W.; McGreevy, R.; Melo, M. C. R.; Radak, B. K.; Skeel, R. D.; Singharoy, A.; Wang, Y.; Roux, B.; Aksimentiev, A.; Luthey-Schulten, Z.; Kalé, L. V.; Schulten, K.; Chipot, C.; Tajkhorshid, E. Scalable Molecular Dynamics on

CPU and GPU Architectures with NAMD. *The Journal of Chemical Physics* **2020**, *153* (4), 044130. https://doi.org/10.1063/5.0014475.

(35) *LAMMPS Molecular Dynamics Simulator*. https://www.lammps.org/ (accessed 2021-11-15).

(36) *Life Science: Desmond*. Schrödinger. https://www.schrodinger.com/platform/products/desmond/ (accessed 2024-04-17).

(37) *OpenMM*. https://openmm.org/ (accessed 2024-04-17).

(38) Monticelli, L.; Tieleman, D. P. Force Fields for Classical Molecular Dynamics. In *Biomolecular Simulations: Methods and Protocols*; Monticelli, L., Salonen, E., Eds.; Methods in Molecular Biology; Humana Press: Totowa, NJ, 2013; pp 197–213. https://doi.org/10.1007/978-1-62703-017-5_8.

(39) Kouza, M. *Numerical Simulation of Folding and Unfolding of Proteins*. arXiv.org. https://arxiv.org/abs/1308.2380v1 (accessed 2024-01-06).

(40) Case, D. A.; Cheatham III, T. E.; Darden, T.; Gohlke, H.; Luo, R.; Merz Jr., K. M.; Onufriev, A.; Simmerling, C.; Wang, B.; Woods, R. J. The Amber Biomolecular Simulation Programs. *Journal of Computational Chemistry* **2005**, *26* (16), 1668–1688. https://doi.org/10.1002/jcc.20290.

(41) Huang, J.; Rauscher, S.; Nawrocki, G.; Ran, T.; Feig, M.; de Groot, B. L.; Grubmüller, H.; MacKerell, A. D. CHARMM36m: An Improved Force Field for Folded and Intrinsically

Disordered Proteins. *Nat Methods* **2017**, *14* (1), 71–73. https://doi.org/10.1038/nmeth.4067.

(42) van Gunsteren, W. F.; Daura, X.; Mark, A. E. GROMOS Force Field. In *Encyclopedia of Computational Chemistry*; John Wiley & Sons, Ltd, 2002. https://doi.org/10.1002/0470845015.cga011.

(43) Ploetz, E. A.; Karunaweera, S.; Bentenitis, N.; Chen, F.; Dai, S.; Gee, M. B.; Jiao, Y.; Kang, M.; Kariyawasam, N. L.; Naleem, N.; Weerasinghe, S.; Smith, P. E. Kirkwood–Buff-Derived Force Field for Peptides and Proteins: Philosophy and Development of KBFF20. *J. Chem. Theory Comput.* **2021**, *17* (5), 2964–2990. https://doi.org/10.1021/acs.jctc.1c00075.

(44) Ploetz, E. A.; Karunaweera, S.; Smith, P. E. Kirkwood–Buff-Derived Force Field for Peptides and Proteins: Applications of KBFF20. *J. Chem. Theory Comput.* **2021**, *17* (5), 2991–3009. https://doi.org/10.1021/acs.jctc.1c00076.

(45) Damm, W.; Frontera, A.; Tirado–Rives, J.; Jorgensen, W. L. OPLS All-Atom Force Field for Carbohydrates. *Journal of Computational Chemistry* **1997**, *18* (16), 1955–1970. https://doi.org/10.1002/(SICI)1096-987X(199712)18:16<1955::AID-JCC1>3.0.CO;2-L.

(46) Sun, H.; Ren, P.; Fried, J. R. The COMPASS Force Field: Parameterization and Validation for Phosphazenes. *Computational and Theoretical Polymer Science* **1998**, *8* (1), 229–246. https://doi.org/10.1016/S1089-3156(98)00042-7.

(47) Thompson, J. M. T.; Grindon, C.; Harris, S.; Evans, T.; Novik, K.; Coveney, P.; Laughton, C. Large-Scale Molecular Dynamics Simulation of DNA: Implementation and Validation

of the AMBER98 Force Field in LAMMPS. *Philosophical Transactions of the Royal Society of London. Series A: Mathematical, Physical and Engineering Sciences* **2004**, *362* (1820), 1373–1386. https://doi.org/10.1098/rsta.2004.1381.

(48) van Duin, A. C. T.; Dasgupta, S.; Lorant, F.; Goddard, W. A. ReaxFF: A Reactive Force Field for Hydrocarbons. *J. Phys. Chem. A* **2001**, *105* (41), 9396–9409. https://doi.org/10.1021/jp004368u.

(49) Marrink, S. J.; Risselada, H. J.; Yefimov, S.; Tieleman, D. P.; de Vries, A. H. The MARTINI Force Field: Coarse Grained Model for Biomolecular Simulations. *J. Phys. Chem. B* **2007**, *111* (27), 7812–7824. https://doi.org/10.1021/jp071097f.

(50) Shi, Y.; Xia, Z.; Zhang, J.; Best, R.; Wu, C.; Ponder, J. W.; Ren, P. Polarizable Atomic Multipole-Based AMOEBA Force Field for Proteins. *J. Chem. Theory Comput.* **2013**, *9* (9), 4046–4063. https://doi.org/10.1021/ct4003702.

(51) Schlick, T. Biomolecular Structure and Modeling: Historical Perspective. In *Molecular Modeling and Simulation: An Interdisciplinary Guide*; Schlick, T., Ed.; Interdisciplinary Applied Mathematics; Springer: New York, NY, 2002; pp 1–32. https://doi.org/10.1007/978-0-387-22464-0_1.

(52) Lifson, S.; Warshel, A. Consistent Force Field for Calculations of Conformations, Vibrational Spectra, and Enthalpies of Cycloalkane and n-Alkane Molecules. *The Journal of Chemical Physics* **2003**, *49* (11), 5116–5129. https://doi.org/10.1063/1.1670007.

(53) McCammon, J. A.; Gelin, B. R.; Karplus, M. Dynamics of Folded Proteins. *Nature* **1977**, *267* (5612), 585–590. https://doi.org/10.1038/267585a0.

(54) Levitt, M.; Warshel, A. Computer Simulation of Protein Folding. *Nature* **1975**, *253* (5494), 694–698. https://doi.org/10.1038/253694a0.

(55) Sprik, M.; Klein, M. L. A Polarizable Model for Water Using Distributed Charge Sites. *J. Chem. Phys.* **1988**, *89* (12), 7556–7560. https://doi.org/10.1063/1.455722.

(56) Rick, S. W.; Stuart, S. J.; Berne, B. J. Dynamical Fluctuating Charge Force Fields: Application to Liquid Water. *The Journal of Chemical Physics* **1994**, *101* (7), 6141–6156. https://doi.org/10.1063/1.468398.

(57) Leontyev, I.; Stuchebrukhov, A. Accounting for Electronic Polarization in Non-Polarizable Force Fields. *Phys. Chem. Chem. Phys.* **2011**, *13* (7), 2613–2626. https://doi.org/10.1039/C0CP01971B.

(58) Rudd, R. E.; Broughton, J. Q. Coarse-Grained Molecular Dynamics and the Atomic Limit of Finite Elements. *Phys. Rev. B* **1998**, *58* (10), R5893–R5896. https://doi.org/10.1103/PhysRevB.58.R5893.

(59) González, M. A. Force Fields and Molecular Dynamics Simulations. *JDN* **2011**, *12*, 169–200. https://doi.org/10.1051/sfn/201112009.

(60) Kirkwood, J. G.; Buff, F. P. The Statistical Mechanical Theory of Solutions. I. *The Journal of Chemical Physics* **2004**, *19* (6), 774–777. https://doi.org/10.1063/1.1748352.

(61) Radial Distribution Function. *Wikipedia*; 2023.

(62) Ben-Naim, A. Inversion of the Kirkwood–Buff Theory of Solutions: Application to the Water–Ethanol System. *The Journal of Chemical Physics* **2008**, *67* (11), 4884–4890. https://doi.org/10.1063/1.434669.

(63) Weerasinghe, S.; Smith, P. E. A Kirkwood−Buff Derived Force Field for Mixtures of Urea and Water. *J. Phys. Chem. B* **2003**, *107* (16), 3891–3898. https://doi.org/10.1021/jp022049s.

(64) Pierce, V.; Kang, M.; Aburi, M.; Weerasinghe, S.; Smith, P. E. Recent Applications of Kirkwood–Buff Theory to Biological Systems. *Cell Biochem Biophys* **2008**, *50* (1), 1–22. https://doi.org/10.1007/s12013-007-9005-0.

(65) Dawass, N.; Krüger, P.; Schnell, S. K.; Simon, J.-M.; Vlugt, T. J. H. Kirkwood-Buff Integrals from Molecular Simulation. *Fluid Phase Equilibria* **2019**, *486*, 21–36. https://doi.org/10.1016/j.fluid.2018.12.027.

(66) Ben-Naim, A. Inversion of the Kirkwood–Buff Theory of Solutions: Application to the Water–Ethanol System. *The Journal of Chemical Physics* **1977**, *67* (11), 4884–4890. https://doi.org/10.1063/1.434669.

(67) Matteoli, E.; Lepori, L. Solute–Solute Interactions in Water. II. An Analysis through the Kirkwood–Buff Integrals for 14 Organic Solutes. *The Journal of Chemical Physics* **1984**, *80* (6), 2856–2863. https://doi.org/10.1063/1.447034.

(68) Schnell, S. K.; Vlugt, T. J. H.; Simon, J.-M.; Bedeaux, D.; Kjelstrup, S. Thermodynamics of a Small System in a μT Reservoir. *Chemical Physics Letters* **2011**, *504* (4), 199–201. https://doi.org/10.1016/j.cplett.2011.01.080.

(69) Schnell, S. K.; Liu, X.; Simon, J.-M.; Bardow, A.; Bedeaux, D.; Vlugt, T. J. H.; Kjelstrup, S. Calculating Thermodynamic Properties from Fluctuations at Small Scales. *J. Phys. Chem. B* **2011**, *115* (37), 10911–10918. https://doi.org/10.1021/jp204347p.

(70) Ploetz, E. A.; Rustenburg, A. S.; Geerke, D. P.; Smith, P. E. To Polarize or Not to Polarize? Charge-on-Spring versus KBFF Models for Water and Methanol Bulk and Vapor–Liquid Interfacial Mixtures. *J. Chem. Theory Comput.* **2016**, *12* (5), 2373–2387. https://doi.org/10.1021/acs.jctc.5b01115.

(71) Gee, M. B.; Cox, N. R.; Jiao, Y.; Bentenitis, N.; Weerasinghe, S.; Smith, P. E. A Kirkwood-Buff Derived Force Field for Aqueous Alkali Halides. *J. Chem. Theory Comput.* **2011**, *7* (5), 1369–1380. https://doi.org/10.1021/ct100517z.

(72) Naleem, N.; Bentenitis, N.; Smith, P. E. A Kirkwood-Buff Derived Force Field for Alkaline Earth Halide Salts. *The Journal of Chemical Physics* **2018**, *148* (22), 222828. https://doi.org/10.1063/1.5019454.

(73) Schaefer, D.; Kohns, M.; Hasse, H. Molecular Modeling and Simulation of Aqueous Solutions of Alkali Nitrates. *The Journal of Chemical Physics* **2023**, *158* (13), 134508. https://doi.org/10.1063/5.0141331.

Chapter 2 - A Kirkwood-Buff theory derived force field for aqueous alkali nitrate solutions

2.1. Introduction

Alkali metal nitrates are ubiquitous in nature and the chemical industry. They are used as oxidizing agents, fertilizers, common reagents in chemistry labs, etc. Due to their oxidizing properties, they are also used in pyrotechnics and fireworks. Among the alkali metal (Li, Na, K, Rb, and Cs) nitrates, $NaNO_3$ and KNO_3 are the commercially most important. $NaNO_3$ is used as a preservative in the food industry. KNO_3 is used as a nitrogenous fertilizer, providing potassium and nitrogen, essential nutrients for plant growth. KNO_3 is also used in heat transfer fluids as it can absorb and transfer heat effectively, thereby making it suitable for some industrial applications. Alkali metal nitrates are used in rocket propellants as a cleaner and more environment-friendly alternative to chlorine-containing oxidants.[1] Some alkali nitrates also find applications in the pharmaceutical industry. Nitrate anion is biologically very important. Nitrates provide essential nutrients for plants, but excessive amounts can lead to significant water quality problems such as eutrophication.[2] Inorganic nitrate and nitrite can be found in the body or consumed through food. When these compounds are metabolized in the body, they produce nitric oxide (NO) and other nitrogen oxides that are biologically active. This pathway is becoming recognized as an important regulator of blood flow, cellular signalling, energy production, and the body's response to low oxygen levels (hypoxia).[3] Nitrate stimulates the synthesis of proteins, DNA, and RNA.[4] Nitrate plays the most critical role in the nitrogen cycle. The nitrogen cycle involves the transformation of nitrogen between different living and non-living forms in the environment.[5] Some bacteria can reduce nitrate ions to nitrogen gas, using nitrate reductase enzyme, thereby releasing nitrogen into

the atmosphere.[6] Most of the reactions of nitrate ions occur in an aqueous environment, and all the alkali metal nitrates are highly soluble in water.[7]

The importance of nitrates has fuelled a desire to understand their solution properties. Where experimental data is scarce, the use of computer simulation has been beneficial. However, computer simulation studies are sensitive to the models employed. Building a FF model for an electrolyte solution such as aqueous nitrate can be difficult due to the intricate interplay between ions and solvent molecules. Several factors need to be considered. In most cases, the partial atomic charges associated with the atoms come from gas-phase quantum mechanics (QM) simulations. However, it is not always the most accurate to use the partial atomic charges obtained directly from QM as the polarization of nitrate in solution due to the presence of polar solvent molecules and other ions will be significant. Performing a simulation with an explicitly polarizable model increases the computational cost tremendously. Hence, there is a need to develop simpler models that include polarization effects in terms of effective fixed partial atomic charges thereby reducing the computational cost.

Alkali metal nitrates can be used as a probe to develop a nitrate force field (FF) for biological and other systems. Several nitrate FFs have been published over the years. Borodin et al. published a polarizable and non-polarizable FF for nitrates based on alkyl nitrates.[8] Xie et al. studied ion pairing in lithium, sodium, and potassium nitrate solutions by using an electronic continuum correction.[9] In two separate works, Ni et al. and Fantauzzo et al. built a FF for alkali metal nitrates that can be used for the molten and crystallized forms, respectively.[10,11] Recently, Schaefer et al. published a FF for alkali nitrate aqueous solutions.[12] They adopted models from the literature and

made no adjustments, However, our initial tests found that their FF only worked for low, less than 1 m concentrations. In another recent study, Trejos et al. parameterized nitrate ions as an extension to the Madrid-2019 FF.[13–15] They used nitrate ion charges from gas-phase quantum chemical calculations and then scaled those by a factor of 0.85 to mimic polarization effects. The LJ parameters were also taken from the same study.[16,17] The interaction terms (σ_{ij} and ϵ_{ij}) between the counterions were adjusted by comparing the experimental properties, such as viscosity and diffusion constant of alkali nitrate aqueous solution with the simulated data.

Our group has recently published a FF for the simulation of classical biological systems such as peptides and proteins, named KBFF20,[18,19] and also a Kirkwood-Buff (KB) theory derived FF for aqueous alkali halides.[20] In this work, we have adapted the alkali metal parameters from the previously published article and scaled the Lennard-Jones (LJ) parameters between the cation and nitrate oxygen (referred to as ON) to build a FF for alkali metal nitrates, which is compatible with the KBFF20 models. Our approach to building a FF for alkali nitrate heavily relies on the Kirkwood-Buff theory of solutions.[21] The KBIs for aqueous alkali metal nitrates were used for the target data. Validation of the FF was performed by calculating properties such as the first shell coordination number, dielectric decrement, and surface tension. We have used the SPC/E water model, which was also used to build KBFF20 for compatibility. To our knowledge, this is the first Kirkwood-Buff theory-based alkali metal nitrate FF that has been developed.

2.2. Methods

2.2.1. Kirkwood Buff Analysis of Experimental Data

The KBIs can be extracted from experimental data using Ben-Naim's KB inversion process.[22] For a binary solution of a solute (2) in a solvent (1) there are three KBIs corresponding to the solute-solute, solute-solvent and solvent-solvent distributions. The three composition dependent KBIs can be obtained from the KBI inversion equation,[19]

$$\delta_{\alpha\beta} + \rho_\beta G_{\alpha\beta} = \rho_\beta RT\kappa_T + \frac{1}{x_1 x_2}\frac{x_\beta}{x_\alpha}\frac{(1-\rho_\alpha \bar{V}_\alpha)(1-\rho_\beta \bar{V}_\beta)}{(\partial\beta\mu_\alpha / \partial x_\beta)_{T,P}} \tag{2.1}$$

where $\delta_{\alpha\beta}$ is the Kronecker delta, ρ is the number density, $G_{\alpha\beta}$ is the KBI, R is the gas constant, T is the temperature, κ_T is the compressibility, x is the mole fraction, $\bar{V}$ is the partial molar volume, and $(\partial\beta\mu_\alpha / \partial x_\beta)$ is the derivative of the chemical potential (related to the corresponding activity coefficient).

To perform the inversion one requires three independent pieces of thermodynamics data: one partial molar volume, the isothermal compressibility, and one derivative of the chemical potential (activity coefficient). The second partial molar volume and the other chemical potential derivatives are related by eq 2.2, and the Gibbs-Duhem equation, respectively.

$$\rho_1 \bar{V}_1 + \rho_2 \bar{V}_2 = 1 \tag{2.2}$$

The isothermal compressibility data for solution mixtures is often not available. In that case, the isothermal compressibility can be assumed to follow,

$$\kappa_T = \varphi_1 \kappa_{T_1}^0 + \varphi_2 \kappa_{T_2}^0 \tag{2.3}$$

where $\kappa_{T_1}^0$ is the compressibility of the pure solvent, $\kappa_{T_2}^0$ is the compressibility of the pure solute, and φ represents the volume fraction. The general method for obtaining the partial molar volumes is to fit the density versus composition data. If the density data is unavailable, then the density of pure solute crystal and pure solvent density can be used as the PMV, and is then independent of composition.[23] Neither of these approximations significantly affects the resulting KBIs. The most critical data for obtaining accurate KBIs is the activity data.[19] It can be obtained from phase equilibria or osmotic pressure studies. A table with references for the activity coefficient and density data used in this study is given in Table 2.1.

Compound	Activity Coefficient Reference	Density Reference	Temp (K)	Pressure (bar)
$LiNO_3$	[24]	[25]	298	-
$NaNO_3$	[24]	[26]	298	1
KNO_3	[24]	[26]	298	1
$RbNO_3$	[24]	[27]	298	1
$CsNO_3$	[24]	[27]	298	1

Table 2.1. References for activity coefficient and density data for aqueous alkali metal nitrate solutions. The data for $RbNO_3$ and $CsNO_3$ correspond to the pure crystals

Both the activity coefficient and the density data must be fitted with relevant equations to provide data at the same composition. The equation for fitting the activity coefficient ($\gamma_{\pm}$) with salt molality (m) is given by,

$$\ln \gamma_{\pm} = \frac{-1.178\sqrt{m}}{1+a_1 m} - \ln(1-a_2 m) + a_3 m \tag{2.4}$$

The equation for fitting the density (d) with salt molality (m) is given by,

$$d = 0.99705 + a_1 m + a_2 m^{1.5} + a_3 m^2 \tag{2.5}$$

In both the equations a_1, a_2, and a_3 are separate sets of fitting parameters. We obtain these fitting parameters by running our in-house codes. An example of our fits to the activity coefficient and density data for an aqueous KNO_3 solutions is given in Figure 2.1.

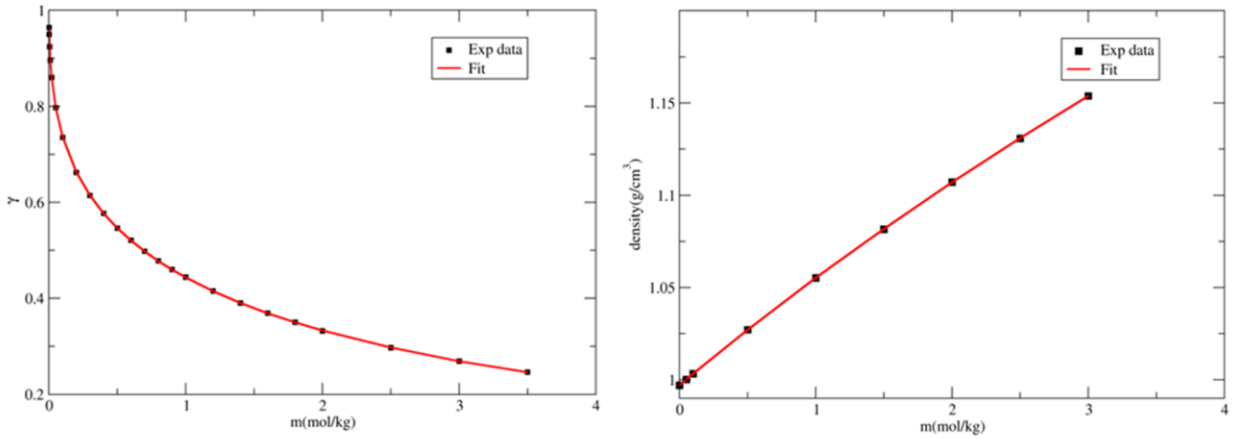

Figure 2.1. An example of the experimental and fitted data for the activity coefficient (left) and density (right) of aqueous KNO_3 solutions as function of salt molality.

2.2.2. Parameterization of nitrate ion and alkali metal ions

Parameters for all the alkali metal ions were developed in the previous work of our group,[20] and were added to the KBFF20 force field.[18,19] The LJ parameters (σ and ϵ) for alkali metals were taken from the previous work. The nitrate ion was parameterized through several steps. To test different parameter changes, we selected KNO_3 as the test salt. The water model used was SPC/E,[28] to be consistent with the KBFF20. We used the bonded (bond length and angle) parameters provided in the literature.[29] First, we tried to parameterize the partial charges on the N and O atoms of the nitrate anion. We tested charges from experimental papers, quantum calculations, and guessed charges. A list of the charges tested and the corresponding KBI values obtained after simulation are given in Table 2.2. However, we found that the charges did not affect the KBI values significantly and so we decided to stick to the charge from a combined experimental and theoretical study.[29] The non-bonded parameters for ON were taken from KBFF20 and then scaled to obtain the proper contact distances between atoms H-ON, ON-OW, N-H, and N-OW, as determined in a recent AIMD simulation of the nitrate ion.[30] The details of the final parameters used for the atoms in nitrate ion are given in Table 2.3.

Charge on N	Charge on O	KNO_3 G_{22} (cm^3/mol)
-0.4	-0.2	-78
-0.7	-0.1	-80
-0.1	-0.3	-76
+0.926	-0.642	-82
-1.0	0	-65
+1.4	-0.8	-88
+2	-1	-77
+0.65	-0.55	-83
+0.20	-0.40	-85

Table 2.2. Charges tested on N and O atoms of the nitrate ion. Experimental KNO_3 G_{22} = +173 cm^3/mol (at 2m)

Atom	Charge	σ (nm)	ϵ (kJ/mol)
N	+0.65	0.3201	0.5620
ON	-0.55	0.3465	0.6047

Table 2.3. Final nitrate ion charges and LJ parameters (after optimization)

The LJ σ parameter was already set in KBFF20 for the alkali metal cations. The initial LJ ϵ parameter was taken from KBFF20. However, this provided relatively poor agreement with the experimental KBIs. Hence, we used a simple scaling factor (s) with respect to the ϵ value of ON to generate the correct KBIs. This approach has been used before in our studies of alkali halides.[20] The initial and final values of the LJ parameters are provided in Table 2.4. To calculate LJ interaction between unlike atoms a geometric combination rule was used.

Cation	σ(nm) (original)	ϵ(kJ/mol) (original)	ON-Cation ϵ(kJ/mol) (scaled)	ON-Cation scaling factor (s)
Li	0.2511	0.7	0.1952	0.2
Na	0.2914	0.32	0.2199	0.5
K	0.3402	0.13	0.1963	0.7
Rb	0.3542	0.15	0.2409	0.8
Cs	0.3783	0.065	0.1784	0.9

Table 2.4. Initial and final alkali metal LJ parameters and the scaling factors between different cations and the nitrate oxygen (ON)

2.2.3. Molecular Dynamics Simulation Details

All the molecular dynamics simulations were performed using GROMACS 2019.5 software.[31] 10 nm cubic simulation boxes were used. Random initial configuration of 1m, 2m, 3m, and 4m alkali nitrate aqueous solutions were generated using custom-made Fortran code. The SPC/E water

model was used.[32] The system was maintained at isothermal isobaric condition (NPT ensemble). The temperature was maintained at 300K using a Nosè-Hoover thermostat.[33] Parrinello-Rahman pressure coupling was used to keep the pressure at 1 bar.[34] The nitrate ion bonds were constrained using the LINCS algorithm and the water bonds were constrained using SETTLE algorithm.[35,36] A 2 fs time step was used to integrate the equations of motion. The particle mesh Ewald (PME) was used to model electrostatic interactions with a 1 nm cut-off distance for real space calculation and a 1 nm cut-off distance for the van der Waals interactions.[37] The steepest descent method was used for three (1000-step each) energy minimization processes, followed by 1 ns equilibration. All the production runs were 50 ns long, except for the calculation of surface tensions, for which a 100 ns long run was performed. In the production run, the first 10 ns were further discarded as part of the equilibration process, and the rest of the 40 ns were divided into chunks of 10 ns to perform analysis. In the production runs configurations were saved every 1 ps.

For the analysis process, a custom-written Fortran code was used to calculate a center of mass radial distribution functions (RDFs), which were then integrated to obtain KB integrals (KBI). The simulated KBIs were compared to the experimentally determined KBIs. Adjustments to LJ parameters were made to get the simulated KBI value closer to the experimental value to optimize the force field.

2.3. Results and Discussion

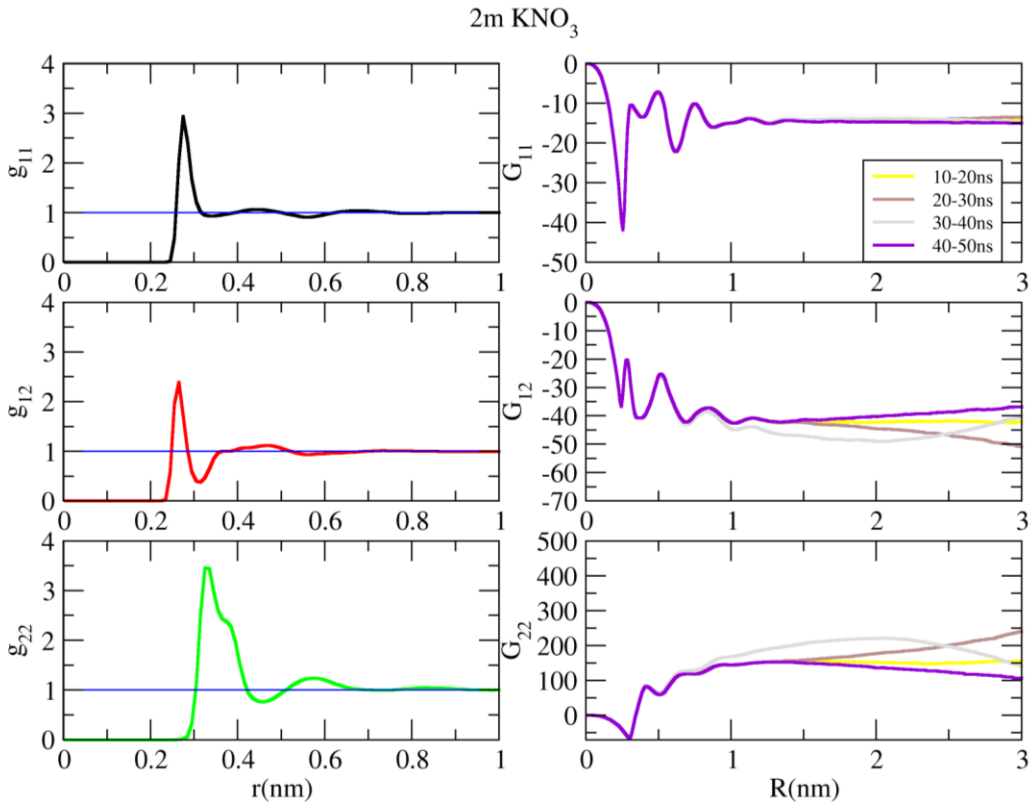

Figure 2.2. Simulated RDFs as a function of distance and the corresponding KBIs as a function of integration distance for 2m KNO_3 (2) in aqueous (1) solution obtained from different simulation times.

Sample RDFs and integrated KBIs for different species in 2m KNO_3 solution are given in Figure 2.2. In this figure and all the following figures, 1 represents solvent, and 2 represents solute. In Figure 2.2, the left-side panel shows RDFs of solvent-solvent, solvent-solute, and solute-solute systems. All the RDFs converge to 1, as particle density should equal the bulk density after a certain distance. The right-side panel of Figure 2.2 contains the integrated KBI values with respect to integration distance, R, in nm. The different colored lines in the right-side panel represent

different time chunks. The data suggest that convergence with time has been achieved, as there is no systematic drift in the data, although different sub-averages do show some statistical fluctuations. We decided to average the integrated KBI values between 1.2 to 1.5 nm to obtain the final KBIs. This distance was chosen as the RDF data displayed no structure beyond 1.5 nm, while a larger distance may result in too small a particle bath.

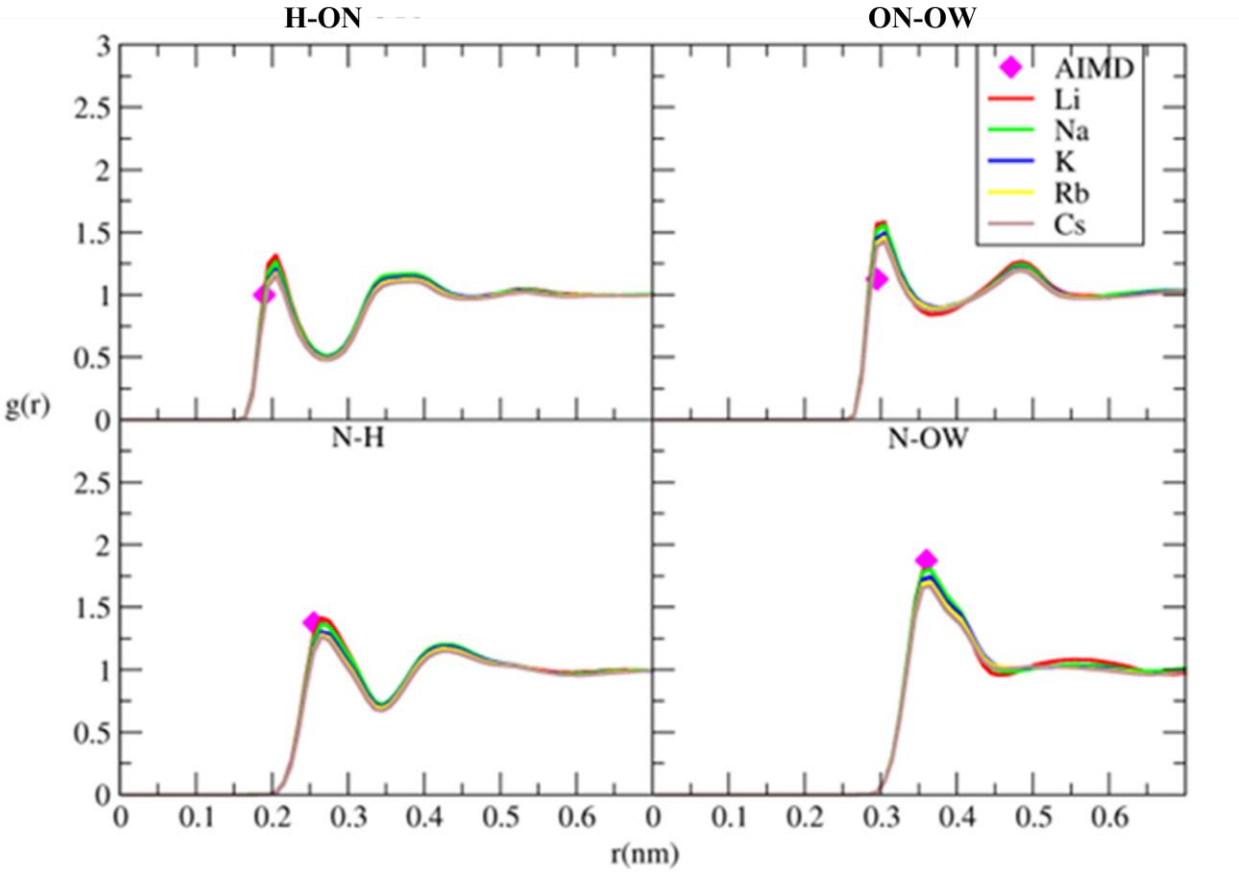

Figure 2.3. Site-site RDFs between water and nitrate ions for a series of metal nitrates at 2m concentrations. The AIMD points correspond to the position and height of the first peak obtained for a single nitrate ion in water.[30]

The site-site RDFs corresponding to the interactions between water and nitrate ion atoms are shown in Figure 2.3. The reference values were taken from an AIMD calculation.[30] It can be seen in the figure that RDFs are not significantly affected by the choice of cation, the peak position does not change, the height changes slightly. Hence, choosing one system as a test system to establish the force field parameters is an acceptable technique. In Figure 2.3, the N-H and N-OW interactions and contact ion distances were reproduced almost perfectly. Thus, we focused on obtaining the correct interactions and contact distances between H to nitrate oxygen and OW to nitrate oxygen. We established a new atom type ON, giving a reasonable contact distance and interaction strength (height of the RDF contact peak) value. It should be noted that getting both contact distance and interaction strength correct was not always achievable. Further tests were conducted using the new atom type ON for the nitrate oxygen. Details of the final atom type ON parameters are provided in Table 2.2.

The primary goal of our method of force field development is reproducing the experimental KBIs. This ensures a reasonable balance between the different distributions. The solute-solute, solute-solvent, and solvent-solvent KBIs before and after adjustments of the force field parameters, are given in Figures 2.4, 2.5, and 2.6, respectively. The KBI values vary from negative to very high (almost infinite) positive values at low salt concentrations. A positive KBI value indicates a net attraction between the two species, and a negative value suggests net repulsion. At lower concentrations, KBI values can reach almost infinity to maintain electroneutrality. This property is obeyed in all our KBI plots. It should be noted that the experimental data does not have an error bar even though there are certainly errors in the experimental data. This is because experimental data for each alkali nitrate molecule has been taken from a single source. In all of the KBIs before

the FF optimization, no differences were observed for the different metals. We were able to differentiate between the metals after optimization and the experimental trends were reproduced for most of them.

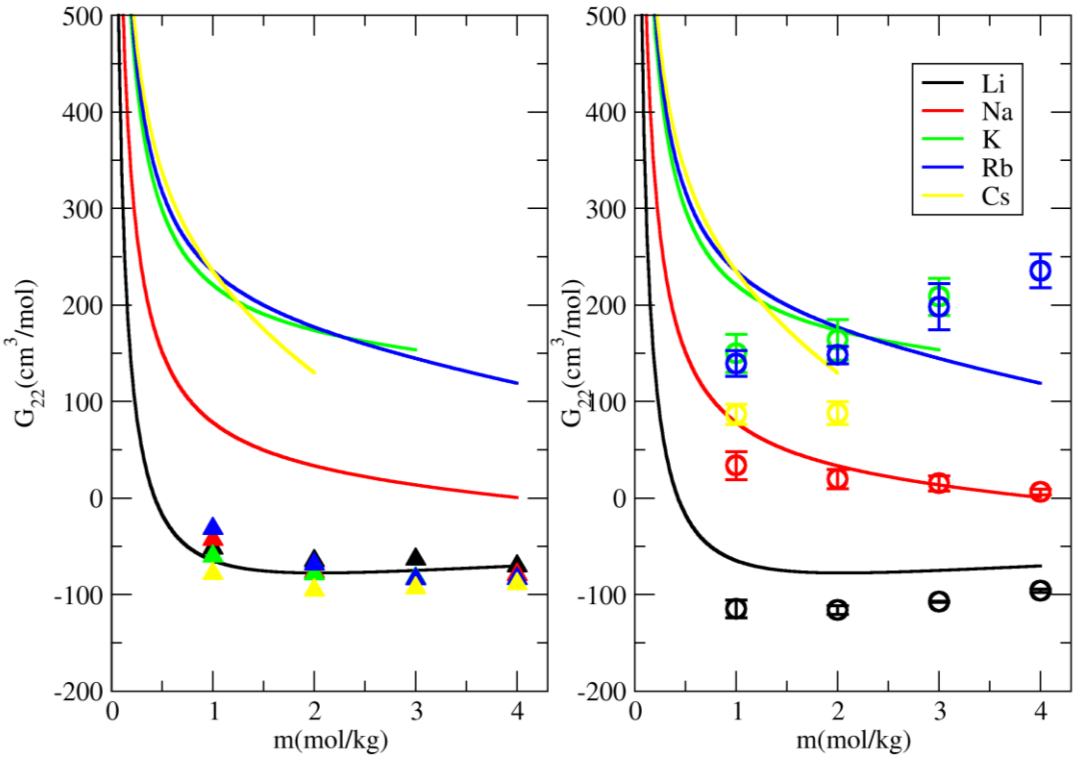

Figure 2.4. Solute-solute KBIs for aqueous metal nitrate solutions before (left) and after (right) optimization of the force field parameters. Lines: Experiment, Symbols: Simulation.

As the cation size increases from Li < Na < K < Rb < Cs, the charge density on the respective ion decreases from Li > Na > K > Rb > Cs. It is more difficult for smaller cations with higher charge densities to lose their solvation shells and form contact ion pairs. Thus, the KBI values are higher for the larger cations. In Figure 2.4, the lines for KNO_3 and $RbNO_3$ stop at 3m and 2m, as there were no experimental activity data available beyond that. The $LiNO_3$ and $NaNO_3$ KBIs show good

agreement with the experiment after optimization. The KNO_3, $RbNO_3$, and $CsNO_3$ KBIs show good agreement with the experiment at 2m concentration.

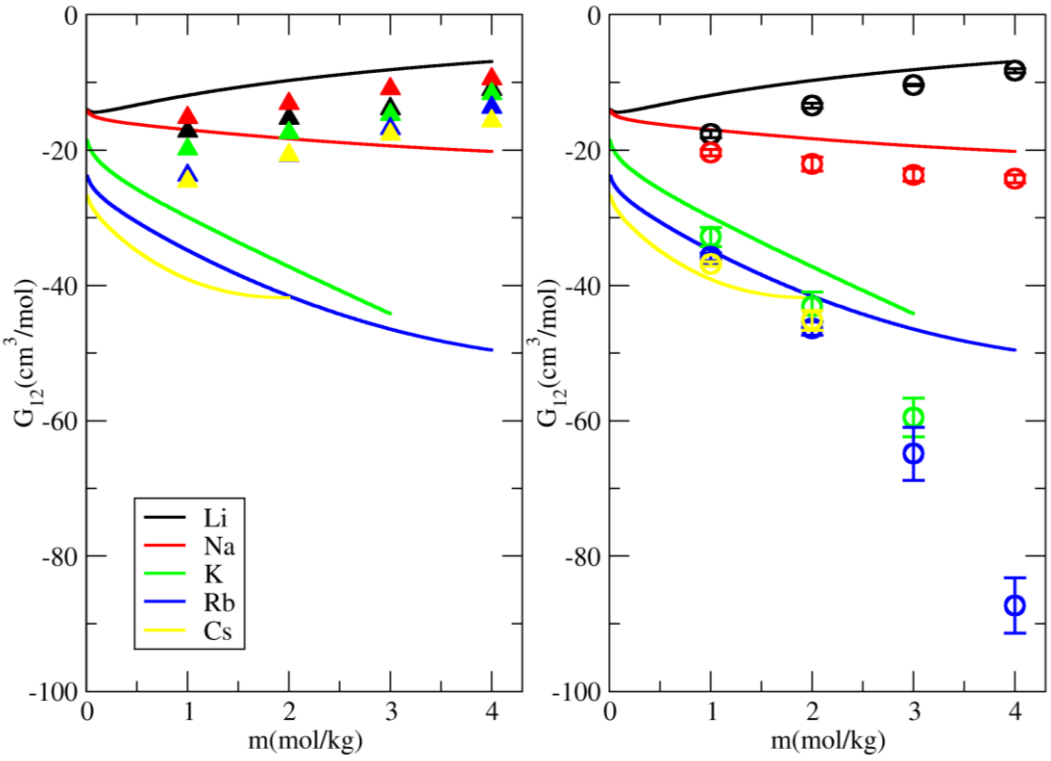

Figure 2.5. Solute-solvent KBIs for aqueous metal nitrate solutions before (left) and after (right) optimization of the force field parameters. Lines: Experiment, Symbols: Simulation.

Figure 2.5 shows the solute-solvent KBIs before and after optimizing the FF. $LiNO_3$ and $NaNO_3$ show good agreement with the experimental value, whereas KNO_3, $RbNO_3$, and $CsNO_3$ follow the trend with their experimental value, although the disagreement increases with salt concentration. The exact reasons for these deviations are unknown.

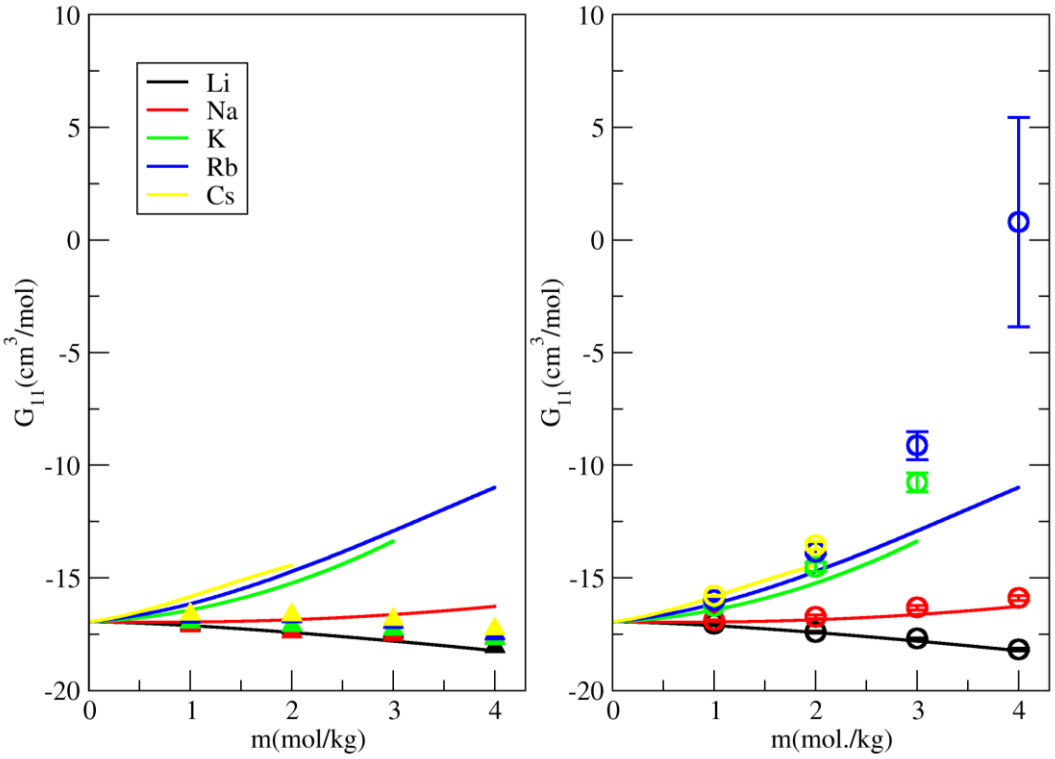

Figure 2.6. Solvent-solvent KBIs for aqueous metal nitrate solutions before (left) and after (right) optimization of the force field parameters. Lines: Experiment, Symbols: Simulation.

Figure 2.6 shows the solvent-solvent KBIs before and after the optimization of the FF. A similar situation to the solute-solvent KBIs was observed in the solvent-solvent KBIs. The $LiNO_3$ and $NaNO_3$ data show good agreement with the experimental values, whereas the KNO_3, $RbNO_3$, and $CsNO_3$ only follow the trend with their experimental value.

After establishing the force field parameters, we have tested the force field by calculating values of properties not included in the parameterization process and compared those to their experimental values. One of the interesting features of electrolytes that affect their properties is the degree of contact ion pairing that occurs between the cation and anion. To explore this we have calculated first shell coordination numbers (C.N.) of the alkali nitrates (cation-N) using the following equation,

$$n(r') = 4\pi\rho\int_0^{r'} g(r)r^2 dr \tag{2.5}$$

In equation 2.5, $n(r')$ is the coordination number, ρ is the number density, and g(r) is the RDF between the cation and the nitrogen atom of the nitrate anion.

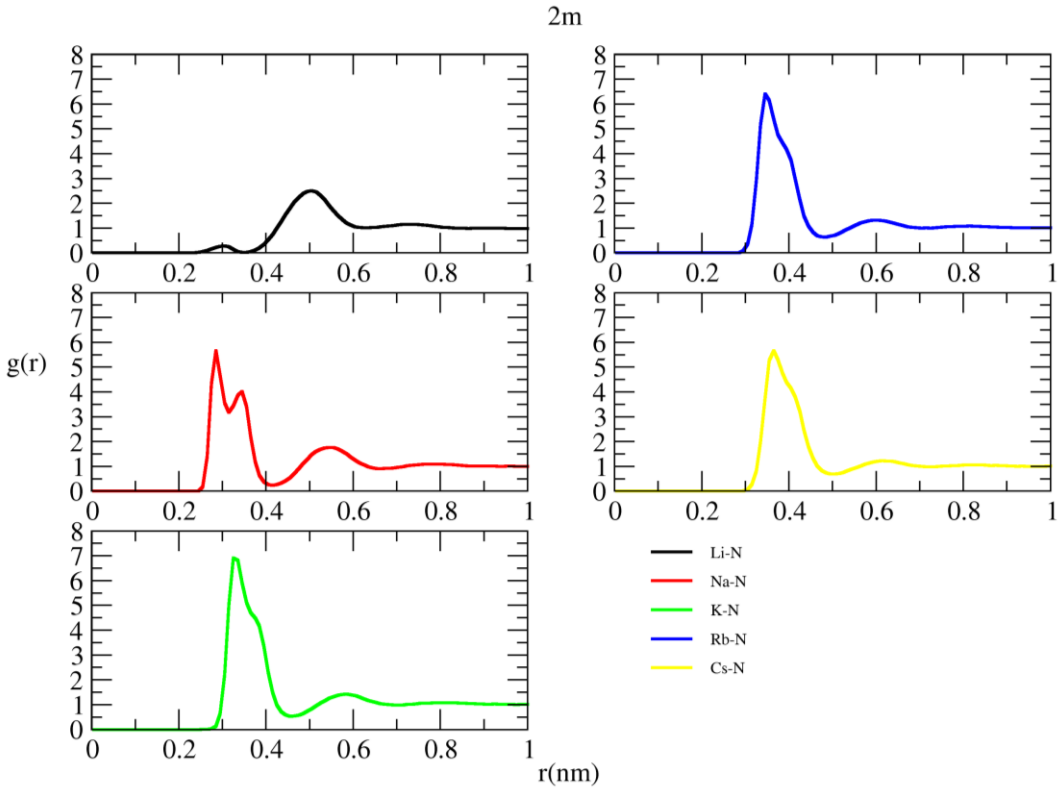

Figure 2.7. RDFs between alkali metal ion and nitrate nitrogen atom for 2m concentrations of aqueous alkali metal nitrate solutions.

The corresponding RDFS are displayed in Figure 2.7. The first peak in the RDF plots represents the formation of the contact ion pair. In the case of $LiNO_3$, the first peak is very small, indicating that Li-NO_3 ion pairs are not formed. This makes sense, as Li has a very high charge density due to its smaller size and does not want to lose its solvation shell to form an ion pair with the NO_3^- anion. As the metal ion size increases, ion-pair formation can be observed. In the case of $NaNO_3$, the split in the peak is due to the two different ways of nitrate ions approaching towards Na^+.[38] The simulated first shell C.N. for $NaNO_3$ matches well with the experimental value. The experimental C.N. was only available for $NaNO_3$.[9] As the size of the alkali metal ions increases, the solvation energy decreases, and the C.N. increases. The trend was established using our force field, as seen in Table 2.5.

Alkali Metal	**Exp. C.N**	**Sim. C.N**	**Integration Distance(nm)**	**Ref**
Li	-	0.001	0.32	-
Na	0.30	0.27	0.32	38
K	-	0.97	0.47	-
Rb	-	1.04	0.48	-
Cs	-	1.09	0.50	-

Table 2.5. The experimental and simulated coordination number of alkali nitrates

Figure 2.8 shows the dielectric decrement ($\varepsilon - \varepsilon_w$) of the alkali nitrate aqueous solution, where ε is the dielectric constant of the salt solution and ε_w is the dielectric constant of pure SPC/E water.[39] The dielectric constants were determined using the equation,

$$\varepsilon = 1 + \frac{4\pi}{3k_B T} \frac{\langle M^2 \rangle - \langle M \rangle^2}{V} \tag{2.6}$$

where M is the total dipole moment of the solvent molecules in the system. The dielectric constant of the salt solution decreases with an increase in salt concentration.[20] This behavior is observed in Figure 2.8.

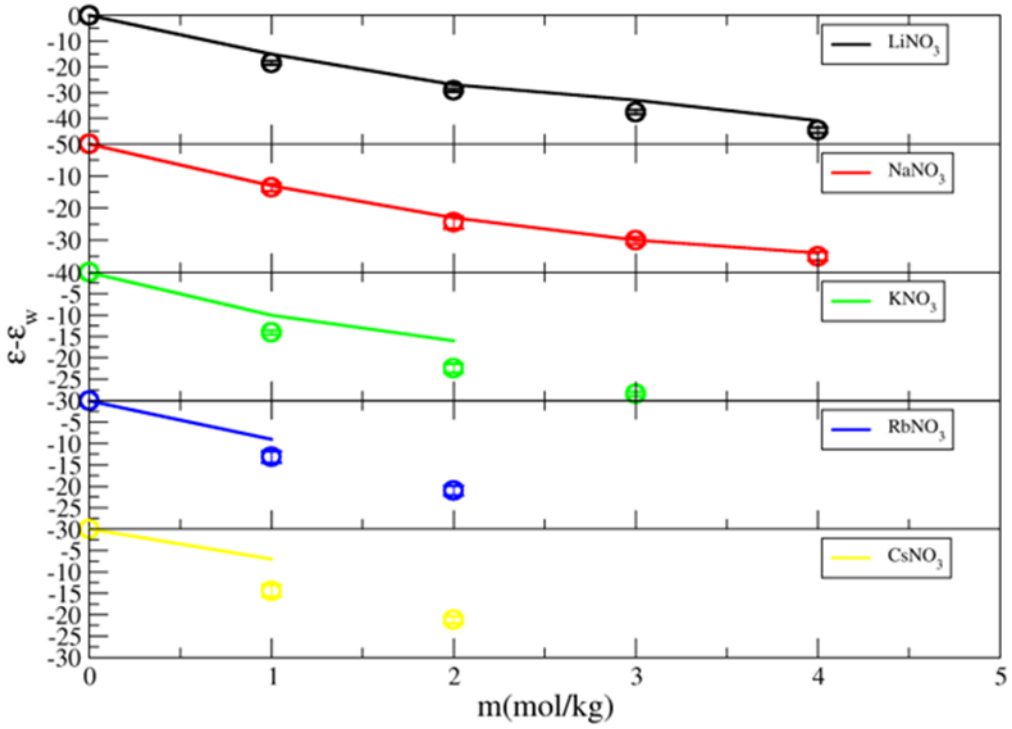

Figure 2.8. Dielectric decrements of aqueous alkali nitrate solution (lines: exp,[40] symbols: KBFF)

Another property that can be simulated and obtained experimentally is the surface tension of the liquid/vapor interface. The system setup to simulate the surface tension of the aqueous alkali nitrate solutions is shown in Figure 2.9.

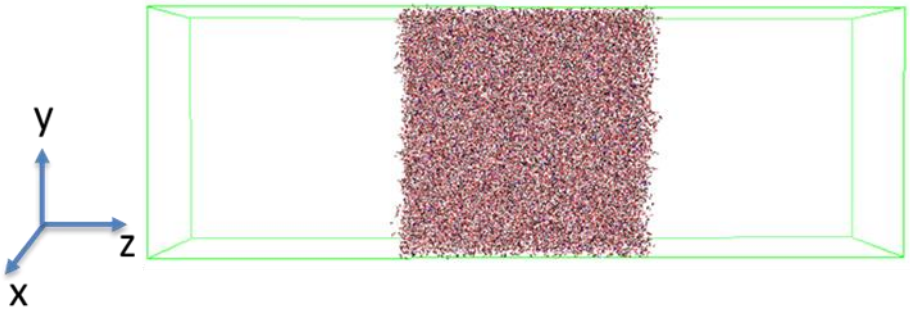

Figure 2.9. The system setup for the simulation of surface tensions of the aqueous salt solutions. Approximate dimensions are x = 10 nm, y = 10 nm, and z = 30 nm.

In Figure 2.9. the salt solution occupies the central 10x10x10 nm^3 region. The simulation box was elongated in the z-direction from both sides of the central salt solution so that the length of the box was 30 nm in the z-direction, and the rest of the space beside the central salt solution was filled with vacuum. This was done to create a liquid/vapor surface of the solution to calculate surface tension. The simulation was performed in a Canonical ensemble (NVT). The simulation length was 100 ns. All other simulation details were the same as given in the methods section. The surface tension of the salt solutions was then calculated using equation 2.7.

$$\gamma = \frac{1}{2} L_z \left[\langle P_{zz} \rangle - \frac{1}{2} (\langle P_{xx} \rangle + \langle P_{yy} \rangle) \right] \tag{2.7}$$

In the equation 2.7., γ is the surface tension of the solution, L_z is the box length in z-direction, $\langle P_{xx} \rangle$, $\langle P_{yy} \rangle$, and $\langle P_{zz} \rangle$ represents the average of the pressure tensor elements in the direction

given in the subscripts. The surface tension of SPC/E water (γ_w) was calculated to be 71.97 mN/m. The surface tension of the salt solution increases with increasing concentration.[41] The trend was observed in our simulations with almost quantitative agreement with experiment.

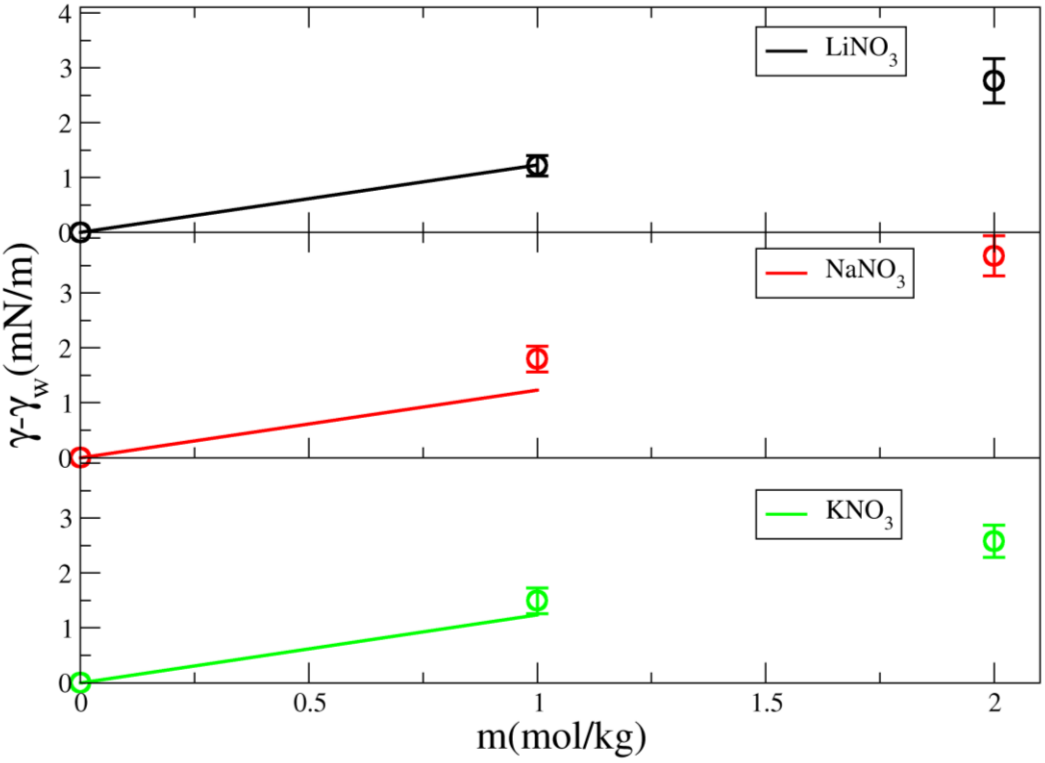

Figure 2.10. Changes in surface tension with concentration for metal nitrate salt solutions (lines: exp,[42] symbols: KBFF).

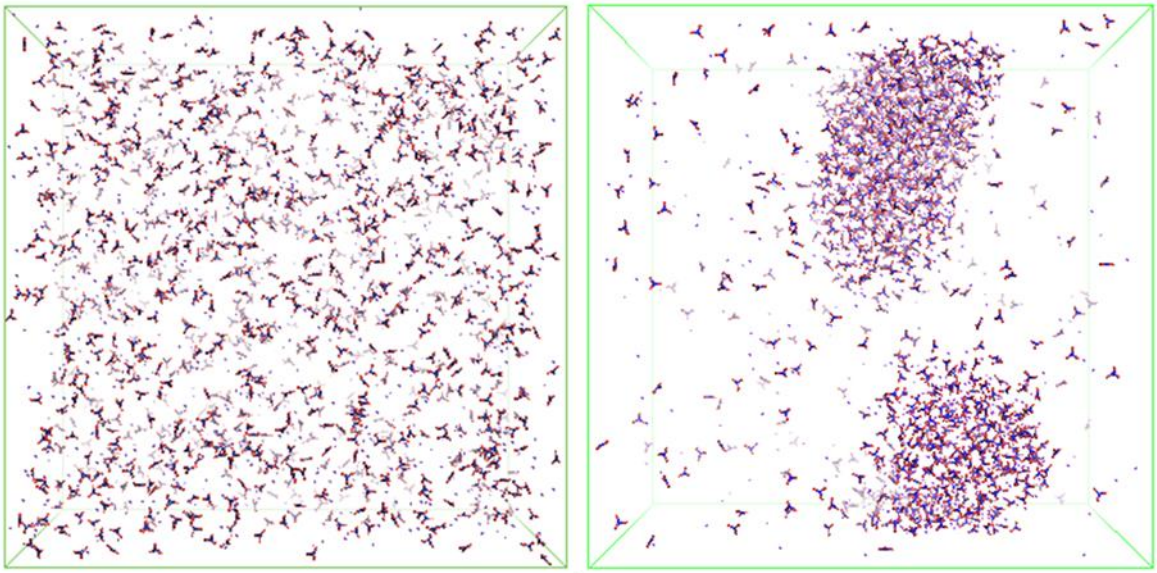

Figure 2.11. Snapshots from the simulation of 2m aqueous KNO_3 after removing the water molecules. The left side is the image obtained from the KBFF, and the right side image is from simulating the FF given by Schaefer et al.[12] Aggregation of the 2m KNO_3 salt solution is evident in the right-hand side image.

A direct comparison of the new KBFF models developed here with a recently published force field by Schaefer et al. for aqueous alkali nitrate solutions was performed.[12] We performed simulations of aqueous alkali nitrate solutions with the force field developed by Schaefer et al. using all the conditions given in their research article. Our results indicate ion aggregation of salt solutions using their force field for all alkali nitrates beyond 1m concentration. In contrast, KBFF does not show any aggregation, in agreement with the KBIs suggested by our analysis of the experimental data. A snapshot of the simulations of both the force fields for 2m KNO_3 is given in Figure 2.11.

The large KBI values for the force field by Schaefer et al. provided in Table 2.6. also indicates significant ion aggregation.

KBI	Exp. Value (cm^3/mol)	KBFF (cm^3/mol)	Schafer et al. (cm^3/mol)
G_{22}	173	155	>28980
G_{12}	-37	-42	<-2668
G_{11}	-15	-15	>232

Table 2.6. The experimental and simulated KBI values for KBFF and the force field by Schaefer et al.

2.4. Conclusion

We have developed a new force field for alkali nitrates in this work. Nitrate ion parameters, such as the charges on each atom and the LJ parameters, were adjusted to reproduce the KBIs. Parameters for the alkali metals were taken from previous work by our group, and then their interaction with nitrate oxygen was scaled. The force field was validated by calculating the dielectric decrement and surface tension as a function of salt concentration. Comparison with a recently published force field showed significant improvement and indicated that accurate force field behavior cannot always be obtained by traditional routes. The transferability of the current force field to alkaline earth metal nitrates will be tested in our future work.

2.5. References:

(1) Terry, B. C.; Sippel, T. R.; Pfeil, M. A.; Gunduz, I. E.; Son, S. F. Removing Hydrochloric Acid Exhaust Products from High Performance Solid Rocket Propellant Using Aluminum-Lithium Alloy. *Journal of Hazardous Materials* **2016**, *317*, 259–266. https://doi.org/10.1016/j.jhazmat.2016.05.067.

(2) *5.7 Nitrates | Monitoring & Assessment | US EPA*. https://archive.epa.gov/water/archive/web/html/vms57.html (accessed 2024-01-19).

(3) Lundberg, J. O.; Gladwin, M. T.; Ahluwalia, A.; Benjamin, N.; Bryan, N. S.; Butler, A.; Cabrales, P.; Fago, A.; Feelisch, M.; Ford, P. C.; Freeman, B. A.; Frenneaux, M.; Friedman, J.; Kelm, M.; Kevil, C. G.; Kim-Shapiro, D. B.; Kozlov, A. V.; Lancaster, J. R.; Lefer, D. J.; McColl, K.; McCurry, K.; Patel, R. P.; Petersson, J.; Rassaf, T.; Reutov, V. P.; Richter-Addo, G. B.; Schechter, A.; Shiva, S.; Tsuchiya, K.; van Faassen, E. E.; Webb, A. J.; Zuckerbraun, B. S.; Zweier, J. L.; Weitzberg, E. Nitrate and Nitrite in Biology, Nutrition and Therapeutics. *Nat Chem Biol* **2009**, *5* (12), 865–869. https://doi.org/10.1038/nchembio.260.

(4) Ingle, J. Nucleic Acid and Protein Synthesis Associated with the Induction of Nitrate Reductase Activity in Radish Cotyledons. *Biochemical Journal* **1968**, *108* (5), 715–724. https://doi.org/10.1042/bj1080715.

(5) Stein, L. Y.; Klotz, M. G. The Nitrogen Cycle. *Current Biology* **2016**, *26* (3), R94–R98. https://doi.org/10.1016/j.cub.2015.12.021.

(6) Cabello, P.; Roldán, M. D.; Moreno-Vivián, C. Nitrate Reduction and the Nitrogen Cycle in Archaea. *Microbiology* **2004**, *150* (11), 3527–3546. https://doi.org/10.1099/mic.0.27303-0.

(7) Eysseltová, J.; Zbranek, V.; Skripkin, M. Y.; Sawada, K.; Tepavitcharova, S. IUPAC-NIST Solubility Data Series. 89. Alkali Metal Nitrates. Part 2. Sodium Nitrate. *Journal of Physical and Chemical Reference Data* **2017**, *46* (1), 013103. https://doi.org/10.1063/1.4972807.

(8) Borodin, O.; Smith, G. D.; Sewell, T. D.; Bedrov, D. Polarizable and Nonpolarizable Force Fields for Alkyl Nitrates. *J. Phys. Chem. B* **2008**, *112* (3), 734–742. https://doi.org/10.1021/jp076149f.

(9) Xie, W. J.; Zhang, Z.; Gao, Y. Q. Ion Pairing in Alkali Nitrate Electrolyte Solutions. *J. Phys. Chem. B* **2016**, *120* (9), 2343–2351. https://doi.org/10.1021/acs.jpcb.5b10755.

(10) Ni, H.; Wu, J.; Sun, Z.; Lu, G.; Yu, J. Molecular Simulation of the Structure and Physical Properties of Alkali Nitrate Salts for Thermal Energy Storage. *Renewable Energy* **2019**, *136*, 955–967. https://doi.org/10.1016/j.renene.2019.01.044.

(11) Fantauzzo, V.; Yeandel, S. R.; Freeman, C. L.; Harding, J. H. A Transferable Force-Field for Alkali Metal Nitrates. *J. Phys. Commun.* **2022**, *6* (5), 055011. https://doi.org/10.1088/2399-6528/ac6e2b.

(12) Schaefer, D.; Kohns, M.; Hasse, H. Molecular Modeling and Simulation of Aqueous Solutions of Alkali Nitrates. *The Journal of Chemical Physics* **2023**, *158* (13), 134508. https://doi.org/10.1063/5.0141331.

(13) Trejos, V. M.; de Lucas, M.; Vega, C.; Blazquez, S.; Gámez, F. Further Extension of the Madrid-2019 Force Field: Parametrization of Nitrate (NO3−) and Ammonium (NH4+) Ions. *The Journal of Chemical Physics* **2023**, *159* (22).

(14) Zeron, I. M.; Abascal, J. L. F.; Vega, C. A Force Field of Li+, Na+, K+, Mg2+, Ca2+, Cl−, and SO42− in Aqueous Solution Based on the TIP4P/2005 Water Model and Scaled Charges for the Ions. *The Journal of Chemical Physics* **2019**, *151* (13), 134504. https://doi.org/10.1063/1.5121392.

(15) Blazquez, S.; Conde, M. M.; Abascal, J. L. F.; Vega, C. The Madrid-2019 Force Field for Electrolytes in Water Using TIP4P/2005 and Scaled Charges: Extension to the Ions F−, Br−, I−, Rb+, and Cs+. *The Journal of Chemical Physics* **2022**, *156* (4), 044505. https://doi.org/10.1063/5.0077716.

(16) Sambasivarao, S. V.; Acevedo, O. Development of OPLS-AA Force Field Parameters for 68 Unique Ionic Liquids. *J. Chem. Theory Comput.* **2009**, *5* (4), 1038–1050. https://doi.org/10.1021/ct900009a.

(17) Doherty, B.; Zhong, X.; Gathiaka, S.; Li, B.; Acevedo, O. Revisiting OPLS Force Field Parameters for Ionic Liquid Simulations. *Journal of chemical theory and computation* **2017**, *13* (12), 6131–6145.

(18) Ploetz, E. A.; Karunaweera, S.; Smith, P. E. Kirkwood–Buff-Derived Force Field for Peptides and Proteins: Applications of KBFF20. *J. Chem. Theory Comput.* **2021**, *17* (5), 2991–3009. https://doi.org/10.1021/acs.jctc.1c00076.

(19) Ploetz, E. A.; Karunaweera, S.; Bentenitis, N.; Chen, F.; Dai, S.; Gee, M. B.; Jiao, Y.; Kang, M.; Kariyawasam, N. L.; Naleem, N.; Weerasinghe, S.; Smith, P. E. Kirkwood–Buff-Derived Force Field for Peptides and Proteins: Philosophy and Development of KBFF20. *J. Chem. Theory Comput.* **2021**, *17* (5), 2964–2990. https://doi.org/10.1021/acs.jctc.1c00075.

(20) Gee, M. B.; Cox, N. R.; Jiao, Y.; Bentenitis, N.; Weerasinghe, S.; Smith, P. E. A Kirkwood-Buff Derived Force Field for Aqueous Alkali Halides. *J. Chem. Theory Comput.* **2011**, *7* (5), 1369–1380. https://doi.org/10.1021/ct100517z.

(21) Kirkwood, J. G.; Buff, F. P. The Statistical Mechanical Theory of Solutions. I. *The Journal of Chemical Physics* **1951**, *19* (6), 774–777. https://doi.org/10.1063/1.1748352.

(22) Ben-Naim, A. Inversion of the Kirkwood–Buff Theory of Solutions: Application to the Water–Ethanol System. *The Journal of Chemical Physics* **1977**, *67* (11), 4884–4890. https://doi.org/10.1063/1.434669.

(23) Matteoli, E.; Lepori, L. Solute–Solute Interactions in Water. II. An Analysis through the Kirkwood–Buff Integrals for 14 Organic Solutes. *The Journal of Chemical Physics* **1984**, *80* (6), 2856–2863. https://doi.org/10.1063/1.447034.

(24) Robinson, R. A.; Stokes, R. H. *Electrolyte Solutions*; Courier Corporation, 2002.

(25) Campbell, A.; Debus, G.; Kartzmark, E. Conductances of Aqueous Lithium Nitrate Solutions at 25.0 C. and 110.0 C. *Canadian Journal of Chemistry* **1955**, *33* (10), 1508–1514.

(26) Isono, T. Density, Viscosity, and Electrolytic Conductivity of Concentrated Aqueous Electrolyte Solutions at Several Temperatures. Alkaline-Earth Chlorides, Lanthanum Chloride, Sodium Chloride, Sodium Nitrate, Sodium Bromide, Potassium Nitrate, Potassium Bromide, and Cadmium Nitrate. *Journal of chemical and engineering data* **1984**, *29* (1), 45–52.

(27) PubChem. *PubChem*. https://pubchem.ncbi.nlm.nih.gov/ (accessed 2024-01-30).

(28) Berendsen, H. J. C.; Grigera, J. R.; Straatsma, T. P. The Missing Term in Effective Pair Potentials. *J. Phys. Chem.* **1987**, *91* (24), 6269–6271. https://doi.org/10.1021/j100308a038.

(29) Wang, H.-W.; Vlcek, L.; Neuefeind, J. C.; Page, K.; Irle, S.; Simonson, J. M.; Stack, A. G. Decoding Oxyanion Aqueous Solvation Structure: A Potassium Nitrate Example at Saturation. *J. Phys. Chem. B* **2018**, *122* (30), 7584–7589. https://doi.org/10.1021/acs.jpcb.8b05895.

(30) Thøgersen, J.; Réhault, J.; Odelius, M.; Ogden, T.; Jena, N. K.; Jensen, S. J. K.; Keiding, S. R.; Helbing, J. Hydration Dynamics of Aqueous Nitrate. *J. Phys. Chem. B* **2013**, *117* (12), 3376–3388. https://doi.org/10.1021/jp310090u.

(31) *Welcome to the GROMACS documentation! — GROMACS documentation*. https://manual.gromacs.org/ (accessed 2024-02-17).

(32) Berendsen, H. J. C.; Grigera, J. R.; Straatsma, T. P. The Missing Term in Effective Pair Potentials. *J. Phys. Chem.* **1987**, *91* (24), 6269–6271. https://doi.org/10.1021/j100308a038.

(33) Nosé, S. A Unified Formulation of the Constant Temperature Molecular Dynamics Methods. *The Journal of Chemical Physics* **1984**, *81* (1), 511–519. https://doi.org/10.1063/1.447334.

(34) Parrinello, M.; Rahman, A. Polymorphic Transitions in Single Crystals: A New Molecular Dynamics Method. *Journal of Applied Physics* **1981**, *52* (12), 7182–7190. https://doi.org/10.1063/1.328693.

(35) Hess, B.; Bekker, H.; Berendsen, H. J. C.; Fraaije, J. G. E. M. LINCS: A Linear Constraint Solver for Molecular Simulations. *Journal of Computational Chemistry* **1997**, *18* (12), 1463–1472. https://doi.org/10.1002/(SICI)1096-987X(199709)18:12<1463::AID-JCC4>3.0.CO;2-H.

(36) *Settle: An analytical version of the SHAKE and RATTLE algorithm for rigid water models - Miyamoto - 1992 - Journal of Computational Chemistry - Wiley Online Library*. https://onlinelibrary.wiley.com/doi/abs/10.1002/jcc.540130805 (accessed 2024-05-15).

(37) Darden, T.; York, D.; Pedersen, L. Particle Mesh Ewald: An N·log(N) Method for Ewald Sums in Large Systems. *The Journal of Chemical Physics* **1993**, *98* (12), 10089–10092. https://doi.org/10.1063/1.464397.

(38) Megyes, T.; Bálint, S.; Peter, E.; Grósz, T.; Bakó, I.; Krienke, H.; Bellissent-Funel, M.-C. Solution Structure of NaNO3 in Water: Diffraction and Molecular Dynamics Simulation Study. *The Journal of Physical Chemistry B* **2009**, *113* (13), 4054–4064.

(39) Smith, P. E.; van Gunsteren, W. F. Consistent Dielectric Properties of the Simple Point Charge and Extended Simple Point Charge Water Models at 277 and 300 K. *The Journal of Chemical Physics* **1994**, *100* (4), 3169–3174. https://doi.org/10.1063/1.466407.

(40) *Analysis of Activity Coefficients in Aqueous Solutions of Alkali Metal Nitrates on the Basis of Dielectric Properties | Russian Journal of Inorganic Chemistry*. https://link.springer.com/article/10.1134/S0036023621070123 (accessed 2024-02-24).

(41) Hauner, I. M.; Deblais, A.; Beattie, J. K.; Kellay, H.; Bonn, D. The Dynamic Surface Tension of Water. *J. Phys. Chem. Lett.* **2017**, *8* (7), 1599–1603. https://doi.org/10.1021/acs.jpclett.7b00267.

(42) Matubayasi, N.; Yoshikawa, R. Thermodynamic Quantities of Surface Formation of Aqueous Electrolyte Solutions: VII. Aqueous Solution of Alkali Metal Nitrates LiNO3, NaNO3, and KNO3. *Journal of Colloid and Interface Science* **2007**, *315* (2), 597–600. https://doi.org/10.1016/j.jcis.2007.07.004.

Chapter 3 - A Kirkwood-Buff theory derived force field for aqueous alkaline earth nitrate solutions

3.1. Introduction:

Divalent alkaline earth metals are of considerable interest due to their presence in nature and biological systems. Due to their high charge density and closed-shell electronic structure, the hydration properties of the alkaline earth metals are easy to predict.[1] Thus, these ions offer a unique opportunity to investigate the effects of ion size and hydration behavior of divalent metal ions on DNA-ion binding.[1] In biology, alkaline earth metals are essential for physiological functions, contributing to bone integrity, nerve signaling, and enzyme activation.[2–4] These metals also play crucial roles in various industrial processes as fundamental elements in alloys, catalysts, and manufacturing techniques.[5] Moreover, in environmental remediation and water treatment, compounds derived from alkaline earth metals are used to address water hardness and counteract acidic conditions.[6] Additionally, alkaline earth metals feature prominently in sectors like healthcare, agriculture, construction, and technology, showcasing their indispensable contributions to advancing and sustaining life on our planet.[7–11]

Alkaline earth metal nitrates, compounds derived from alkaline earth metals like calcium, magnesium, strontium, and barium combined with nitrate ions, play a crucial role across numerous applications due to their versatile properties. These nitrates find significance in fields ranging from chemistry and agriculture to healthcare and industrial processes.[12] They serve as essential chemical reagents for various synthesis and analytical procedures.[13] In agriculture, calcium and magnesium

nitrates are vital fertilizers, providing essential nutrients for plant growth and improving crop yields.[14] Additionally, alkaline earth metal nitrates are used in flame tests to identify metal ions and pyrotechnic formulations to produce vibrant colors in fireworks displays. In healthcare, strontium nitrate has been explored for its potential in treating osteoporosis, highlighting the importance of alkaline earth metal nitrates in medicinal applications.[15] These compounds play a pivotal role in advancing technology, agriculture, and healthcare, underscoring their multifaceted importance in modern society.

Nitrate salts of most alkaline earth metals (Mg^{2+}, Ca^{2+}, and Sr^{2+}) have high solubility in water. Thus, there is plenty of experimental data available. However, due to their high charge density, the water residence time in the first solvation shell of these metals is quite long (~10 ns to 1 μs).[16–18] The μs time length is quite long and difficult to attain computationally. The simulations of hundreds of nanoseconds have difficulty capturing the contact ion pair formation of the metal nitrates, making the simulations difficult. Consequently, proper modeling of ion-pairing of alkaline earth cations with the nitrate ions in aqueous solutions is not easily found in the literature. One significant work was done by Yadav and Chandra.[19] They used the parameters for alkaline earth metals and the nitrate ion from two previous works.[20,21] They performed Electronic Continuum Correction (ECC)[22] to generate a non-polarizable force field and compared it with an explicitly polarizable force field simulation. Their ECC force field was able to reproduce experimental coordination numbers for $Mg(NO_3)_2$, $Ca(NO_3)_2$, and $Sr(NO_3)_2$ at relatively higher concentrations (>3m).

In this work we have established an alkaline earth metal nitrate force field. This is an extension of our alkali nitrate force field discussed in Chapter 2. By using a similar approach as provided in Chapter 2 one can have some confidence that the new models are compatible with our previous models. We take the force field parameters for alkaline earth metals from a previously published work of our group.[23] Our nitrate model is the same as described in Chapter 2. We have subsequently scaled the Lennard-Jones (LJ) parameters between the alkaline earth metal cation and the nitrate oxygen (ON). The SPC/E water model was used to also make this force field compatible with the KBFF20.[24,25]

3.2. Methods

3.2.1. Kirkwood Buff Analysis of the Experimental Data

The Kirkwood Buff (KB) analysis of the experimental data involves the same approach as used in Chapter 2. Below is a table with references for the experimental activity coefficient and density data for Mg, Ca, and Sr nitrate salts.

Compound	Activity Coefficient Reference	Density Reference	Temperature (K)	Pressure
$Mg(NO_3)_2$	[26]	[27]	298	-
$Ca(NO_3)_2$	[26]	[28]	298	-
$Sr(NO_3)_2$	[26]	[27]	298	-

Table 3.1. References for the activity coefficients and the density data for alkaline earth nitrates

We could not study $Be(NO_3)_2$ due to its covalent nature and little-known chemistry.[29] $Ba(NO_3)_2$ was excluded from the study due to its low solubility in water.[30] The activity coefficient and the density data were fitted using the polynomial equations provided in Chapter 2 to obtain the experimental KB integrals (KBIs). These KBIs were used as data to optimize FF for alkaline earth nitrates.

3.2.2. Parameterization of nitrate ion and alkaline earth metal ions

Parameters for the nitrate ion were taken from Chapter 2. The nitrate ion parameters are given in Table 3.2. Alkaline earth metal ion parameters were developed in a previous work of our group and then added to KBFF20.[23–25] The LJ σ parameter was already set in KBFF20 for the alkaline earth metal cations. The initial LJ ϵ parameter was taken from KBFF20 and then scaled by multiplying with a scaling factor (s) with respect to the ϵ value of ON to reproduce experimental

KBIs. The initial and final values of the LJ parameters are provided in Table 3.3. To calculate the LJ interaction between unlike atoms, the geometric combination rule was then used.

Atom	Charge	σ (nm)	ϵ (kJ/mol)
N	+0.65	0.3201	0.5620
ON	-0.55	0.3465	0.6047

Table 3.2. Nitrate ion charges and LJ parameters taken from Chapter 2

Cation	σ(nm) (original)	ϵ(kJ/mol) (original)	ϵ(kJ/mol) (scaled)	ON-Cation scaling factor (s)
Mg	0.2697	0.7500	0.0842	0.125
Ca	0.3170	0.4700	0.1333	0.25
Sr	0.3277	0.5000	0.2062	0.375

Table 3.3. Initial and final alkaline earth metal LJ parameters and the scaling factors

3.2.3. Molecular Dynamics Simulation Details

All the molecular dynamics (MD) simulation details were the same as in Chapter 2. The initial random configuration generation for 1m, 2m, 3m, and 4m alkaline earth nitrate aqueous solution was generated using custom-made Fortran code. After the MD simulation, further data analysis was also performed using Fortran codes.

3.3. Results and Discussion

Our initial studies focused on the cation to nitrate oxygen scaling factor and whether that can be used to reproduce both the KBIs and the degree of contact ion pairing. The cation-oxygen RDFs for all three systems are displayed in Figure 3.1. The contact ion pair peak is missing for Mg nitrate while it is present for both Ca and Sr nitrate solutions becoming more substantial as the metal size increases and the desolvation penalty is reduced. Integration of these RDFs provides the ion-ion KBIs and coordination numbers listed in Table 3.4. Both the KBIs and coordination numbers are in reasonable agreement with experiment at this concentration. This provides some confidence in the current approach and the also the distributions illustrated in Figure 3.1.

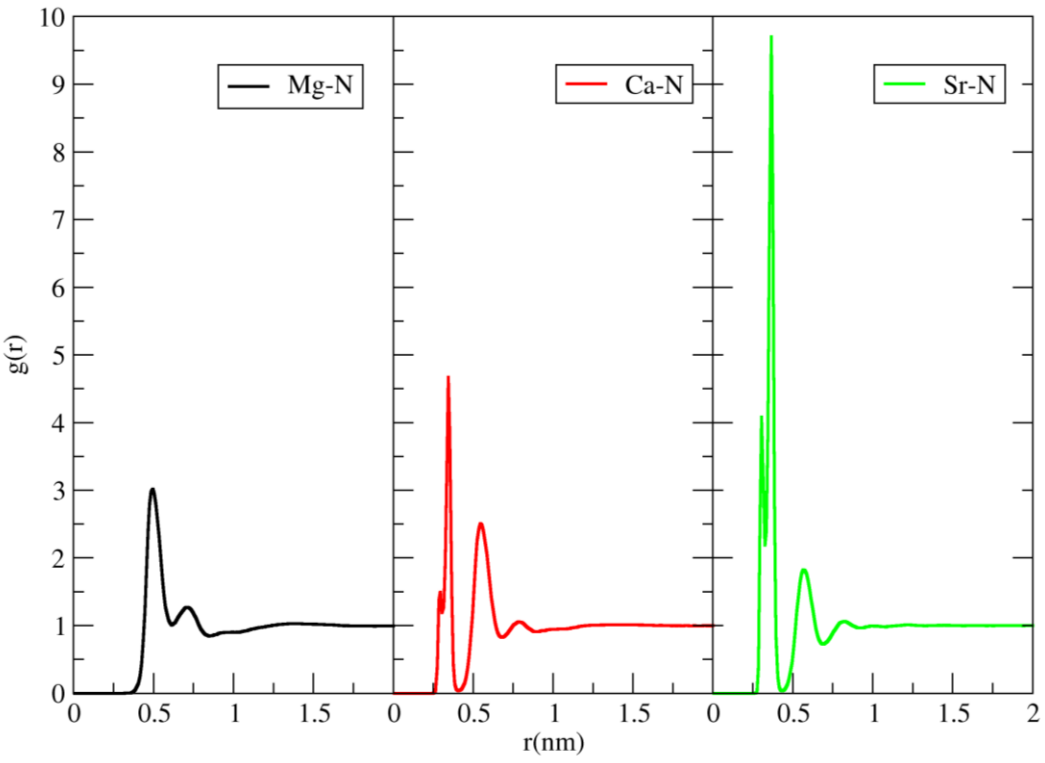

Figure 3.1. Cation to N rdfs for aqueous 2m metal nitrate solutions.

Compound	Experimental G_{22}(cm^3/mol)	Simulated G_{22} (cm^3/mol)	Experimental Coordination Number	Reference	Simulated Coordination Number
$Mg(NO_3)_2$	-114	-116	0.02-0.03	[19]	0.00
$Ca(NO_3)_2$	-58	-82	0.17-0.24	[19]	0.10
$Sr(NO_3)_2$	9	25	0.23-0.42	[19]	0.30

Table 3.4. Experimental and simulated KBIs and coordination numbers for 2m aqueous Mg, Ca, and Sr nitrate solutions

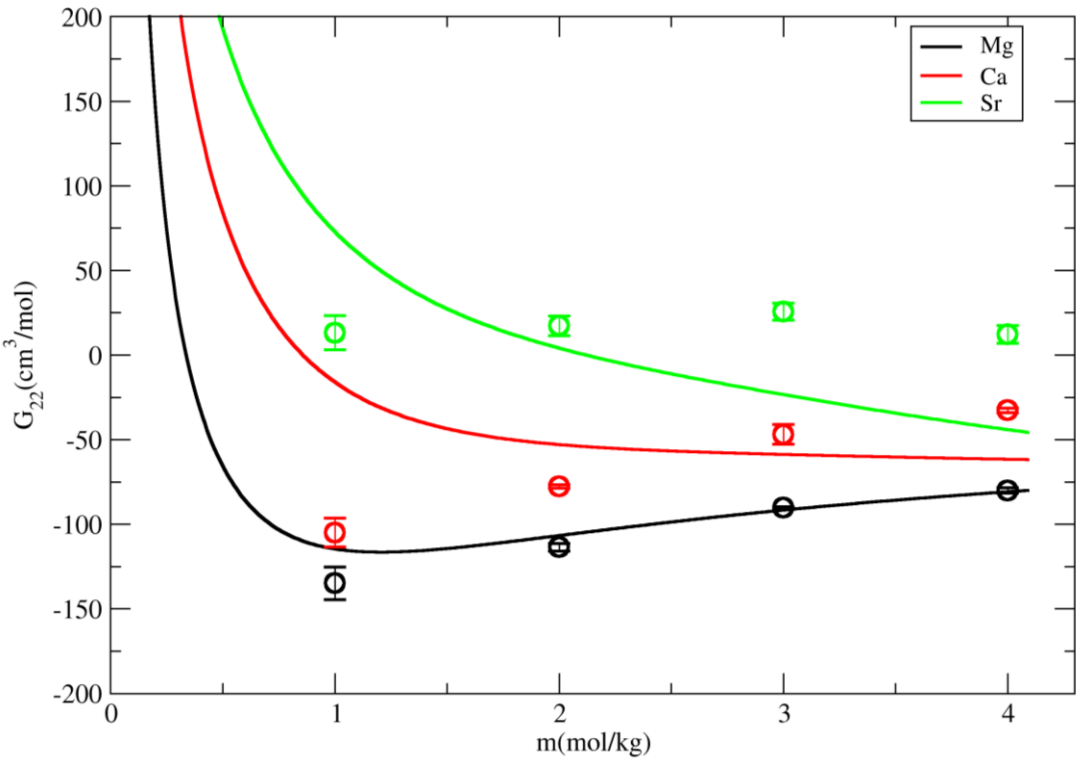

Figure 3.2. Solute-solute KBIs for aqueous alkaline earth nitrate solutions (lines: exp, symbols: simulation).

The solute-solute KBIs from simulation and experiment are displayed in Figure 3.2 as a function of salt molality. For $Mg(NO_3)_2$, the KBIs were well reproduced for the whole concentration range, while for $Ca(NO_3)_2$ the KBIs gave good results at ≥2m concentrations. In all cases and concentrations the experimental trend between the different cations was reproduced.

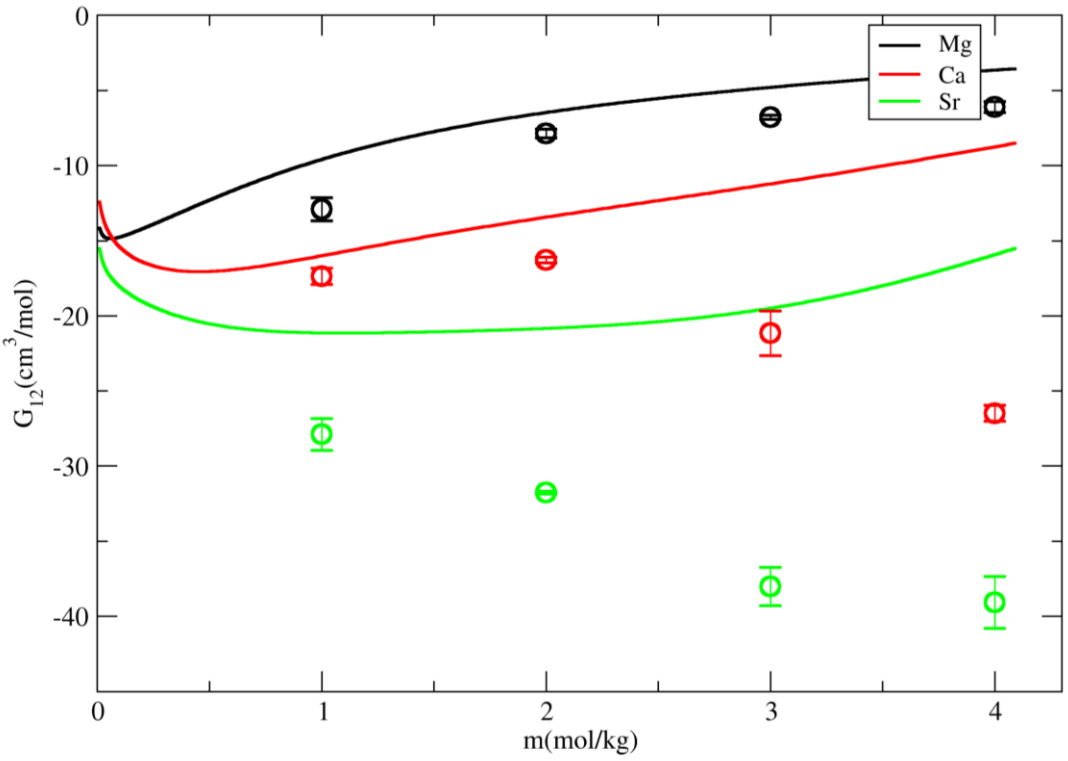

Figure 3.3. Solvent-solute KBIs for aqueous alkaline earth nitrate solutions (lines: exp, symbols: simulation).

In Figure 3.3, the correct trends in the KBIs were maintained up to 2m concentration for Magnesium and Calcium nitrates. While, for $Mg(NO_3)_2$, the trend was maintained for the whole concentration range. The reason for the differences is unclear. The water residence time surrounding the Mg^{2+} ions is relatively high (~10 ns to 1 μs).[19] So, the thermodynamic interaction between water molecules and Mg^{2+} ions appears to be captured quite well even if the exchange of waters is infrequent.

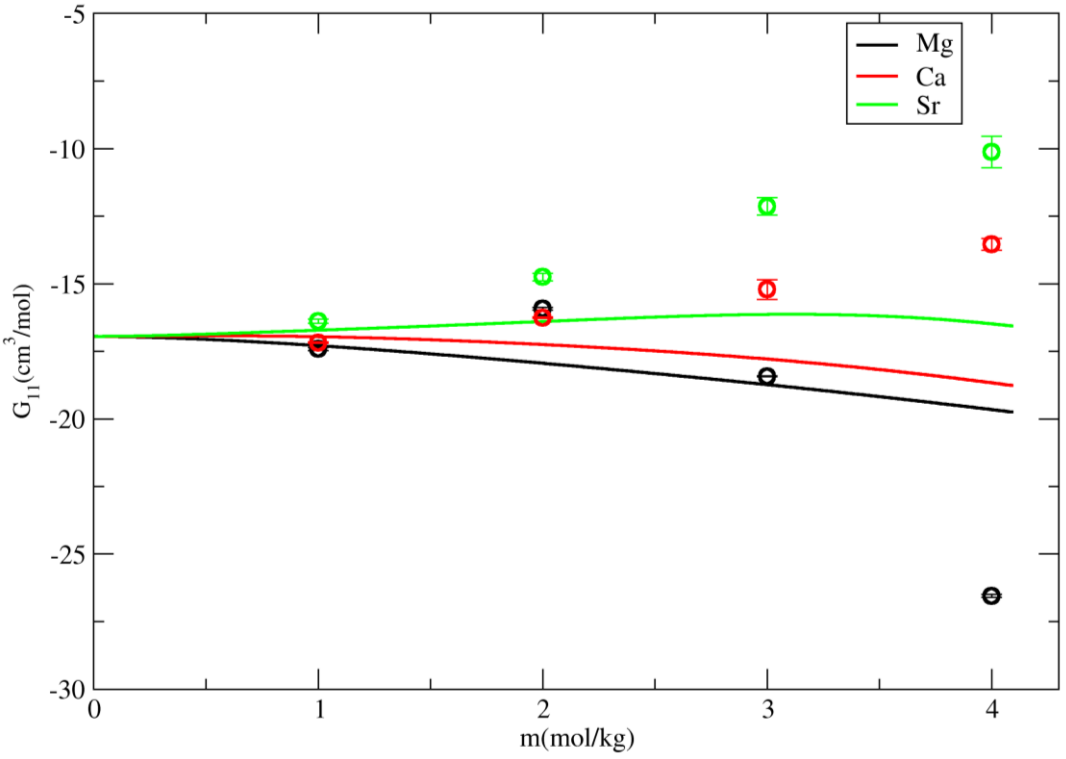

Figure 3.4. Solvent-solvent KBIs for aqueous alkaline earth nitrate systems (lines: exp, symbols: simulation).

The solvent-solvent KBIs are provided in Figure 3.4. At lower concentrations (1m), the solvent-solvent KBIs were quite well reproduced. As the concentration increased, a positive deviation from the experimental data was observed, except for the $Mg(NO_3)_2$, at 4m concentration, where a negative deviation was observed. Comparison of all three sets of KBI data suggest that the properties of $Sr(NO_3)_2$ aqueous solutions cannot be predicted as accurately as those of $Mg(NO_3)_2$ and $Ca(NO_3)_2$ aqueous solutions, especially at higher concentrations.

The surface tension of the $Ca(NO_3)_2$ aqueous solution was calculated at different concentrations. Only $Ca(NO_3)_2$ was studied as it appears the surface tension changes for the other two nitrate solutions is unavailable. Chapter 2 describes the simulation process. Salts that are soluble in water increase the water's surface tension due to surface exclusion.[31] The trend was reproduced in our simulations. However, the effect was over-estimated with our model.

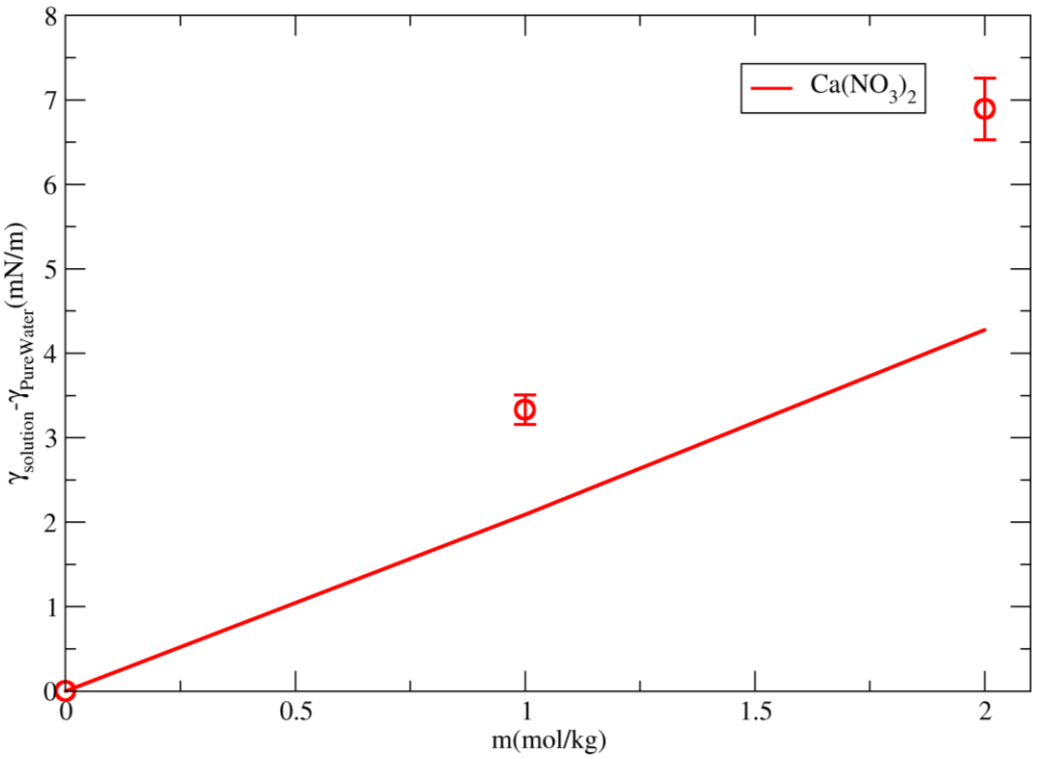

Figure 3.5. Change in surface tension with concentration for Calcium Nitrate solutions (lines: exp,[32] symbols: KBFF).

3.4. Conclusions

In this chapter, we have described the development of an aqueous alkaline earth nitrate force field. We have taken the nitrate model from aqueous alkali nitrates (chapter 2) and adapted it for the aqueous alkaline earth nitrates by scaling the LJ parameters between the alkaline earth metal cation and the nitrate oxygen (ON). This process was insufficient to fully reproduce characteristics of all the aqueous alkaline earth nitrate solutions over all concentrations. However, the results for Mg nitrate are very reasonable and the results for the other metal nitrates at lower concentrations were also more acceptable. The lack of aqueous alkaline earth nitrate FFs in the literature has already suggested that it is not easy to model these compounds. Different methods may need to be developed in order to build a FF for these compounds.

3.5. References

(1) Provorse Long, M.; Alland, S.; E. Martin, M.; M. Isborn, C. Molecular Dynamics Simulations of Alkaline Earth Metal Ions Binding to DNA Reveal Ion Size and Hydration Effects. *Physical Chemistry Chemical Physics* **2020**, *22* (10), 5584–5596. https://doi.org/10.1039/C9CP06844A.

(2) Alnuaimi, M. M.; Saeed, I. A.; Ashraf, S. S. Effect of Various Heavy Metals on the Enzymatic Activity of E. Coli Alkaline Phosphatase. *Int J Biotechnol Biochem* **2012**, *8*, 47–59.

(3) Jomova, K.; Makova, M.; Alomar, S. Y.; Alwasel, S. H.; Nepovimova, E.; Kuca, K.; Rhodes, C. J.; Valko, M. Essential Metals in Health and Disease. *Chemico-Biological Interactions* **2022**, *367*, 110173. https://doi.org/10.1016/j.cbi.2022.110173.

(4) Yin, J.; Hu, Y.; Yoon, J. Fluorescent Probes and Bioimaging: Alkali Metals, Alkaline Earth Metals and pH. *Chemical Society Reviews* **2015**, *44* (14), 4619–4644. https://doi.org/10.1039/C4CS00275J.

(5) Arzamendi, G.; Arguiñarena, E.; Campo, I.; Zabala, S.; Gandía, L. M. Alkaline and Alkaline-Earth Metals Compounds as Catalysts for the Methanolysis of Sunflower Oil. *Catalysis Today* **2008**, *133–135*, 305–313. https://doi.org/10.1016/j.cattod.2007.11.029.

(6) Miró, M.; Estela, J. M.; Cerdà, V. Application of Flowing Stream Techniques to Water Analysis: Part III. Metal Ions: Alkaline and Alkaline-Earth Metals, Elemental and

Harmful Transition Metals, and Multielemental Analysis. *Talanta* **2004**, *63* (2), 201–223. https://doi.org/10.1016/j.talanta.2003.10.047.

(7) Pathak, P.; Srivastava, R. R.; Keceli, G.; Mishra, S. Assessment of the Alkaline Earth Metals (Ca, Sr, Ba) and Their Associated Health Impacts. In *Strontium Contamination in the Environment*; Pathak, P., Gupta, D. K., Eds.; Springer International Publishing: Cham, 2020; pp 227–243. https://doi.org/10.1007/978-3-030-15314-4_12.

(8) Tyopine, A. A.; Sikakwe, G. U.; Obalum, S. E.; Okoye, C. O. B. Relative Distribution of Rare-Earth Metals alongside Alkaline Earth and Alkali Metals in Rhizosphere of Agricultural Soils in Humid Tropical Environment. *Environ Monit Assess* **2020**, *192* (8), 504. https://doi.org/10.1007/s10661-020-08437-5.

(9) Alcazar-Ruiz, A.; Ortiz, M. L.; Sanchez-Silva, L.; Dorado, F. Catalytic Effect of Alkali and Alkaline Earth Metals on Fast Pyrolysis Pre-Treatment of Agricultural Waste. *Biofuels, Bioproducts and Biorefining* **2021**, *15* (5), 1473–1484. https://doi.org/10.1002/bbb.2253.

(10) Tsukada, H.; Hasegawa, H.; Hisamatsu, S. Distributions of Alkali and Alkaline Earth Metals in Several Agricultural Plants. *Radioprotection Collogues* **2002**, *37*, 535–540.

(11) Vodyanitskii, Yu. N.; Savichev, A. T.; Vasil'ev, A. A.; Lobanova, E. S.; Chashchin, A. N.; Prokopovich, E. V. Contents of Heavy Alkaline-Earth (Sr, Ba) and Rare-Earth (Y, La, Ce) Metals in Technogenically Contaminated Soils. *Eurasian Soil Sc.* **2010**, *43* (7), 822–832. https://doi.org/10.1134/S1064229310070136.

(12) Lahijani, P.; Zainal, Z. A.; Mohamed, A. R.; Mohammadi, M. CO2 Gasification Reactivity of Biomass Char: Catalytic Influence of Alkali, Alkaline Earth and Transition Metal Salts. *Bioresource Technology* **2013**, *144*, 288–295. https://doi.org/10.1016/j.biortech.2013.06.059.

(13) Batta-Mpouma, J.; Kandhola, G.; Kim, J.-W. Ionically Crosslinked Cellulose Nanocrystals by Metal Nitrates for the Preparation of Stable Emulsions with Tunable Interface Properties. *Sci Rep* **2023**, *13* (1), 21630. https://doi.org/10.1038/s41598-023-48703-3.

(14) Addiscott, T. M. *Nitrate, Agriculture and the Environment*; CABI, 2005.

(15) Cooper, C.; Fox, K. M.; Borer, J. S. Ischaemic Cardiac Events and Use of Strontium Ranelate in Postmenopausal Osteoporosis: A Nested Case–Control Study in the CPRD. *Osteoporos Int* **2014**, *25* (2), 737–745. https://doi.org/10.1007/s00198-013-2582-4.

(16) Neely, J.; Connick, R. Rate of Water Exchange from Hydrated Magnesium Ion. *J. Am. Chem. Soc.* **1970**, *92* (11), 3476–3478. https://doi.org/10.1021/ja00714a048.

(17) Helm, L.; Merbach, A. E. Inorganic and Bioinorganic Solvent Exchange Mechanisms. *Chem. Rev.* **2005**, *105* (6), 1923–1960. https://doi.org/10.1021/cr030726o.

(18) Callahan, K. M.; Casillas-Ituarte, N. N.; Roeselová, M.; Allen, H. C.; Tobias, D. J. Solvation of Magnesium Dication: Molecular Dynamics Simulation and Vibrational Spectroscopic Study of Magnesium Chloride in Aqueous Solutions. *J. Phys. Chem. A* **2010**, *114* (15), 5141–5148. https://doi.org/10.1021/jp909132a.

(19) Yadav, S.; Chandra, A. Preferential Solvation, Ion Pairing, and Dynamics of Concentrated Aqueous Solutions of Divalent Metal Nitrate Salts. *The Journal of Chemical Physics* **2017**, *147* (24), 244503. https://doi.org/10.1063/1.4996273.

(20) Mamatkulov, S.; Fyta, M.; Netz, R. R. Force Fields for Divalent Cations Based on Single-Ion and Ion-Pair Properties. *The Journal of Chemical Physics* **2013**, *138* (2), 024505. https://doi.org/10.1063/1.4772808.

(21) Baaden, M.; Burgard, M.; Wipff, G. TBP at the Water−Oil Interface: The Effect of TBP Concentration and Water Acidity Investigated by Molecular Dynamics Simulations. *J. Phys. Chem. B* **2001**, *105* (45), 11131–11141. https://doi.org/10.1021/jp011890n.

(22) Leontyev, I.; Stuchebrukhov, A. Accounting for Electronic Polarization in Non-Polarizable Force Fields. *Phys. Chem. Chem. Phys.* **2011**, *13* (7), 2613–2626. https://doi.org/10.1039/C0CP01971B.

(23) Naleem, N.; Bentenitis, N.; Smith, P. E. A Kirkwood-Buff Derived Force Field for Alkaline Earth Halide Salts. *The Journal of Chemical Physics* **2018**, *148* (22), 222828. https://doi.org/10.1063/1.5019454.

(24) Ploetz, E. A.; Karunaweera, S.; Bentenitis, N.; Chen, F.; Dai, S.; Gee, M. B.; Jiao, Y.; Kang, M.; Kariyawasam, N. L.; Naleem, N.; Weerasinghe, S.; Smith, P. E. Kirkwood–Buff-Derived Force Field for Peptides and Proteins: Philosophy and Development of KBFF20. *J. Chem. Theory Comput.* **2021**, *17* (5), 2964–2990. https://doi.org/10.1021/acs.jctc.1c00075.

(25) Ploetz, E. A.; Karunaweera, S.; Smith, P. E. Kirkwood–Buff-Derived Force Field for Peptides and Proteins: Applications of KBFF20. *J. Chem. Theory Comput.* **2021**, *17* (5), 2991–3009. https://doi.org/10.1021/acs.jctc.1c00076.

(26) Robinson, R. A.; Stokes, R. H. *Electrolyte Solutions*; Courier Corporation, 2002.

(27) Jones, J. S.; Ziemer, S. P.; Brown, B. R.; Woolley, E. M. Apparent Molar Volumes and Apparent Molar Heat Capacities of Aqueous Magnesium Nitrate, Strontium Nitrate, and Manganese Nitrate at Temperatures from 278.15 K to 393.15 K and at the Pressure 0.35 MPa. *The Journal of Chemical Thermodynamics* **2007**, *39* (4), 550–560. https://doi.org/10.1016/j.jct.2006.09.008.

(28) Ewing, W. W.; Mikovsky, R. J. Calcium Nitrate. V. Partial Molal Volumes of Water and Calcium Nitrate in Concentrated Solutions. *J. Am. Chem. Soc.* **1950**, *72* (3), 1390–1393. https://doi.org/10.1021/ja01159a086.

(29) W. Rudolph, W.; Fischer, D.; Irmer, G.; C. Pye, C. Hydration of Beryllium(Ii) in Aqueous Solutions of Common Inorganic Salts . A Combined Vibrational Spectroscopic and Ab Initio Molecular Orbital Study. *Dalton Transactions* **2009**, *0* (33), 6513–6527. https://doi.org/10.1039/B902481F.

(30) Aghaie, M.; Aghaie, H.; Ebrahimi, A. Thermodynamics of the Solubility of Barium Nitrate in the Mixed Solvent, Ethanol+ Water, and the Related Ion-Association. *Journal of molecular liquids* **2007**, *135* (1–3), 72–74.

(31) Hauner, I. M.; Deblais, A.; Beattie, J. K.; Kellay, H.; Bonn, D. The Dynamic Surface Tension of Water. *J. Phys. Chem. Lett.* **2017**, *8* (7), 1599–1603. https://doi.org/10.1021/acs.jpclett.7b00267.

(32) Matubayasi, N.; Yoshikawa, R. Thermodynamic Quantities of Surface Formation of Aqueous Electrolyte Solutions: VII. Aqueous Solution of Alkali Metal Nitrates LiNO3, NaNO3, and KNO3. *Journal of Colloid and Interface Science* **2007**, *315* (2), 597–600. https://doi.org/10.1016/j.jcis.2007.07.004.

Chapter 4 - Selective binding of alkali metals at neutral and charged surfaces

4.1. Introduction:

An electrolyte near a charged surface is ubiquitous in Chemistry. There has been extensive research on single electrolytes near a charged surface, compared to mixed electrolytes, despite the fact that mixed electrolytes are more prevalent in nature and technology. The study of mixed electrolytes can provide valuable insights into the behavior of complex systems. By examining the interactions between different ions in a solution, scientists can gain a better understanding of fundamental principles such as chemical equilibria, thermodynamics, and kinetics. These principles are essential for advancing knowledge in various fields of Chemistry. Mixed electrolytes are crucial in Chemistry for many reasons. It is possible to manipulate and adjust various properties such as conductivity, viscosity, solubility, and chemical reactivity by mixing electrolytes. This is particularly important in industrial processes where fine-tuning these properties can optimize efficiency and productivity. Mixed electrolytes are important in many electrochemical applications, such as batteries, fuel cells, and supercapacitors. Mixing different electrolytes can help control ion transport, which is important for device function. For example, in battery electrolytes, mixing different salts enhances conductivity while maintaining stability.[1,2] In analytical chemistry and sensor applications, mixed electrolytes can be used to create selective ion sensors. By carefully choosing the combination of electrolytes, it is possible to design sensors that respond specifically to specific ions, enabling accurate detection and quantification of target

species in complex mixtures. Due to all of these applications, theoretical interest has also grown in the area of mixed electrolytes since the beginning of the 21st century.[3–13]

In Computational Chemistry, simulating mixed electrolytes near a charged surface is complex yet crucial. Using a Monte-Carlo simulation process, Lamperski and Outhwaite showed that better modelling of the electrolyte mixtures and the charged surface is required to get closer agreement with experiment.[14] Co-ion and ion competition effects close to a charged and uncharged solid hydrophobic surface were simulated by Lima et al.[9] In their simulation, they used a polarizable model to include the co-ion effect in the theory of the ionic dispersion potential. Schmickler et al. have used molecular dynamics simulation to study the approach of alkali metal ions toward an electrode surface.[15] They simulated each alkali halide individually near a gold electrode and described their structure-making or breaking properties. An excellent perspective on the effects of cations on the metal/water interface and the selectivity of electrocatalytic processes was recently given by Waegele et al.[16]

Our study aims to simulate mixed electrolytes with a common ion near a charged gold electrode. We have selected the relatively simpler but widely applicable alkali metal chlorides as the electrolyte choice. In a mixture of ions of different sizes and charge densities, the structure of the electrode-electrolyte interface becomes much more complicated. Knowing how different ions approach a charged electrode in a mixture of electrolytes could be groundbreaking in electrochemical applications such as batteries. One of the problems in the field is the quantification of the ion effects. While the surface-ion distribution functions are often of interest, these vary with distance and hence the exact features that might be relevant are sometimes unclear. Here, we use

the Kirkwood-Buff theory of solutions to help quantify the charge neutralization and interactions of various ions with a negatively charged electrode.

4.2. Methods

The MD simulations were conducted using the GROMACS 2019.5 software package.[17] All the simulations were performed using the KBFF20 force field,[18] together with the SPC/E water model.[19] Figure 4.1 provides a snapshot of the simulation box, illustrating the setup. The box size was (9.2288 x 8.9914 x 44.1627) nm^3. The system consisted of six layers of Au (111) on both sides, with the aqueous mixed electrolyte solution sandwiched between the innermost layers of Au. The Au LJ parameters (σ=0.2629 nm and ϵ=0.1 kJ/mol) were chosen to provide an essentially repulsive plate. The aqueous solution was either 2M pure MCl (M = Li/ Na/ K/ Rb/ Cs) or a mixture of 1M M′Cl + 1M NaCl (M′= Li/ K/ Rb/ Cs). To eliminate the periodicity effects in the z-direction,[19] the box was extended by 14.7209 nm on both sides of the box along the z-axis.

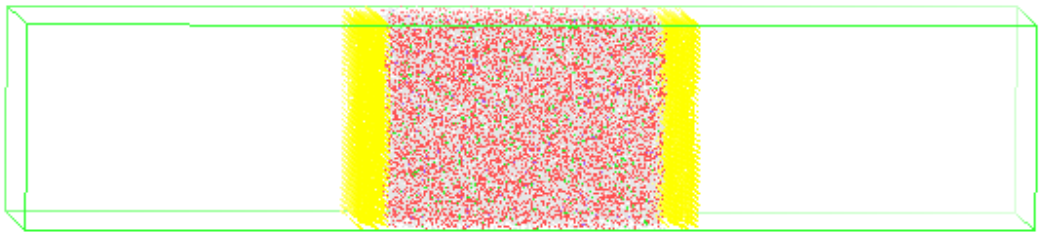

Figure 4.1. A snapshot of the simulation setup where aqueous 2M MCl solution is sandwiched between six layers of Au(111) on both sides. The box has an extended vacuum region on both sides. A fixed charge is applied to the inner layer of Au atoms.

The system was maintained under constant NVT conditions (Canonical ensemble). The temperature was maintained at 300K using a Nosè-Hoover thermostat.[20] All bonds were constrained using the SETTLE algorithm.[21] The Au layers were frozen in space using the freeze group option in the mdp file. A 2 fs time step was used to integrate the equations of motion. The particle mesh Ewald (PME) was used to model electrostatic interactions with a 1 nm cut-off distance for real space calculation and a 1 nm cut-off distance for the van der Waals interactions.[22] For all the simulation procedures, an equal and opposite charge of 0/0.25/0.50 e/nm^2 was applied on the innermost layers of the Au plates on both sides. The steepest descent method was used for three (1000-step each) energy minimization processes, followed by 1 ns equilibration. All the production runs were 100 ns long. In the production run, the first 20 ns were further discarded as part of the equilibration process, and the rest of the 80 ns were divided into chunks of 20 ns to perform a simple error analysis. In the production run, configurations were saved every 10 ps.

As we were concerned about the behavior of cations near a charged surface, we picked the negative side of the Au layers to perform analysis. The accumulation of the cations is supposed to take place near the negatively charged surface. The data were analyzed using custom-written FORTRAN code. The radial distribution functions (RDF) and the Kirkwood-Buff Integrals (KBI) were calculated with respect to the surface of the innermost Au layers.

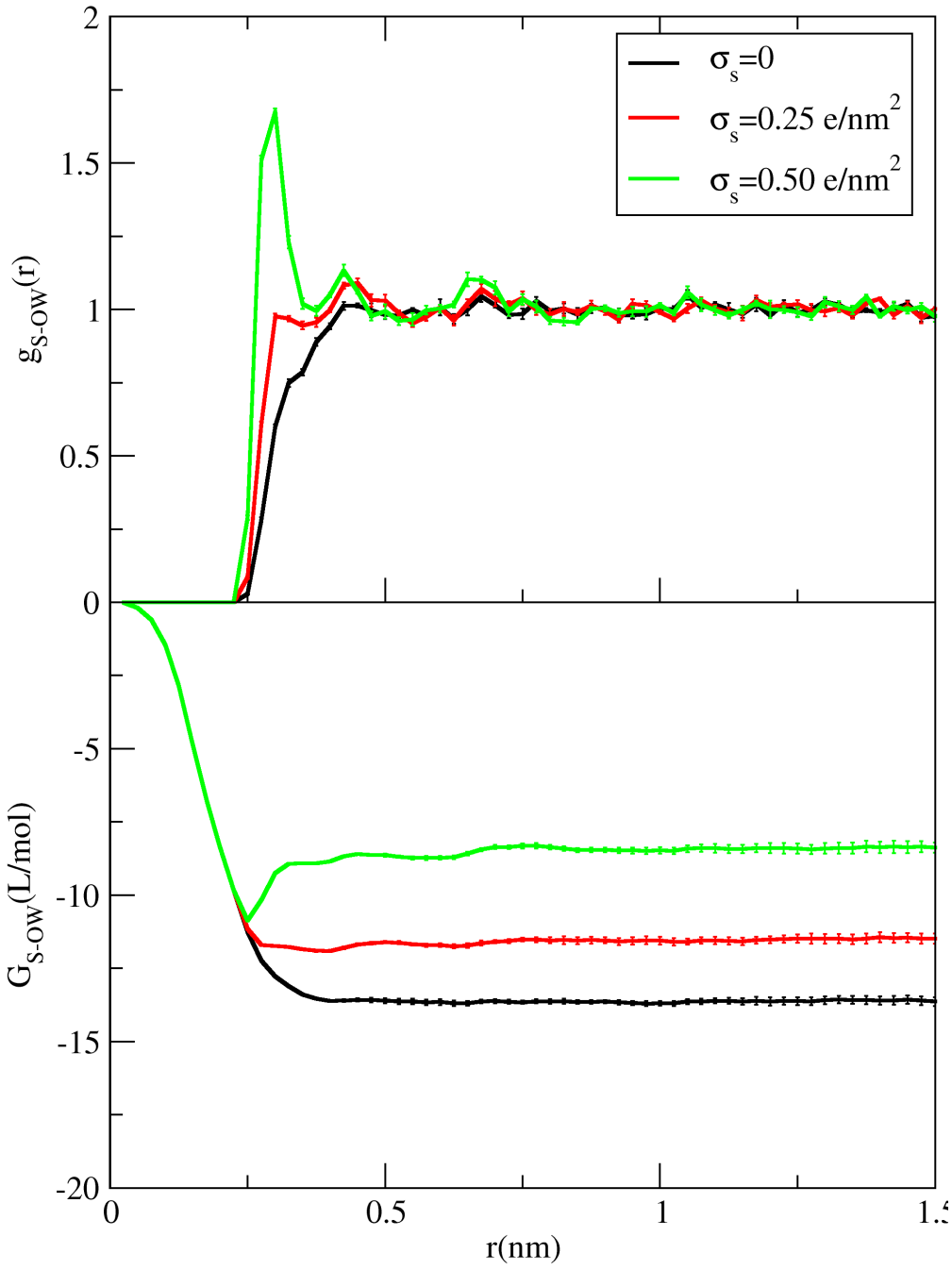

Figure 4.2. The top panel shows surface-OW distribution functions at three different charge densities (σ_s), and the bottom panel shows the corresponding KBIs as a function of integration distance for the aqueous 2M $LiNO_3$ system. All other systems showed very similar results.

We are primarily interested in the (integrated) cation distributions from the surface (S). These are given by,

$$G_{S\alpha} = A\int_0^{\infty}[g_{S\alpha}(z)-1]\ dz \tag{4.1}$$

where *A* is the surface area of the plate. However, due to the subtraction of unity, the value of these integrals depends on the origin. While the z coordinate of Au atoms closest to the solvent is a logical choice, we have taken the approach used in vapor/liquid studies where the solvent distribution is subtracted from the solute distribution in order to relate the results to thermodynamic quantities.[23] Figure 4.2 shows the S-OW RDFs and KBIs for different charges. The KBI values were taken based on the linear region of the KBI plot. Essentially the same results were obtained for all the salts in this study. The S-OW KBIs obtained were -13, -12, and -8 L/mol for zero, medium, and large charge density simulations. The Au surface-OW(SW) KBI values were subtracted from the original KBIs, and the value obtained was divided by the area of the Au surface (9.2288 x 8.9914) nm^2. The relation is provided in equation 4.1,

$$\Delta G_{SX} = (G_{SX} - G_{SW}) / A \tag{4.2}$$

Consequently, the final KBI values had a unit of $Lmol^{-1}nm^{-2}$ and are independent of an origin outside the solvent and the exact surface area used in the simulations.

4.3. Results and Discussion

The simulations performed contained either aqueous 2M pure MCl (M = Li/ Na/ K/ Rb/ Cs) or a mixture of aqueous of 1M NaCl with 1M M′Cl (M′ = Li/ K/ Rb/ Cs). The resulting RDFs and KBIs for different charge densities for an aqueous 2M LiCl solution are given in Figure 4.3.

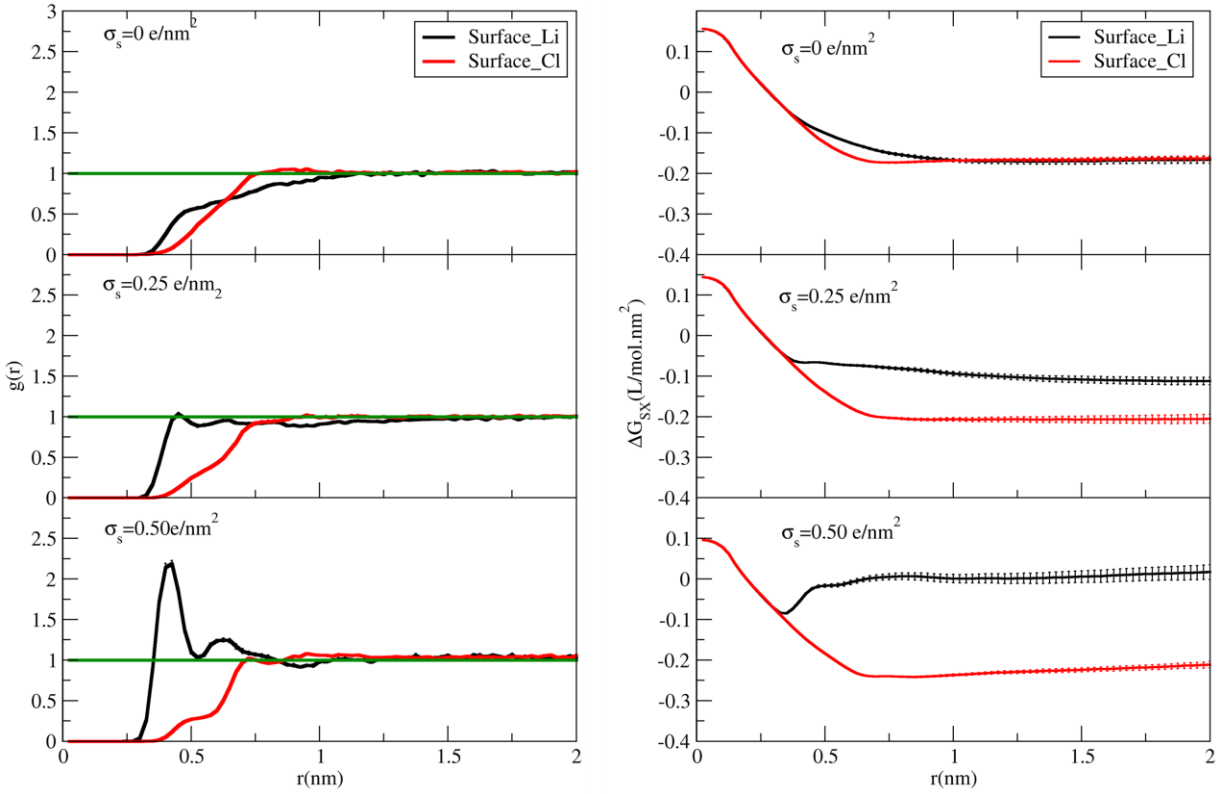

Figure 4.3. Distribution functions (left) and KBIs (right) for an aqueous 2M LiCl solution with respect to the Au surface at different charge densities.

As shown in Figure 4.3, the KBI values for Li and Cl were negative at zero charge, indicating the depletion of ions near the Au surface compared to water. They were also equal in magnitude, which is expected due to charge neutrality away from the neutral surface. .As the negative charge on the

surface increased, the KBI values for the Li ions increased, and the KBI values for the Cl ions became slightly more negative. Similar behavior was observed in the case of other 2M aqueous MCl solutions. When a single electrolyte is present between the Au plates and equal and opposite charges are applied on the innermost layers of the Au plates, the negative ions will move towards the positively charged Au layer and vice-versa. Similar results were obtained for other 2M salt solutions as shown in Figures 4.4 to 4.7.

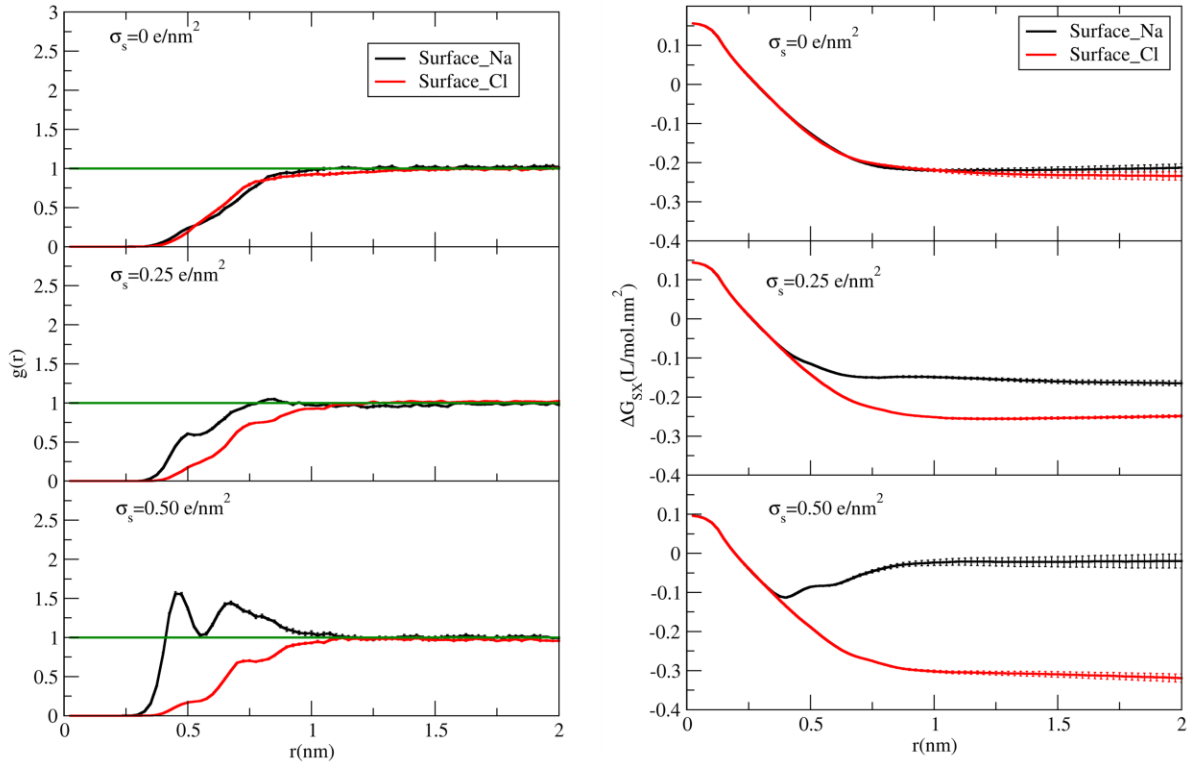

Figure 4.4. Distribution functions (left) and KBIs (right) for an aqueous 2M NaCl solution with respect to the Au surface at different charge densities.

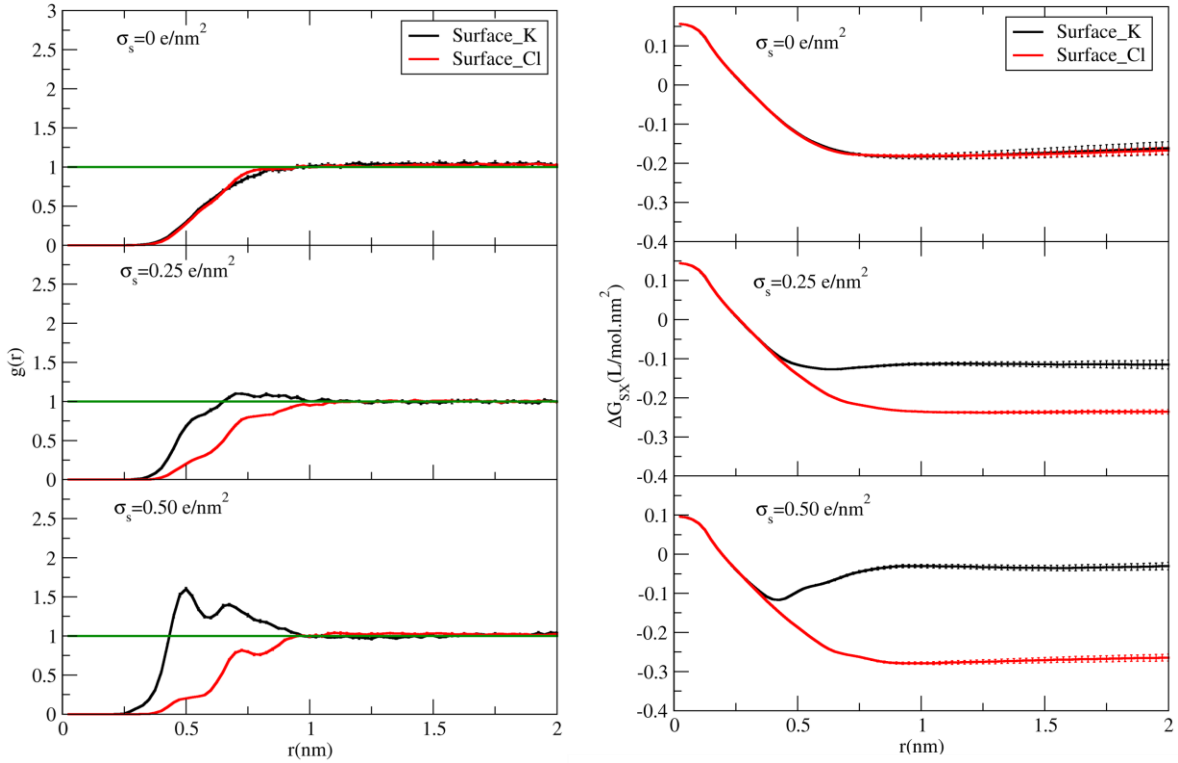

Figure 4.5. Distribution functions (left) and KBIs (right) for an aqueous 2M KCl solution with respect to the Au surface at different charge densities.

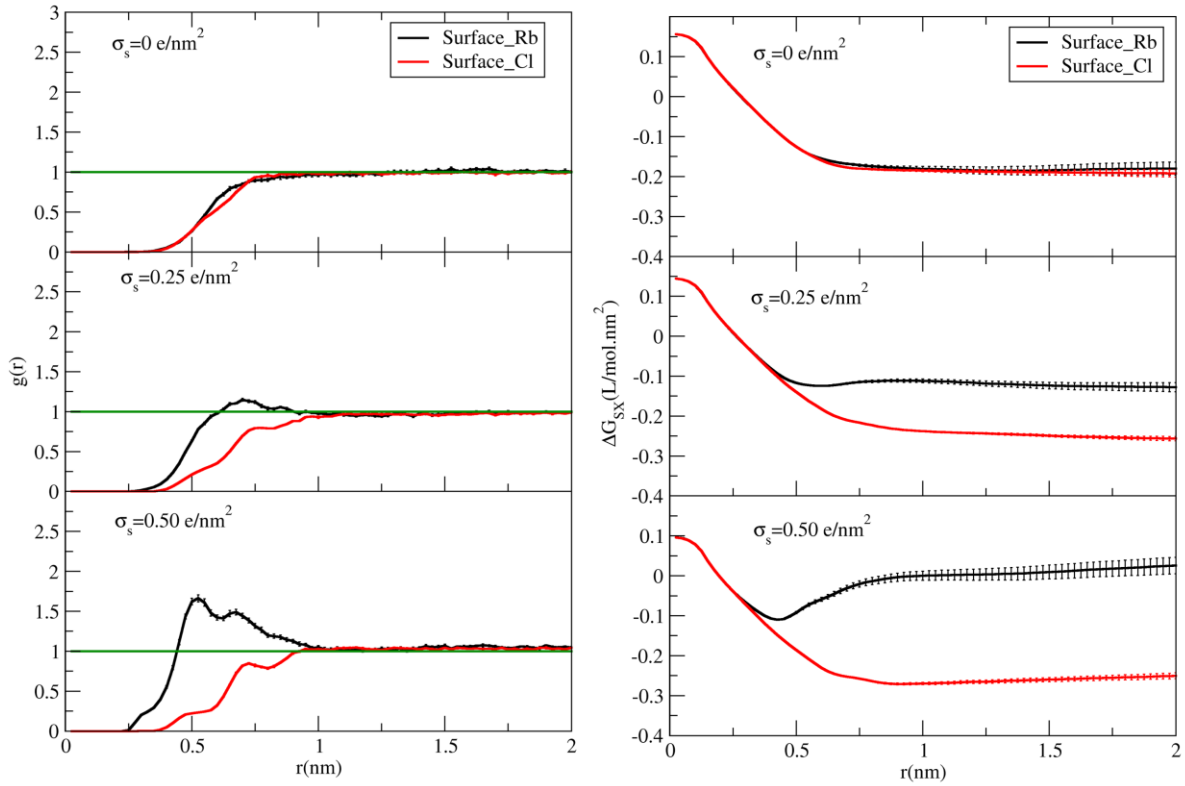

Figure 4.6. Distribution functions (left) and KBIs (right) for an aqueous 2M RbCl solution with respect to the Au surface at different charge densities.

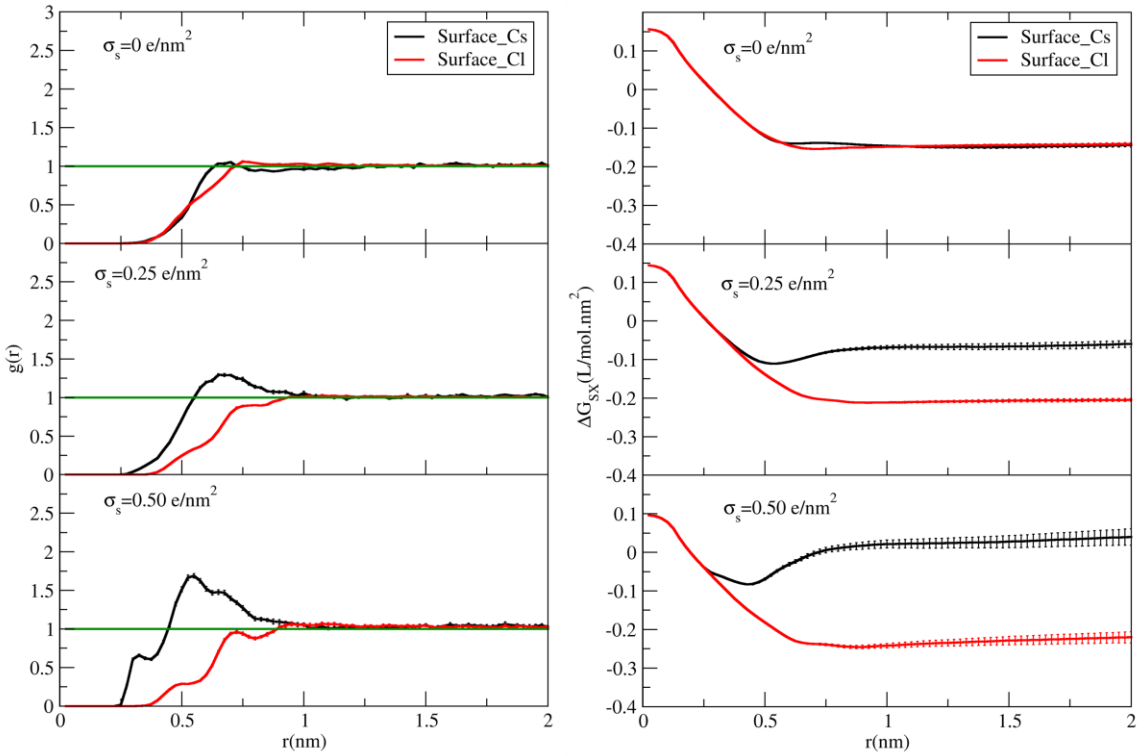

Figure 4.7. Distribution functions (left) and KBIs (right) for an aqueous 2M CsCl solution with respect to the Au surface at different charge densities.

The overall results for the KBIs are summarized in Figure 4.8. The higher the KBI, the higher the attraction with the surface.

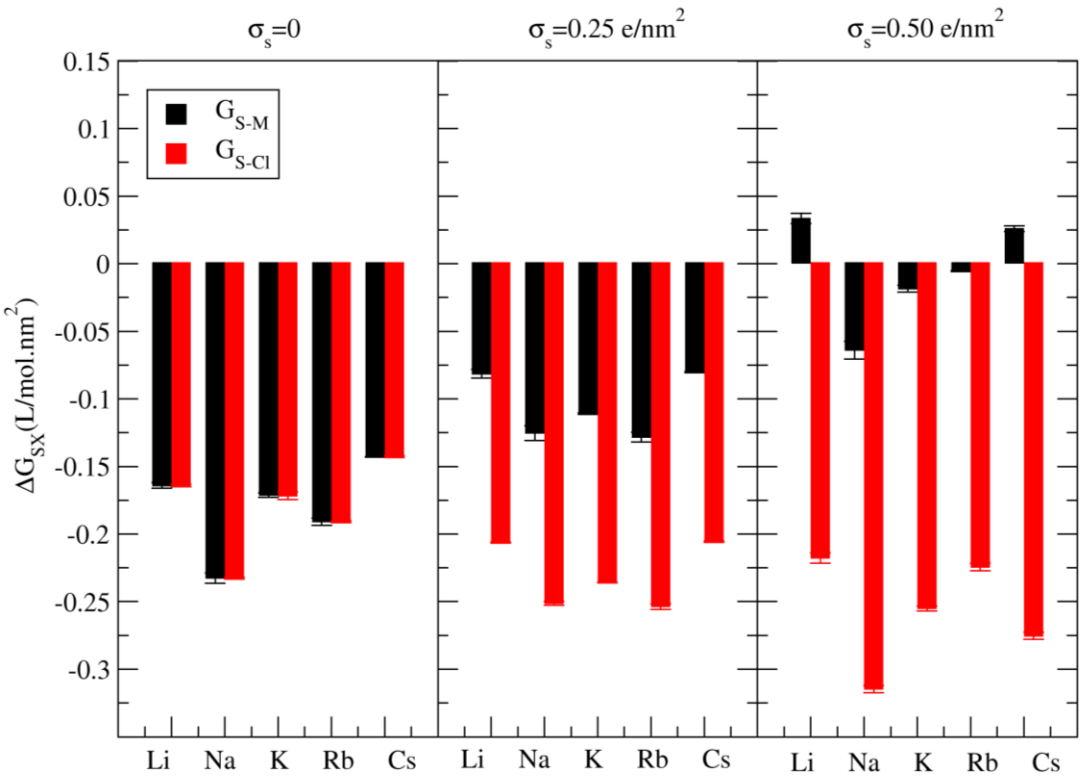

Figure 4.8. A bar graph showing the KBI values for metal and chlorides ions in 2M aqueous MCl (M = Li/ Na/ K/ Rb/Cs) solutions at uncharged and charged Au surfaces.

Figure 4.8 shows that in the absence of any charge, the KBI values of both M (G_{S-M}) and Cl (G_{S-Cl}) with respect to the Au surface are the same. In the presence of the negative medium charge density, the G_{S-M} KBI is less negative than the G_{S-Cl} as metal ions are required to neutralize the surface in the presence of the large negative charge density the G_{S-M} becomes even more positive, and the G_{S-Cl} becomes even more negative. Thus, as the surface charge starts to become negative there is the expected accumulation of metals and depletion of chlorides near the surface. However, the trends do not appear to be systematic. Here, sodium is the most excluded cation, while lithium appears to favor association with the surface. This does not follow the expected trends based on

desolvation penalties (see later discussion) which would suggest cesium should display the largest association.

Interesting results were obtained in the case of the mixed salt solutions. Here, we have chosen NaCl as the reference salt. This study helps to quantify the preferences displayed by the different ions in various electrolyte mixtures. The ion distributions and corresponding KBIs are displayed in Figures 4.9 to 4.12. As shown in Figure 4.8, the KBI values for all the components of the mixed salt were negative before any charge was applied. Upon application of the negative charge, the Cl ions were depleted from the Au surface, whereas more Li ions were present near the Au surface than Na ions in the LiCl/NaCl mixed electrolyte system. The RDFs also illustrate the same conclusion. This system displays a clear preference for Lithium over Sodium in neutralization of the surface charge. Comparison with the distributions from other salt mixtures indicates that Sodium is always the most excluded cation. Similar observations have appeared in previous simulation studies, although the exact reasons for this are not clear.[24,25]

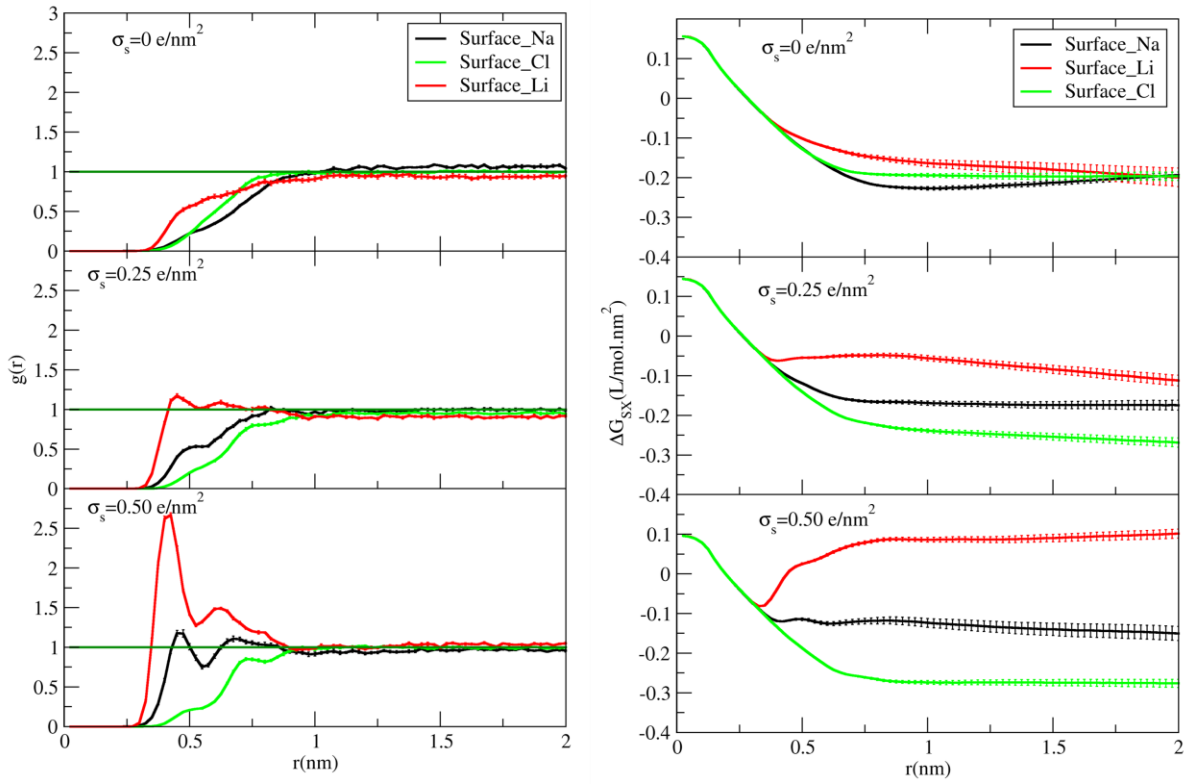

Figure 4.9. Distribution functions (left) and KBIs (right) for an aqueous mixture of 1M LiCl and 1M NaCl solution with respect to the Au surface at different charge densities.

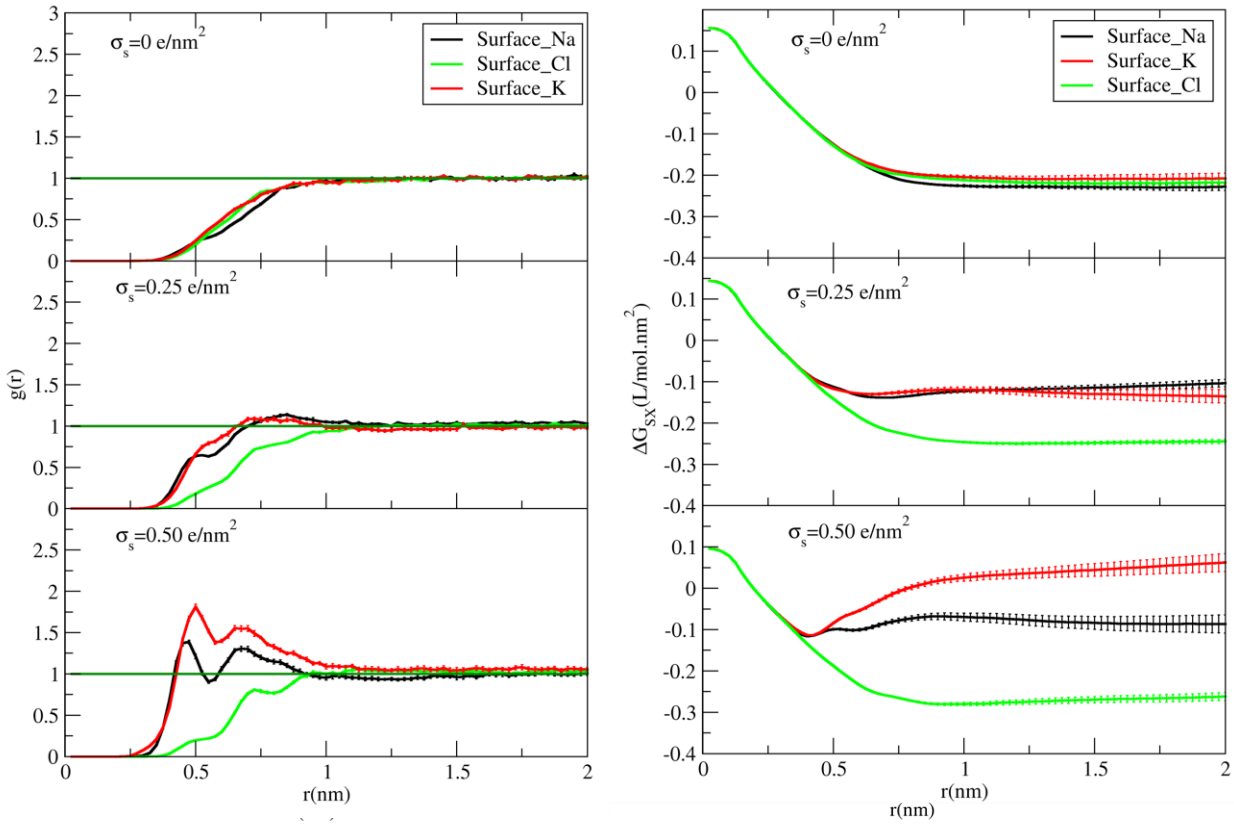

Figure 4.10. Distribution functions (left) and KBIs (right) for an aqueous mixture of 1M KCl and 1M NaCl solution with respect to the Au surface at different charge densities.

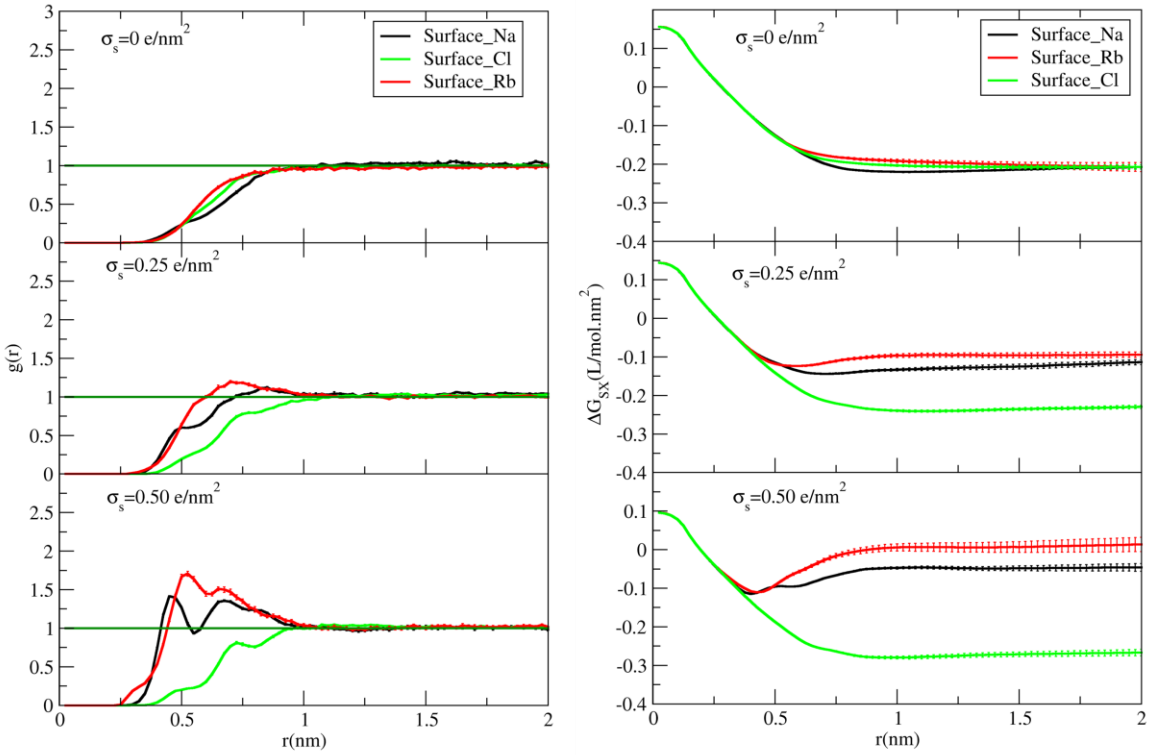

Figure 4.11. Distribution functions (left) and KBIs (right) for an aqueous mixture of 1M RbCl and 1M NaCl solution with respect to the Au surface at different charge densities.

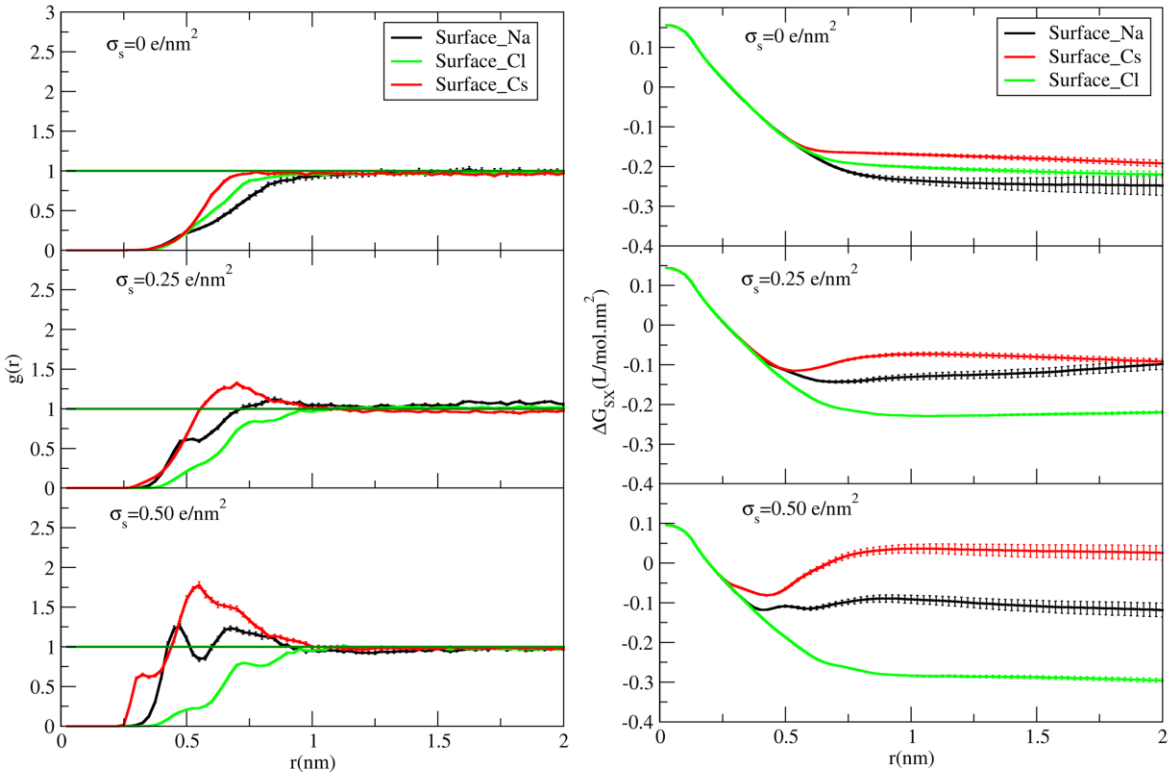

Figure 4.12. Distribution functions (left) and KBIs (right) for an aqueous mixture of 1M CsCl and 1M NaCl solution with respect to the Au surface at different charge densities.

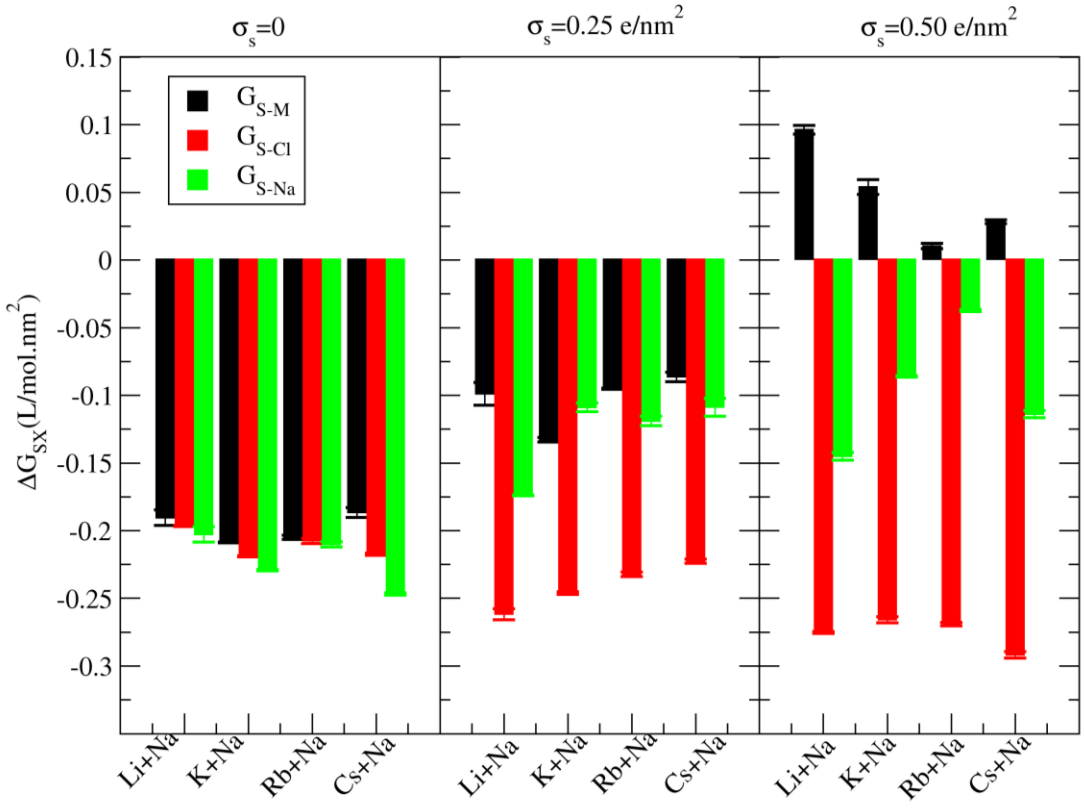

Figure 4.13. A bar graph showing KBI values of metal and chloride ions in a mixture of aqueous 1M NaCl + 1M M´Cl (M´ = Li/ K/ Rb/Cs) for uncharged and charged Au surfaces.

Figure 4.13 shows a similar picture to Figure 4.12 but for the mixture of salts. The behavior of the common chloride ions is the same as in Figure 4.12. Meanwhile, the two metals compete to get near the negatively charged surface. It appears that the addition of NaCl has increased the interaction of all the all cations with the surface. Hence, it seems clear that manipulation of the

relative bulk electrolyte concentrations could be used to manipulate the surface adsorption of different ions.

To investigate this effect further we have considered several properties of the salt solutions that might be involved. Besides the charge on the plate, two competing effects could contribute towards the depletion or accumulation of different cations near the negatively charged Au surface. The first is the strength of the water solvation shell surrounding the ions. The stronger the water molecules are held the less likely the cation is to interact, at least directly, with the charged surface. This would favor Cs association over Li. The second is ion pair formation in the solution. The more ion pairs a solution has the less free cations are available to neutralize the surface charge.

We performed simulations of the bulk (no surface) electrolytes and converted the cation to water distribution to a potential of mean force (PMF) via, $W(r) = - RT \ln g(r)$. As we know from the literature, negative PMF values indicate attraction between the components.[26,27] We also determined the degree of ion pairing in these solutions. The PMFs and ion pairing RDFs are displayed in Figure 4.14. There were no differences between the pure 2M and mixed 1M/1M results. The depth of the first minimum in the PMF and the number of ion pairs are displayed in Table 4.1.

2M salt	PMF first minima depth (kJ/mol)	Ion pairing
LiCl	-6.88	0.002
NaCl	-5.56	0.22
KCl	-4.55	0.38
RbCl	-3.51	0.47
CsCl	-3.44	0.63

Table 4.1. The PMF first minima depth and ion pairing in 2M salts in between Au plates

The values were plotted against the M-Cl coordination number in Figure 4.15. There is a strong (almost linear) inverse correlation between the binding free energy of the first shell waters and the degree of ion pairing in the solution.

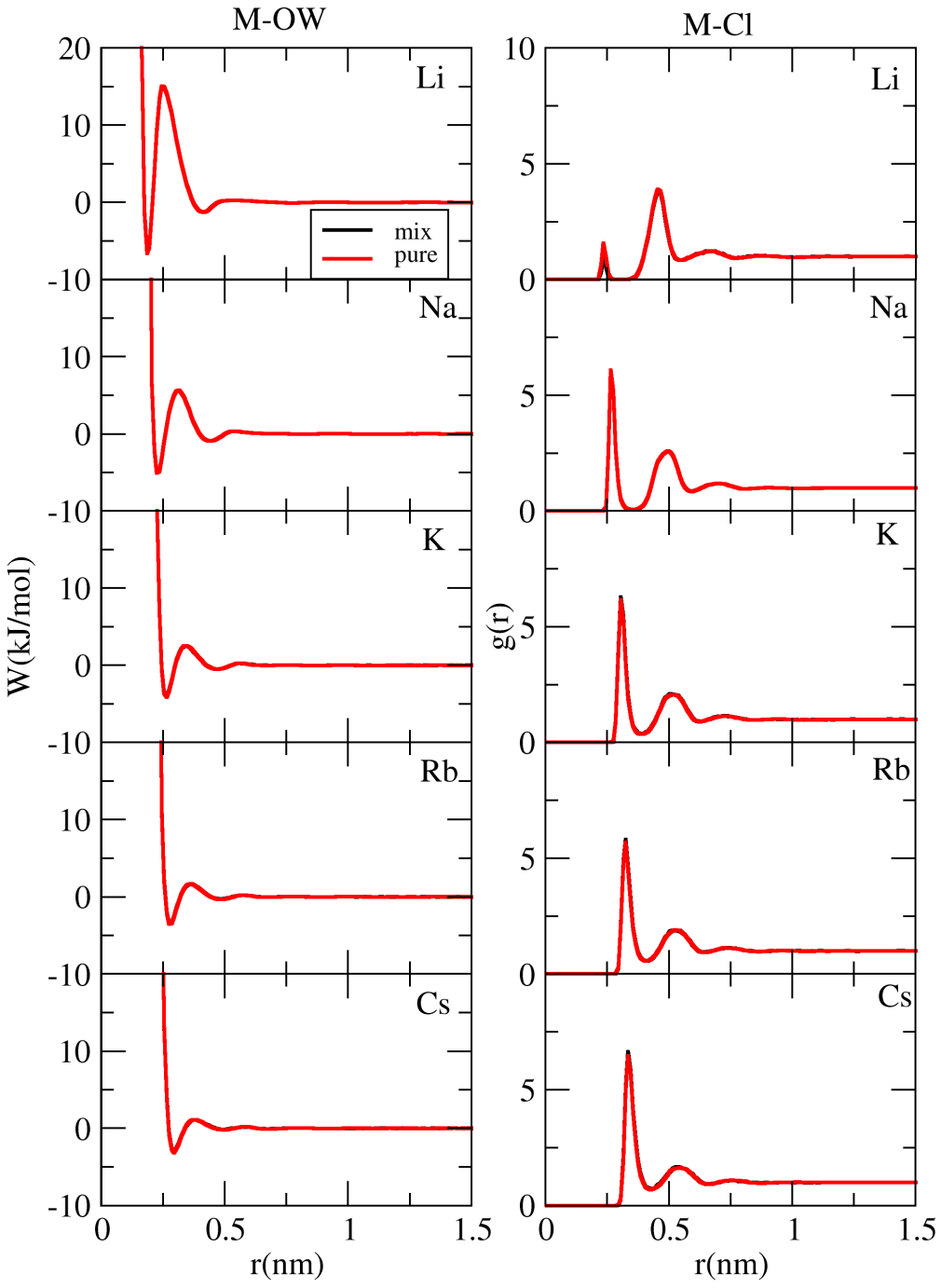

Figure 4.14. The PMFs between M-OW (left) and the RDFs between M-Cl (right) obtained from simulations of aqueous 2m and 1m+1m metal chloride solutions.

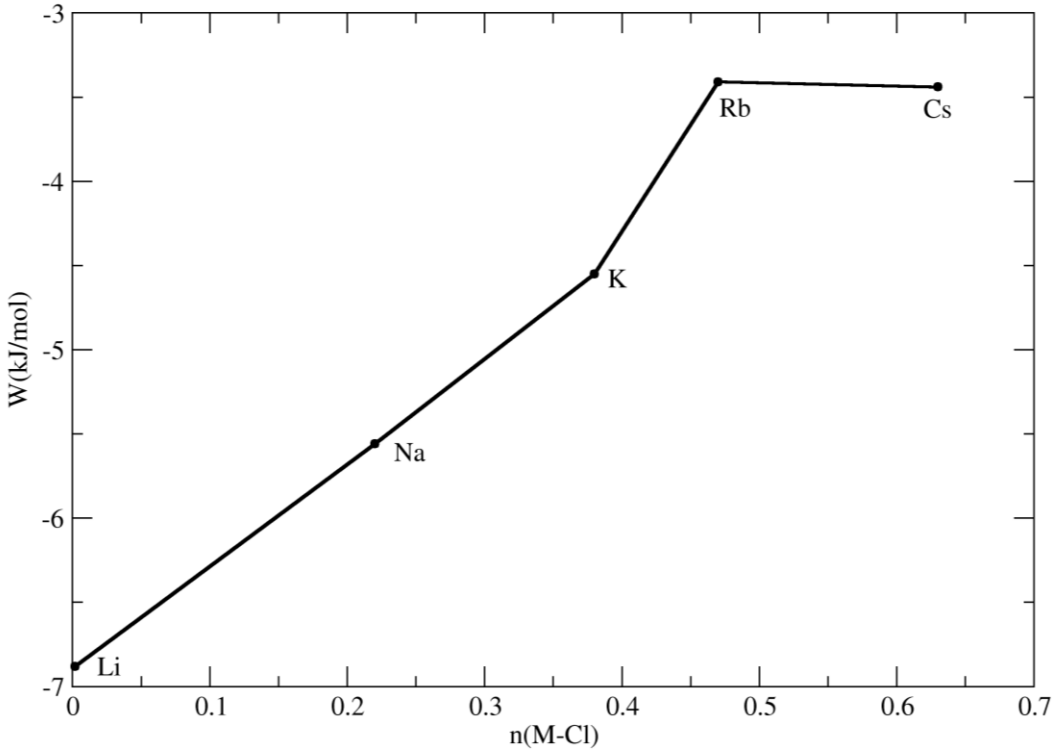

Figure 4.15. The M-OW first shell PMF energy (W) vs M-Cl coordination number (n) obtained from simulations of aqueous 2m metal chloride solutions.

4.4. A special case for a mixture of 1M LiCl + 1M NaCl aqueous solution

In Figure 4.15, we can see that the Li-Cl coordination number is close to zero. Based on this observation, it was possible to introduce a certain percentage of Li-Cl ion pairs in the aqueous mixture of 1M LiCl and 1M NaCl and study whether ion-pair formation or loss of solvation shell effect dominates the presence of metal ions near a charged Au surface. We introduced 25% and

50% Li-Cl ion pairs in the mix of 1M LiCl + 1M NaCl aqueous solution and repeated our simulations. The ion pairs were formed by applying a bond constraint between a certain number of Li^+ ions and Cl^- ions. The results of the simulations are given in Figure 4.16.

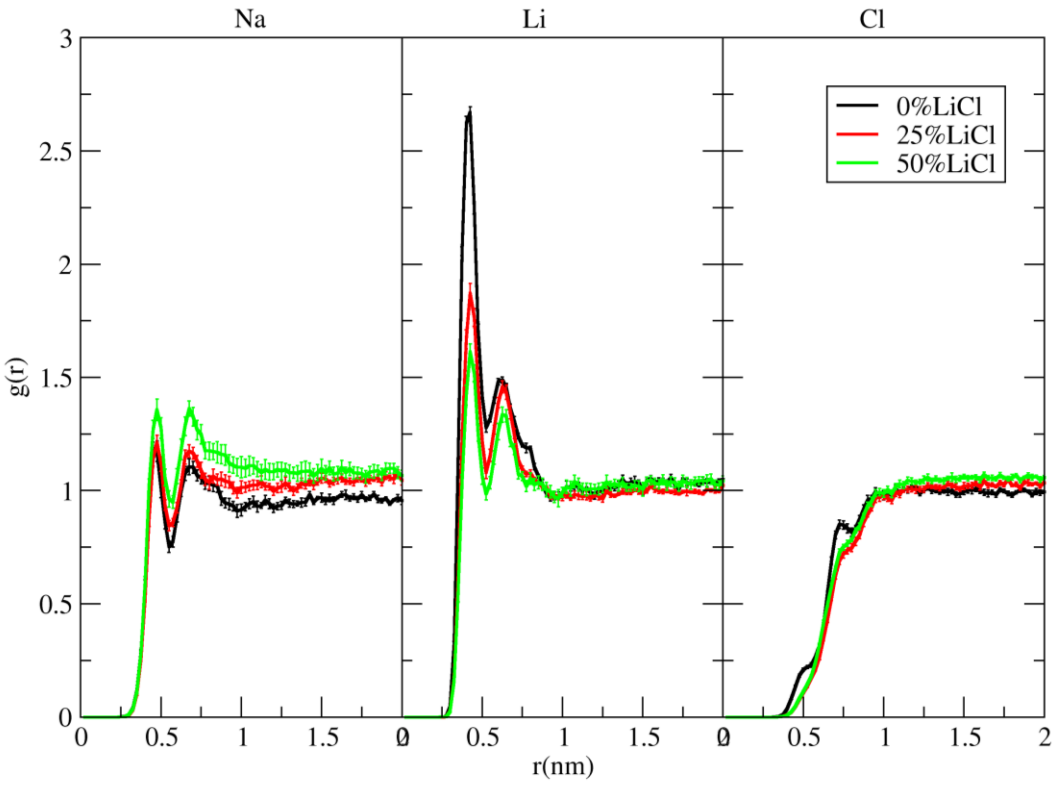

Figure 4.16. Surface-Na, Surface-Li, and Surface-Cl distribution functions for aqueous 1M NaCl + 1M LiCl solutions obtained after constraining 0%, 25%, and 50% of the Li-Cl ion pair at the highest charge density.

Figure 4.16 indicates only small differences in the S-Na and S-Cl RDFs in the presence of different percentages of Li-Cl ion pairs in the aqueous mixture. For the S-Li RDFs, the presence of Li-Cl ion pairs significantly decreases the peak heights, which means the attraction between the charged

Au plate and the Li ions decreases. Thus, between the two competing forces (loss of solvation shell and formation of an ion pair), the ion pair formation has a larger effect on the movement of metal ions toward the charged Au surface. When no Li-Cl ion pair is present in the system, more Li ions are present near the charged Au surface than Na ions, even though their desolvation free energy is greater.

4.5. Conclusions

We have simulated aqueous 2M pure salts and a 1M + 1M mix of salts near planar charged and uncharged Au surfaces. We calculated RDFs, KBIs, PMFs, and coordination numbers for each system. The simulations indicate that surface to cation distributions can be manipulated by varying the bulk electrolyte composition. Using the current model, Sodium ions were always the most excluded cation. In this study, we have taken a closer look at Li ions progressing toward Au electrodes in the presence and absence of an electric field. In an aqueous solution, the formation of ion pairs and loss of solvation shell waters are the two competing forces that govern the movement of Li ions toward the Au electrode. By varying the percentage of ion pairs in the solution, it was possible to study the two competing effects. Hence, Li prefers charged surface because it has a low tendency for ion pairing, and therefore a higher percentage of Li ions are available for charge neutralization. In this study we have assume that the salt force fields are realistic. The effect of the force field also needs to be considered. Different force field parameters might produce slightly different results.

4.5. References

(1) Xu, G.; Shangguan, X.; Dong, S.; Zhou, X.; Cui, G. Formulation of Blended-Lithium-Salt Electrolytes for Lithium Batteries. *Angewandte Chemie International Edition* **2020**, *59* (9), 3400–3415. https://doi.org/10.1002/anie.201906494.

(2) Chen, L.; Gu, Q.; Zhou, X.; Lee, S.; Xia, Y.; Liu, Z. New-Concept Batteries Based on Aqueous Li+/Na+ Mixed-Ion Electrolytes. *Sci Rep* **2013**, *3* (1), 1946. https://doi.org/10.1038/srep01946.

(3) Quesada-Pérez, M.; Martín-Molina, A.; Hidalgo-Álvarez, R. Simulation of Electric Double Layers Undergoing Charge Inversion: Mixtures of Mono- and Multivalent Ions. *Langmuir* **2005**, *21* (20), 9231–9237. https://doi.org/10.1021/la0505925.

(4) Taboada-Serrano, P.; Yiacoumi, S.; Tsouris, C. Behavior of Mixtures of Symmetric and Asymmetric Electrolytes near Discretely Charged Planar Surfaces: A Monte Carlo Study. *The Journal of Chemical Physics* **2005**, *123* (5), 054703. https://doi.org/10.1063/1.1992484.

(5) Taboada-Serrano, P.; Yiacoumi, S.; Tsouris, C. Electrostatic Surface Interactions in Mixtures of Symmetric and Asymmetric Electrolytes: A Monte Carlo Study. *The Journal of Chemical Physics* **2006**, *125* (5), 054716. https://doi.org/10.1063/1.2238869.

(6) Wang, K.; Yu, Y.-X.; Gao, G.-H.; Luo, G.-S. Preferential Interaction between DNA and Small Ions in Mixed-Size Counterion Systems: Monte Carlo Simulation and Density Functional Study. *The Journal of Chemical Physics* **2007**, *126* (13), 135102. https://doi.org/10.1063/1.2713105.

(7) Valiskó, M.; Boda, D.; Gillespie, D. Selective Adsorption of Ions with Different Diameter and Valence at Highly Charged Interfaces. *J. Phys. Chem. C* **2007**, *111* (43), 15575–15585. https://doi.org/10.1021/jp073703c.

(8) Biesheuvel, P. M.; van Soestbergen, M. Counterion Volume Effects in Mixed Electrical Double Layers. *Journal of Colloid and Interface Science* **2007**, *316* (2), 490–499. https://doi.org/10.1016/j.jcis.2007.08.006.

(9) Lima, E. R. A.; Boström, M.; Horinek, D.; Biscaia, E. C.; Kunz, W.; Tavares, F. W. Co-Ion and Ion Competition Effects: Ion Distributions Close to a Hydrophobic Solid Surface in Mixed Electrolyte Solutions. *Langmuir* **2008**, *24* (8), 3944–3948. https://doi.org/10.1021/la7037069.

(10) Vatamanu, J.; Borodin, O.; Smith, G. D. Molecular Dynamics Simulation Studies of the Structure of a Mixed Carbonate/LiPF6 Electrolyte near Graphite Surface as a Function of Electrode Potential. *J. Phys. Chem. C* **2012**, *116* (1), 1114–1121. https://doi.org/10.1021/jp2101539.

(11) Döpke, M. F.; Lützenkirchen, J.; Moultos, O. A.; Siboulet, B.; Dufrêche, J.-F.; Padding, J. T.; Hartkamp, R. Preferential Adsorption in Mixed Electrolytes Confined by Charged

Amorphous Silica. *J. Phys. Chem. C* **2019**, *123* (27), 16711–16720. https://doi.org/10.1021/acs.jpcc.9b02975.

(12) Wu, Q.; McDowell, M. T.; Qi, Y. Effect of the Electric Double Layer (EDL) in Multicomponent Electrolyte Reduction and Solid Electrolyte Interphase (SEI) Formation in Lithium Batteries. *J. Am. Chem. Soc.* **2023**, *145* (4), 2473–2484. https://doi.org/10.1021/jacs.2c11807.

(13) Fraenkel, D. Theoretical Analysis of Aqueous Solutions of Mixed Strong Electrolytes by a Smaller-Ion Shell Electrostatic Model. *The Journal of Chemical Physics* **2014**, *140* (5), 054513. https://doi.org/10.1063/1.4862689.

(14) Lamperski, S.; Outhwaite, C. W. Monte-Carlo Simulation of Mixed Electrolytes next to a Plane Charged Surface. *Journal of Colloid and Interface Science* **2008**, *328* (2), 458–462. https://doi.org/10.1016/j.jcis.2008.09.050.

(15) Schmickler, W.; Belletti, G.; Quaino, P. The Approach of Alkali Ions towards an Electrode Surface – A Molecular Dynamics Study. *Chemical Physics Letters* **2022**, *795*, 139518. https://doi.org/10.1016/j.cplett.2022.139518.

(16) Waegele, M. M.; Gunathunge, C. M.; Li, J.; Li, X. How Cations Affect the Electric Double Layer and the Rates and Selectivity of Electrocatalytic Processes. *The Journal of Chemical Physics* **2019**, *151* (16), 160902. https://doi.org/10.1063/1.5124878.

(17) Lindahl; Abraham; Hess; Spoel, V. D. GROMACS 2019.5 Source Code, 2019. https://doi.org/10.5281/ZENODO.3577986.

(18) Ploetz, E. A.; Karunaweera, S.; Smith, P. E. Kirkwood–Buff-Derived Force Field for Peptides and Proteins: Applications of KBFF20. *J. Chem. Theory Comput.* **2021**, *17* (5), 2991–3009. https://doi.org/10.1021/acs.jctc.1c00076.

(19) Girotto, M.; Alencar, A. M. Modified 3D Ewald Summation for Slab Geometry at Constant Potential. *J. Phys. Chem. B* **2020**, *124* (36), 7842–7848. https://doi.org/10.1021/acs.jpcb.0c03510.

(20) Nosé, S. A Unified Formulation of the Constant Temperature Molecular Dynamics Methods. *The Journal of Chemical Physics* **1984**, *81* (1), 511–519. https://doi.org/10.1063/1.447334.

(21) *Settle: An analytical version of the SHAKE and RATTLE algorithm for rigid water models - Miyamoto - 1992 - Journal of Computational Chemistry - Wiley Online Library*. https://onlinelibrary.wiley.com/doi/abs/10.1002/jcc.540130805 (accessed 2024-05-15).

(22) Darden, T.; York, D.; Pedersen, L. Particle Mesh Ewald: An N·log(N) Method for Ewald Sums in Large Systems. *The Journal of Chemical Physics* **1993**, *98* (12), 10089–10092. https://doi.org/10.1063/1.464397.

(23) Chen, F.; Smith, P. E. Simulated Surface Tensions of Common Water Models. *The Journal of Chemical Physics* **2007**, *126* (22), 221101. https://doi.org/10.1063/1.2745718.

(24) Chaban, V. V.; Andreeva, N. A. Aqueous Electrolytes at the Charged Graphene Surface: Electrode-Electrolyte Coupling. *Journal of Molecular Liquids* **2023**, *387*, 122724.

(25) Dočkal, J.; Lísal, M.; Moučka, F. Molecular Dynamics of Preferential Adsorption in Mixed Alkali–Halide Electrolytes at Graphene Electrodes. *The Journal of Chemical Physics* **2022**, *157* (8).

(26) Iskrenova-Tchoukova, E.; Kalinichev, A. G.; Kirkpatrick, R. J. Metal Cation Complexation with Natural Organic Matter in Aqueous Solutions: Molecular Dynamics Simulations and Potentials of Mean Force. *Langmuir* **2010**, *26* (20), 15909–15919. https://doi.org/10.1021/la102535n.

(27) Babu, C. S.; Lim, C. Empirical Force Fields for Biologically Active Divalent Metal Cations in Water. *J. Phys. Chem. A* **2006**, *110* (2), 691–699. https://doi.org/10.1021/jp054177x.

Chapter 5 - Computer simulation of ion distributions and properties of different seawaters

5.1. Introduction

Seawater is a dynamic chemical mixture that interacts constantly with the land, the atmosphere, and living organisms.[1] Seawater is an essential component in many chemical processes and is significant due to its rich composition and diverse array of dissolved substances. The complex mixture of salts, minerals, gases, and organic matter in seawater serves as a reservoir of elements crucial for various chemical processes and reactions. The composition of seawater also plays a crucial role in understanding oceanic ecosystems, climate dynamics, and even the origin of life. Seawater provides essential elements for biochemical reactions and serves as a medium for chemical transportation and transformation.[2–4] Due to its composition, seawater's properties vary from pure water. Its pH is slightly alkaline.[5] Compared to pure water, the seawater density, viscosity, surface tension, and boiling point are higher, and the freezing point is lower.[6] The complex nature of seawater makes its Chemistry complex. Millero has published an excellent review on the properties of seawater.[7]

Seawater plays a significant role in modern technology across various industries and applications. Desalination technologies, such as reverse osmosis and distillation, are used to extract freshwater from seawater, which helps to address water scarcity issues in arid regions and provides a vital resource for agriculture, industry, and municipal use.[8] Seawater is used as a coolant in thermal power plants and industrial processes.[9] Its abundance of dissolved minerals and salts makes it an

essential resource for extracting valuable resources such as magnesium, lithium, and bromine through processes such as evaporation ponds and electrolysis.[10–12] Seawater's unique chemical composition also supports innovative applications in materials science. For example, it is used to develop corrosion-resistant coatings and biomimetic structures inspired by marine organisms.[13]

Seawater is a complex solution of substances, primarily ions, in water.[14] To completely understand the physical chemistry of seawater on a molecular level, it is necessary to know and understand the physical chemistry and structure of electrolyte solutions. The calculations of activity coefficients using the Pitzer equations have been used for a long time to calculate properties of seawater, such as activity coefficients of the components, concentration of individual ions, pH, density, compressibility, heat capacity, enthalpy, etc.[15–27] However, molecular simulation studies regarding the properties of seawater are scarce in the literature. Zhang et al. performed the first study of the free energies of salts in water under pressure using classical molecular dynamics simulation.[28] Nayar et al. published a review on calculating the thermophysical properties of seawater and software implementation of the correlations developed in the paper.[29] Zeron et al. recently simulated the thermodynamic, dynamic, interfacial, and structural properties of seawater.[14] However, the accurate simulation of the properties of seawater is hindered by the quality of force fields available for the ionic components, together with the large system sizes required to simulate ions at relatively low concentrations with statistically meaningful accuracy.

Previously, Lund et al. used Monte Carlo simulations to calculate activity coefficients of different inorganic salts in seawater.[30] However, no study has been published that calculates the ion distributions in seawater. The inorganic ions Cl^-, Na^+, SO_4^{2-}, Mg^{2+}, Ca^{2+}, K^+, and Br^- comprise

99% of all sea salts by weight.[31] Thus, we focus on these seven ions. We simulate regular seawater, as well as Red Sea brine and Dead Sea brine, due to their unique and different nature than regular seawater. We use KB theory to calculate KBIs and compare the three sea waters.

5.2. Methods

5.2.1. System Setup

We used our custom-made FORTRAN code to generate a 15x15x15 nm^3 cubic simulation box filled with a random arrangement of a specific number of water molecules and ions. The number of ions to be filled in each system was determined using the concentrations of each component provided in the book "Activity Coefficients in Electrolyte Solutions" by Kenneth S. Pitzer.[32] Table 5.1 shows the number of ions and water molecules in the three systems that we simulated. The ionic strength of the three systems was calculated to be 0.7, 7.0, and 5.0 M for the seawater, Red Sea, and Dead Sea, respectively.

Species	# in Seawater (SW)	# in Red Sea (RSW)	# in Dead Sea (DSW)	ρ_{SW} (mol/L)	ρ_{RSW} (mol/L)	ρ_{DSW} (mol/L)
Na^+	968	10353	3364	0.5	5	1.6
Mg^{2+}	110	84	3016	0.05	0.04	1.5
Ca^{2+}	22	294	812	0.01	0.14	0.4
K^+	22	147	348	0.01	0.07	0.17
Cl^-	1122	11214	11252	0.55	5.5	5.5
SO_4^{2-}	66	21	-	0.32	0.01	-
Br^-	-	-	116	-	-	0.057
Water	111012	105966	106952	55	52	52

Table 5.1. Number and concentration of ions and water molecules in each system (seawater, Red Sea, and Dead Sea)

5.2.2. Molecular Dynamics Simulation Details

All the simulations were done using GROMACS 2019.5 software.[33] We used the KBFF20 force field to model our system.[34,35] The SO_4^{2-} ion parameters were taken from the previous work of our group member (Shin Suh, unpublished). The SPC/E water model was used.[36] The system was

maintained at isothermal isobaric condition (NPT ensemble). The temperature was maintained at 300 K using a Nosè-Hoover thermostat.[37] Parrinello-Rahman pressure coupling was used to keep the pressure at 1 bar.[38] All bonds were constrained using the SETTLE algorithm.[39] A 2 fs time step was used to integrate the equations of motion. The particle mesh Ewald (PME) was used to model electrostatic interactions with a 1 nm cut-off distance for real space calculation and a 1 nm cut-off distance for the van der Waals interactions.[40] The steepest descent method was used for three (1000-step each) energy minimization processes, followed by 1 ns equilibration. All the production runs were 2 μs long. After analysis of the production run, the first 500 ns were further discarded as part of the equilibration process, and the rest of the 1500 ns were divided into chunks of 500 ns to perform analysis. In the production run, configurations were saved every 100 ps. A separate 100 ns simulation with the implicit solvent model was performed, keeping all other conditions the same, to determine the necessity of simulations with the explicit solvent model. In the implicit solvent model, all the solvent molecules are replaced by a dielectric constant ($\varepsilon = 80$) scaling of all electrostatic interactions, making the simulations faster and computationally less expensive, but more approximate. For the analysis process, a custom-written Fortran code was used to calculate a center of mass RDF, which was then integrated to obtain KBIs (G_{ij}).

5.3. Results and Discussion

Figure 5.1 shows the cation-anion RDFs for simulation using the implicit and explicit solvent models. The corresponding cation-cation and anion-anion RDFs are provided in the Appendix. The final ion-ion distributions are clearly different with the implicit solvent approach providing distributions which lack much of the structure indicated by the presence of explicit solvent molecules. Most noticeable are the differences for divalent cations and anions. Here, the explicit

solvent simulations do not show any contact ion pair formation, unlike the implicit solvent simulations, but rather a strong solvent separated ion pair peak. Such features are the reason we prefer to study solutes in explicit solvents.

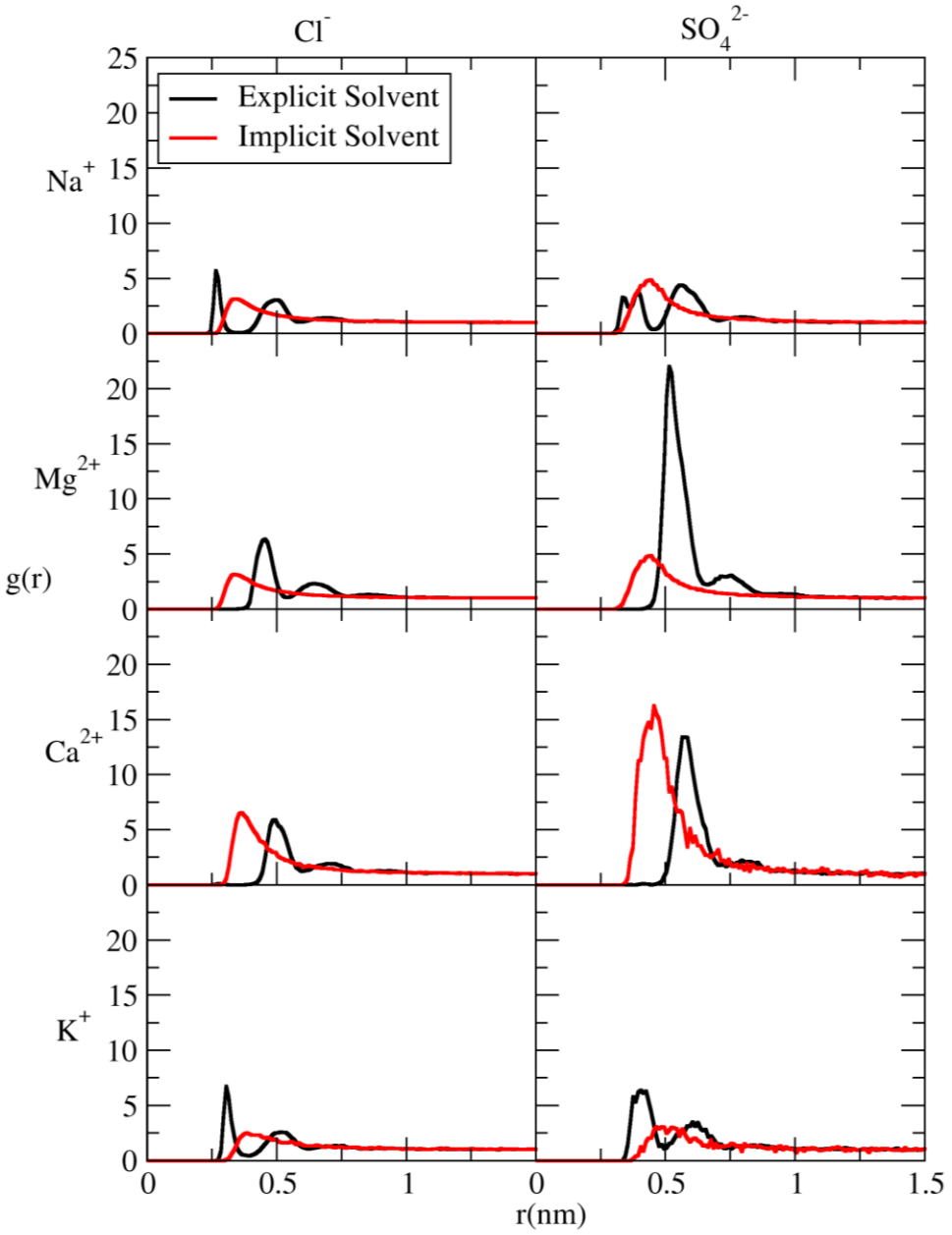

Figure 5.1. The cation-anion RDFs obtained from simulations of seawater using the implicit and explicit solvent models.

The results of these simulations are dependent on the quality of the force field used. Our group has performed simulations of all the possible combinations of salts in the three seawaters in isolation except for $MgSO_4$.[41,42] To test whether the current FF correctly reproduced the interactions between the ions in the three systems, we compared the ion-ion RDFs of the three seawater systems with the RDFs from our group's previous work.

In this work, we performed 100 simulations of aqueous 1m and 2m $MgSO_4$ solutions, using the same conditions as described in the Methods Section, and extracted the corresponding KBIs. To compare with the experimental KBIs we performed the KB inversion, as illustrated in Chapter 2, using the experimental activity coefficients taken from Robinson & Stokes.[43] The experimental density data were unavailable, so we used the pure crystal density of $MgSO_4$.[44] The results are shown in Figures 5.2 and 5.3.

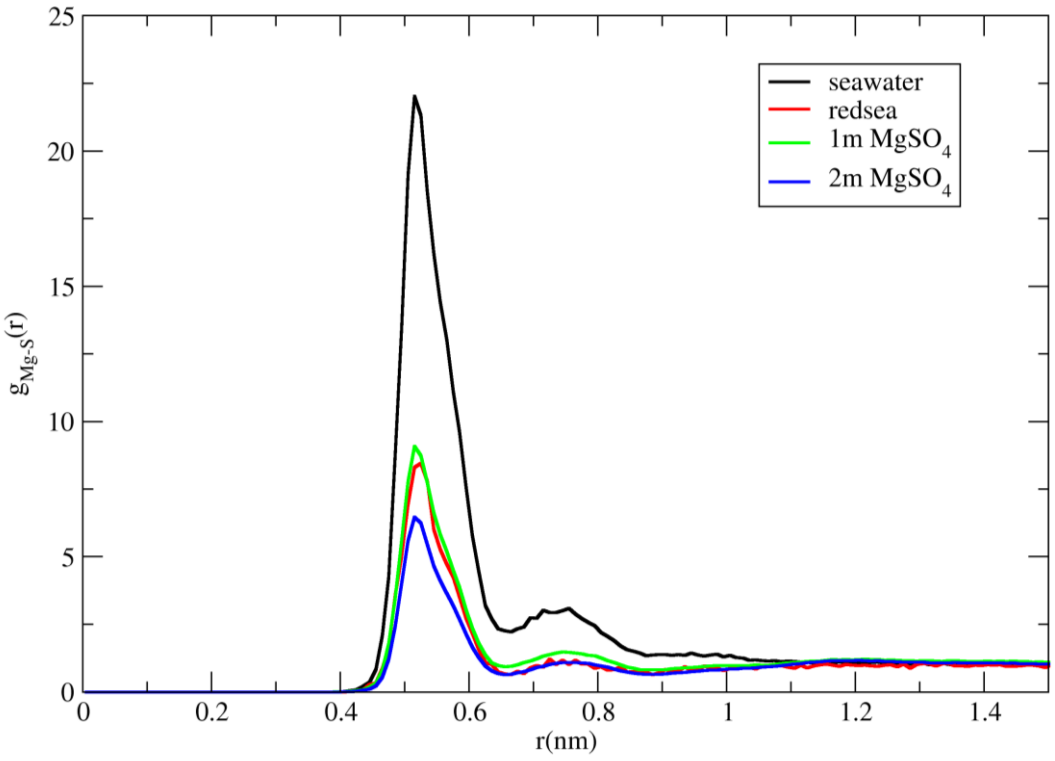

Figure 5.2. The RDFs between Mg and the sulfate sulfur (S) obtained from simulations of seawater, Red Sea water, and 1m and 2m aqueous $MgSO_4$ solutions.

Figure 5.2 compares the RDFs of seawater and the Red Sea system with 1m and 2m aqueous $MgSO_4$ solutions. The differences in peak heights are due to the different concentrations of the simulated systems. The RDFS from the 1m and 2m $MgSO_4$ systems were then integrated to give the corresponding KBIs. The results are shown in Figure 5.3. The figure shows reasonable agreement between the simulated and experimental KBIs for aqueous $MgSO_4$. In conclusion, we have significant confidence that the models reproduce the properties of the various salts composing seawater when studied in isolation. As these models were all developed in the same manner we have some confidence that our simulations of a complex mixture of the salts will also be accurate.

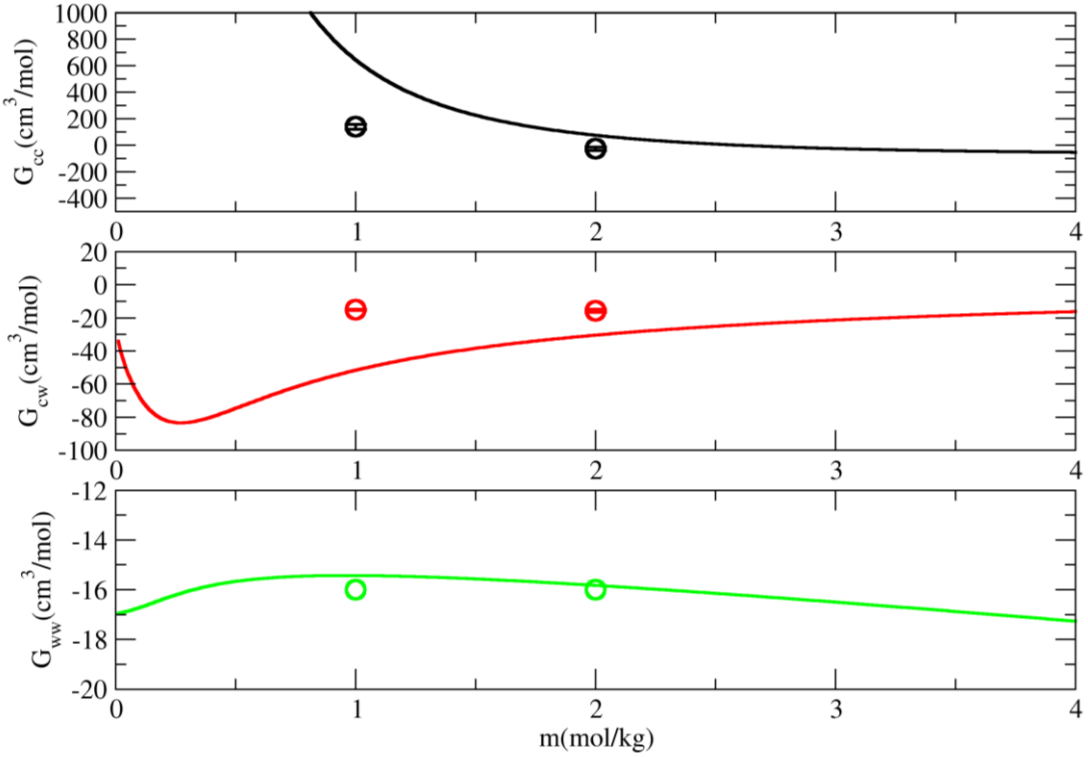

Figure 5.3. The simulated (symbols) and experimental (lines) KBIs of aqueous $MgSO_4$ solutions as a function of concentrations.

The cation-anion RDFs of all three systems are shown in Figure 5.4. The corresponding KBIs for the cation-anion, cation-cation and anion-anion distributions from all three systems are provided in the Appendix. The RDF shapes and positions match the results of the literature well.[41,42] The difference between the heights of the peaks occurs due to differences in the concentration of ions in the three systems.

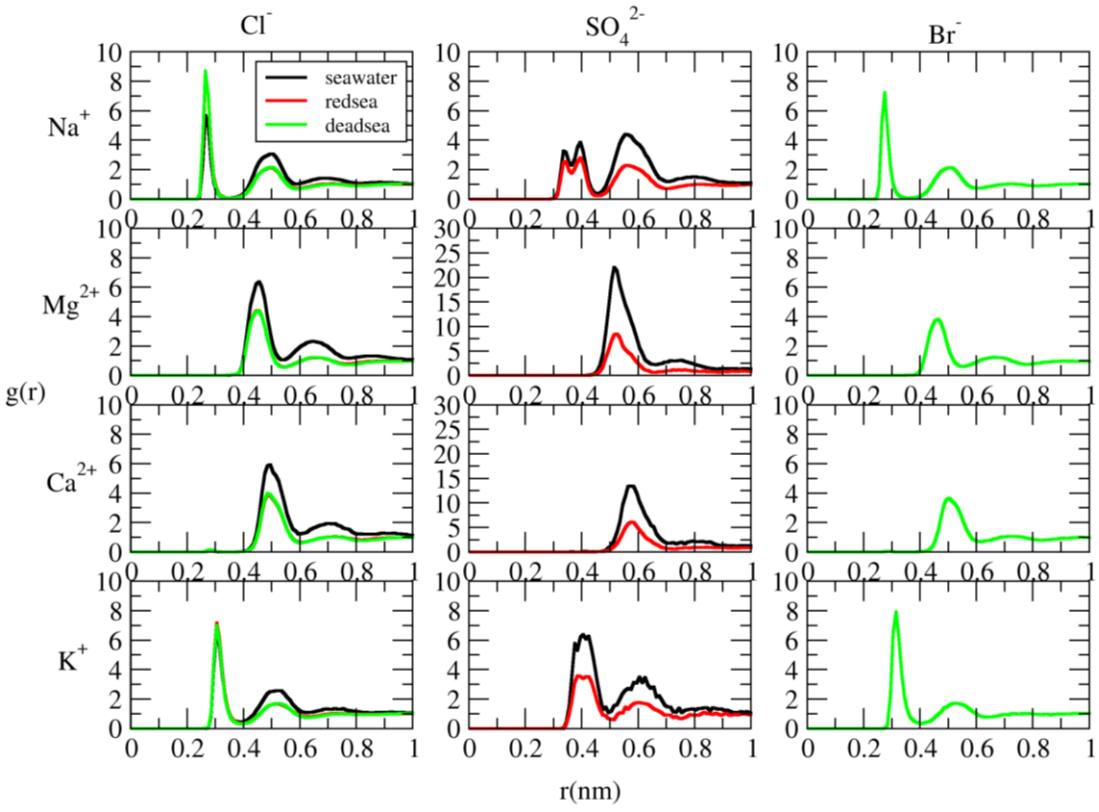

Figure 5.4. The cation-anion RDFs from simulations of seawater, Red Sea water, and Dead Sea water solutions.

The RDFs were integrated to obtain G^{total} (cm^3/mol) according to the usual expression,

$$G_{ij} = 4\pi \int_0^{\infty} [g_{ij}(r) - 1]\ r^2 dr \qquad (5.1)$$

where g_{ij} is the radial distribution function (RDF) between two species, *i* and *j*, in the system. Chapter 1 describes more details about KB theory. The results are shown in Figure 5.5. It is clear that the KBIs from the seawater simulation are significantly larger in magnitude than those from the Red Sea and Dead Sea simulations. However, much of this is due to the lower ionic strength of the seawater simulations as we now indicate.

In a separate ongoing project (Ploetz, Smyers and Smith, submitted), our group has observed that the ion-ion KBIs can be decomposed into two contributions: one contribution due to charge neutralization (G_{ij}^{CN}) and the other a thermodynamic contribution (G_{ij}^{TH}). Furthermore, the charge neutralization is simply related to the total ionic strength of the solution. The relevant equations are,

$$\begin{aligned} G_{ij} &= G_{ij}^{CN} + G_{ij}^{TH} \\ G_{ij}^{CN} &= -\frac{q_i q_j}{2I} \\ I &= \frac{1}{2}\sum \rho_i q_i^{\,2} \end{aligned} \tag{5.2}$$

where I is the total molar ionic strength of the solution, ρ_i is the number density, and q_i is the charge on ion i. It was also concluded that the charge neutralization played no role in the solution thermodynamics as provided by KB theory.

In the current simulations the total KBI values are dominated by the charge neutralization term, especially for the seawater system. In Figure 5.6 we present the thermodynamic contributions to the KBIs obtained after subtracting G^{CN} from the total KBIs. This produces more similar results for comparison. The exceptions are the divalent cation and anion combinations. Here, the KBIs remain much larger for the seawater system. This suggest a prominent role for these interactions in determining the thermodynamics of the solutions.

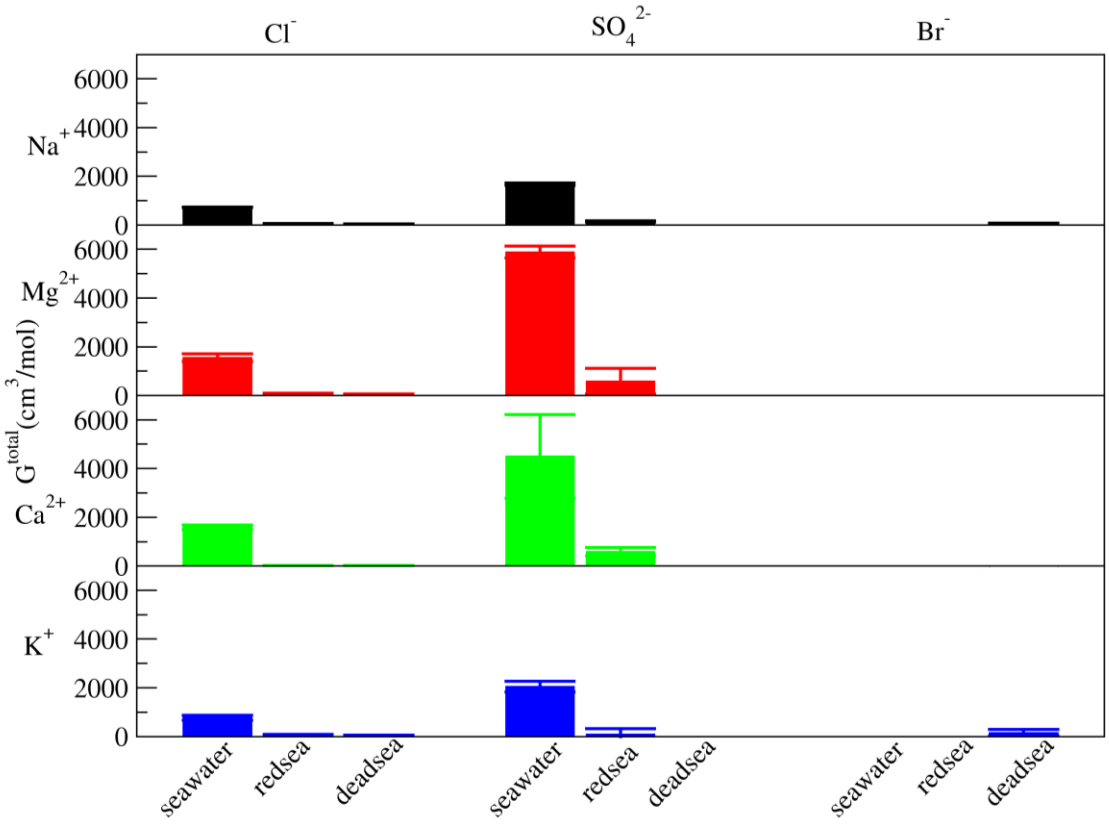

Figure 5.5. Comparison of the cation-anion KBIs obtained from simulations of seawater, Red Sea water, and Dead Sea water systems.

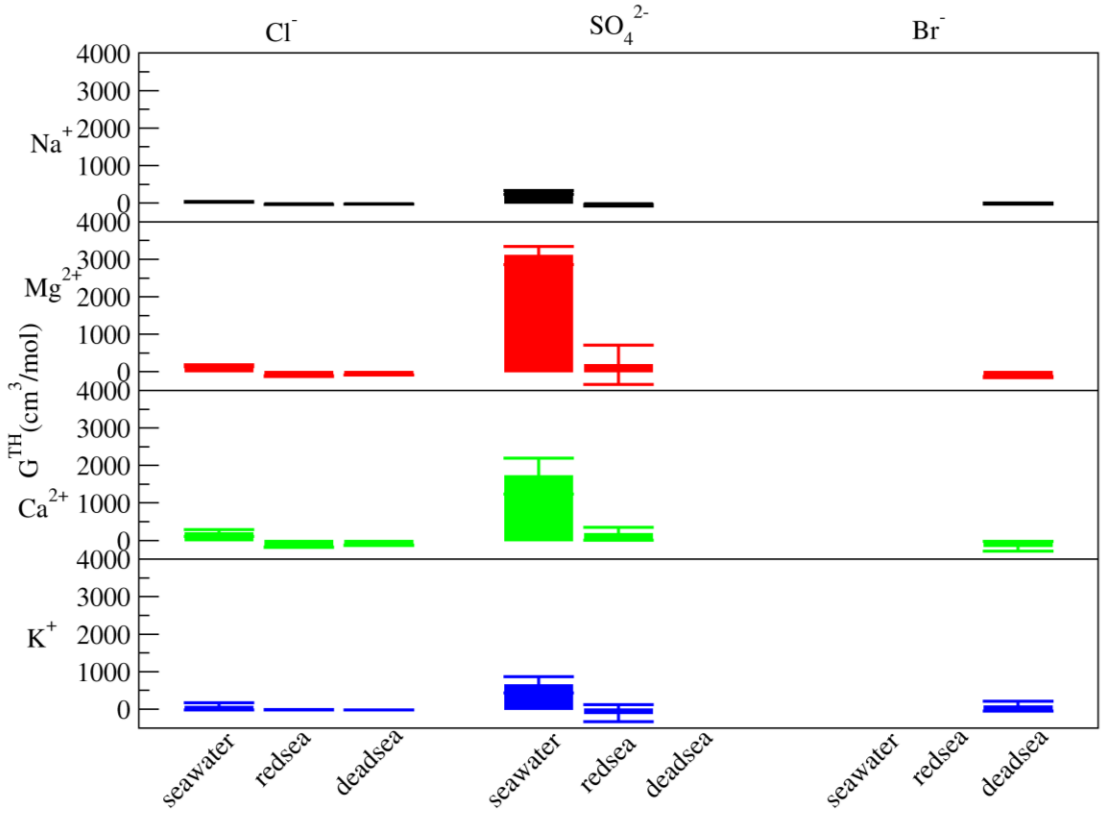

Figure 5.6. Comparison of the thermodynamic contribution to the cation-anion KBIs (G^{TH}) obtained from simulations of seawater, Red Sea water, and Dead Sea water systems.

The change in ion-ion G^{TH} values with the total ionic strength (*I*) of the three systems is shown in Figure 5.7. Figure 5.7 shows that the specific KBIs that dominate the thermodynamic contribution G^{TH} at lower ionic strengths. Larger thermodynamic contributions to the KBIs are evident in the case of double-charged ion combinations, such as Mg^{2+}-SO4^{2-} and Ca^{2+}-SO_4^{2-}. This result matches the data shown in the bar graphs in Figure 5.5, and Figure 5.6. The change with ionic strength

probably suggests that at higher total ion concentrations the competition from monovalent ions comes into play.

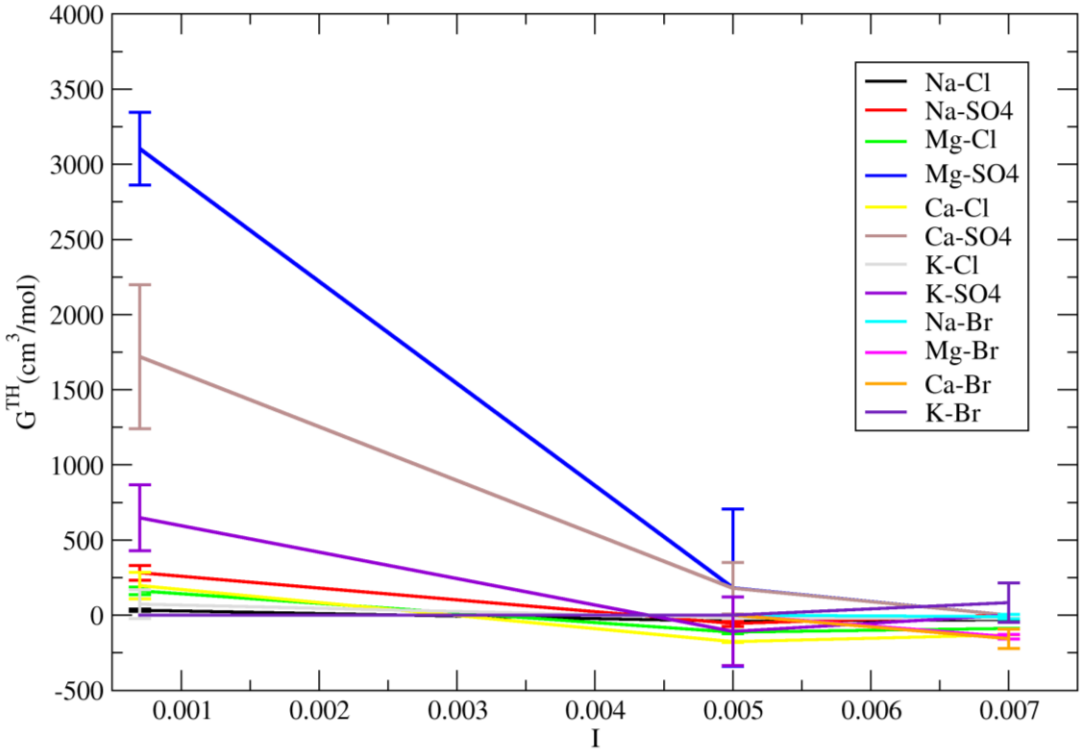

Figure 5.7. Changes in the thermodynamic contribution to the cation-anion KBIs (G^{TH}) with ionic strength (mol/cm^3) obtained from simulations of different sea waters.

5.4. Conclusions

In this chapter, we have simulated a set of three saltwater systems. These simulations are computationally intensive due to the low concentrations, and therefore large system sizes, required for many of the ions. We have compared and contrasted three types of seawater: regular seawater,

Red Sea water, and Dead Sea water, from the KB theory point of view. We have also split the total KBI (G^{total}) values into charge neutralization (G^{CN}) and thermodynamic contributions (G^{TH}), which is an entirely new approach. Significant differences were found between the three systems, especially between divalent anions and cations. Further work is required to fully understand the meaning of these findings.

5.5. References

(1) *The Salty Sea | manoa.hawaii.edu/ExploringOurFluidEarth*. https://manoa.hawaii.edu/exploringourfluidearth/chemical/chemistry-and-seawater/salty-sea (accessed 2024-04-01).

(2) De Mora, S. J. Chemistry of the Oceans. In *Principles of Environmental Chemistry*; Royal Society of Chemistry, 2007; pp 170–233.

(3) Kaim, W.; Schwederski, B.; Klein, A. *Bioinorganic Chemistry--Inorganic Elements in the Chemistry of Life: An Introduction and Guide*; John Wiley & Sons, 2013.

(4) Morel, F.; Milligan, A.; Saito, M. Marine Bioinorganic Chemistry: The. *The oceans and marine geochemistry* **2006**, *6*, 113.

(5) Halevy, I.; Bachan, A. The Geologic History of Seawater pH. *Science* **2017**, *355* (6329), 1069–1071.

(6) Brown, W. S. Physical Properties of Seawater. *Springer handbook of ocean engineering* **2016**, 101–110.

(7) Millero, F. J. The Physical Chemistry of Seawater. *Annual Review of Earth and Planetary Sciences* **1974**, *2* (1), 101–150.

(8) Peñate, B.; García-Rodríguez, L. Current Trends and Future Prospects in the Design of Seawater Reverse Osmosis Desalination Technology. *Desalination* **2012**, *284*, 1–8.

(9) Ibrahim, S. M.; Attia, S. I. The Influence of the Condenser Cooling Seawater Salinity Changes on the Thermal Performance of a Nuclear Power Plant. *Progress in Nuclear Energy* **2015**, *79*, 115–126.

(10) Yang, S.; Zhang, F.; Ding, H.; He, P.; Zhou, H. Lithium Metal Extraction from Seawater. *Joule* **2018**, *2* (9), 1648–1651.

(11) Enami, S.; Vecitis, C.; Cheng, J.; Hoffmann, M.; Colussi, A. Global Inorganic Source of Atmospheric Bromine. *The Journal of Physical Chemistry A* **2007**, *111* (36), 8749–8752.

(12) Quist-Jensen, C. A.; Koustrup Jørgensen, M.; Christensen, M. L. Treated Seawater as a Magnesium Source for Phosphorous Recovery from Wastewater—a Feasibility and Cost Analysis. *Membranes* **2016**, *6* (4), 54.

(13) Hassan, A. M.; Malik, A. Corrosion Resistant Materials for Seawater RO Plants. *Desalination* **1989**, *74*, 157–170.

(14) Zeron, I. M.; Gonzalez, M. A.; Errani, E.; Vega, C.; Abascal, J. L. F. “In Silico” Seawater. *J. Chem. Theory Comput.* **2021**, *17* (3), 1715–1725. https://doi.org/10.1021/acs.jctc.1c00072.

(15) Millero, F. J. The Estimation of the $pK*HA$ of Acids in Seawater Using the Pitzer Equations. *Geochimica et Cosmochimica Acta* **1983**, *47* (12), 2121–2129. https://doi.org/10.1016/0016-7037(83)90037-6.

(16) Millero, F. J.; Pierrot, D. The Apparent Molal Heat Capacity, Enthalpy, and Free Energy of Seawater Fit to the Pitzer Equations. *Marine chemistry* **2005**, *94* (1–4), 81–99.

(17) Pierrot, D.; Millero, F. J. The Apparent Molal Volume and Compressibility of Seawater Fit to the Pitzer Equations. *Journal of solution chemistry* **2000**, *29* (8), 719–742.

(18) Marion, G. M.; Millero, F. J.; Camões, M. F.; Spitzer, P.; Feistel, R.; Chen, C.-T. pH of Seawater. *Marine Chemistry* **2011**, *126* (1–4), 89–96.

(19) Rodriguez, C.; Millero, F. J. Estimating the Density and Compressibility of Seawater to High Temperatures Using the Pitzer Equations. *Aquatic geochemistry* **2013**, *19* (2), 115–133.

(20) Anes, B.; Bettencourt da Silva, R. J.; Martins, H. F.; Oliveira, C. S.; Camoes, M. F. Compatibility of Activity Coefficients Estimated Experimentally and by Pitzer Equations for the Assessment of Seawater pH. *Accreditation and Quality Assurance* **2016**, *21*, 1–7.

(21) Humphreys, M. P.; Waters, J. F.; Turner, D. R.; Dickson, A. G.; Clegg, S. L. Chemical Speciation Models Based upon the Pitzer Activity Coefficient Equations, Including the

Propagation of Uncertainties: Artificial Seawater from 0 to 45° C. *Marine Chemistry* **2022**, *244*, 104095.

(22) Feistel, R.; Marion, G. M. A Gibbs–Pitzer Function for High-Salinity Seawater Thermodynamics. *Progress in Oceanography* **2007**, *74* (4), 515–539.

(23) Keller, A.; Burger, J.; Hasse, H.; Kohns, M. Application of the Pitzer Model for Describing the Evaporation of Seawater. *Desalination* **2021**, *503*, 114866.

(24) Waters, J. F.; Millero, F. J. The Free Proton Concentration Scale for Seawater pH. *Marine Chemistry* **2013**, *149*, 8–22.

(25) Turner, D. R.; Achterberg, E. P.; Chen, C.-T. A.; Clegg, S. L.; Hatje, V.; Maldonado, M. T.; Sander, S. G.; Van den Berg, C. M.; Wells, M. Toward a Quality-Controlled and Accessible Pitzer Model for Seawater and Related Systems. *Frontiers in Marine Science* **2016**, *3*, 139.

(26) Nir, O.; Marvin, E.; Lahav, O. Accurate and Self-Consistent Procedure for Determining pH in Seawater Desalination Brines and Its Manifestation in Reverse Osmosis Modeling. *Water research* **2014**, *64*, 187–195.

(27) Qian, H.; Wu, F.; Zhang, F.; Zhou, Z.; Zhang, Z. An Accurate Calculation Model for Na+ Concentration in Seawater Desalination Solution. *Desalination* **2013**, *313*, 12–17.

(28) Zhang, C.; Giberti, F.; Sevgen, E.; de Pablo, J. J.; Gygi, F.; Galli, G. Dissociation of Salts in Water under Pressure. *Nat Commun* **2020**, *11* (1), 3037. https://doi.org/10.1038/s41467-020-16704-9.

(29) Nayar, K. G.; Sharqawy, M. H.; Banchik, L. D.; Lienhard V, J. H. Thermophysical Properties of Seawater: A Review and New Correlations That Include Pressure Dependence. *Desalination* **2016**, *390*, 1–24. https://doi.org/10.1016/j.desal.2016.02.024.

(30) Lund, M.; Jönsson, B.; Pedersen, T. Activity Coefficients in Sea Water Using Monte Carlo Simulations. *Marine Chemistry* **2003**, *80* (2), 95–101. https://doi.org/10.1016/S0304-4203(02)00039-7.

(31) *Seawater | Composition, Properties, Distribution, & Facts | Britannica*. https://www.britannica.com/science/seawater (accessed 2024-04-01).

(32) Pitzer, K. S.; Press, C. *Activity Coefficients in Electrolyte Solutions*; CRC press Boca Raton, FL, 1991; Vol. 2.

(33) *Welcome to the GROMACS documentation! — GROMACS documentation*. https://manual.gromacs.org/ (accessed 2024-02-17).

(34) Ploetz, E. A.; Karunaweera, S.; Smith, P. E. Kirkwood–Buff-Derived Force Field for Peptides and Proteins: Applications of KBFF20. *J. Chem. Theory Comput.* **2021**, *17* (5), 2991–3009. https://doi.org/10.1021/acs.jctc.1c00076.

(35) Ploetz, E. A.; Karunaweera, S.; Bentenitis, N.; Chen, F.; Dai, S.; Gee, M. B.; Jiao, Y.; Kang, M.; Kariyawasam, N. L.; Naleem, N.; Weerasinghe, S.; Smith, P. E. Kirkwood–Buff-Derived Force Field for Peptides and Proteins: Philosophy and Development of KBFF20. *J. Chem. Theory Comput.* **2021**, *17* (5), 2964–2990. https://doi.org/10.1021/acs.jctc.1c00075.

(36) Berendsen, H. J. C.; Grigera, J. R.; Straatsma, T. P. The Missing Term in Effective Pair Potentials. *J. Phys. Chem.* **1987**, *91* (24), 6269–6271. https://doi.org/10.1021/j100308a038.

(37) Nosé, S. A Unified Formulation of the Constant Temperature Molecular Dynamics Methods. *The Journal of Chemical Physics* **1984**, *81* (1), 511–519. https://doi.org/10.1063/1.447334.

(38) Parrinello, M.; Rahman, A. Polymorphic Transitions in Single Crystals: A New Molecular Dynamics Method. *Journal of Applied Physics* **1981**, *52* (12), 7182–7190. https://doi.org/10.1063/1.328693.

(39) *Settle: An analytical version of the SHAKE and RATTLE algorithm for rigid water models - Miyamoto - 1992 - Journal of Computational Chemistry - Wiley Online Library*. https://onlinelibrary.wiley.com/doi/abs/10.1002/jcc.540130805 (accessed 2024-05-15).

(40) Darden, T.; York, D.; Pedersen, L. Particle Mesh Ewald: An N·log(N) Method for Ewald Sums in Large Systems. *The Journal of Chemical Physics* **1993**, *98* (12), 10089–10092. https://doi.org/10.1063/1.464397.

(41) Gee, M. B.; Cox, N. R.; Jiao, Y.; Bentenitis, N.; Weerasinghe, S.; Smith, P. E. A Kirkwood-Buff Derived Force Field for Aqueous Alkali Halides. *J. Chem. Theory Comput.* **2011**, *7* (5), 1369–1380. https://doi.org/10.1021/ct100517z.

(42) Naleem, N.; Bentenitis, N.; Smith, P. E. A Kirkwood-Buff Derived Force Field for Alkaline Earth Halide Salts. *The Journal of Chemical Physics* **2018**, *148* (22), 222828. https://doi.org/10.1063/1.5019454.

(43) Robinson, R. A.; Stokes, R. H. *Electrolyte Solutions*; Courier Corporation, 2002.

(44) PubChem. *Magnesium Sulfate*. https://pubchem.ncbi.nlm.nih.gov/compound/24083 (accessed 2024-05-06).

Chapter 6 - Conclusions and Future Directions

This thesis was split into two parts. The first part (Chapters 2 and 3) focuses on simulating and developing a force field for simple ionic solutions, particularly alkali metal nitrate and alkaline earth nitrate aqueous solutions. Validation against experimental data showed good agreement. In the second part, more complex systems were explored, including simulations of alkali chloride aqueous solutions between charged or uncharged Au layers (Chapter 4) and three types of seawater (Chapter 5). Distinct preferences of different alkali metal ions towards charged Au plates was observed. A novel approach of splitting Kirkwood-Buff Integrals in charge neutralization and thermodynamic terms was introduced for the seawater analysis.

The biggest challenge with FF development is its transferability to other systems. The nitrate ion FF can be tested for compatibility with biomolecular systems as it is involved in the synthesis of protein, DNA, and RNA. Nitrate ions have massive applicability in agriculture, industry, environmental management, energy storage, medicine, and other scientific research areas. Testing our FF with those systems is the ultimate goal. One simple idea is to study a series of protein crystals that are known to contain the nitrate anion from crystallography to see if simulations with our FFs maintains the integrity of the nitrate binding.

The alkali halide simulations between the Au plates are preliminary studies that can be further extended to other complex systems, such as different electrolytes and/or more complicated (larger) ions. Instead of the Au plate, different kinds of surfaces, such as carbon nanostructures, other metal surfaces, and biological compounds, can be simulated. The metallic and carbonaceous substances

have applicability in electrochemical systems like batteries, fuel cells etc. The preference of electrolytes towards the plates/electrode surfaces is an active area of research. In biological systems, ion transport can be simulated, and preferential binding of the ions with the protein surfaces can be studied.

The seawater simulations were complex due to the presence of multiple ions and their low concentrations. Our models appear to reproduce the chemical properties of seawater, although a deeper comparison is still required to confirm this as fact. The same approaches can be applied to other complex aqueous electrolytic systems, both natural and manmade. The effects of different conditions, such as temperature, pressure, etc., can also be studied, which is vital in environmental science, marine science, etc.

Appendix A - RDFs and KBIs for different seawater systems

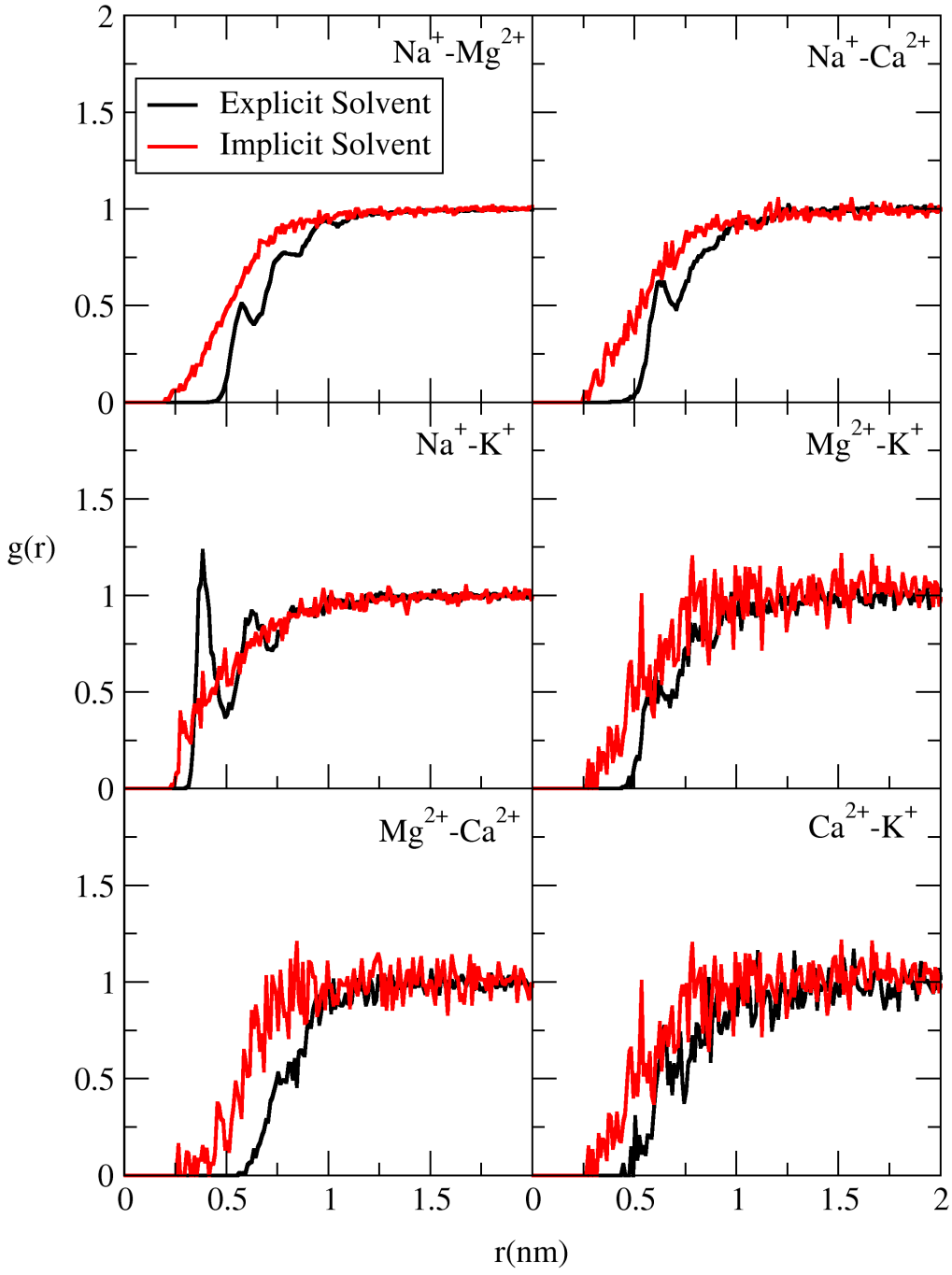

Appendix Figure A.1. The cation-cation RDFs of simulations of seawater using the implicit and explicit solvent model

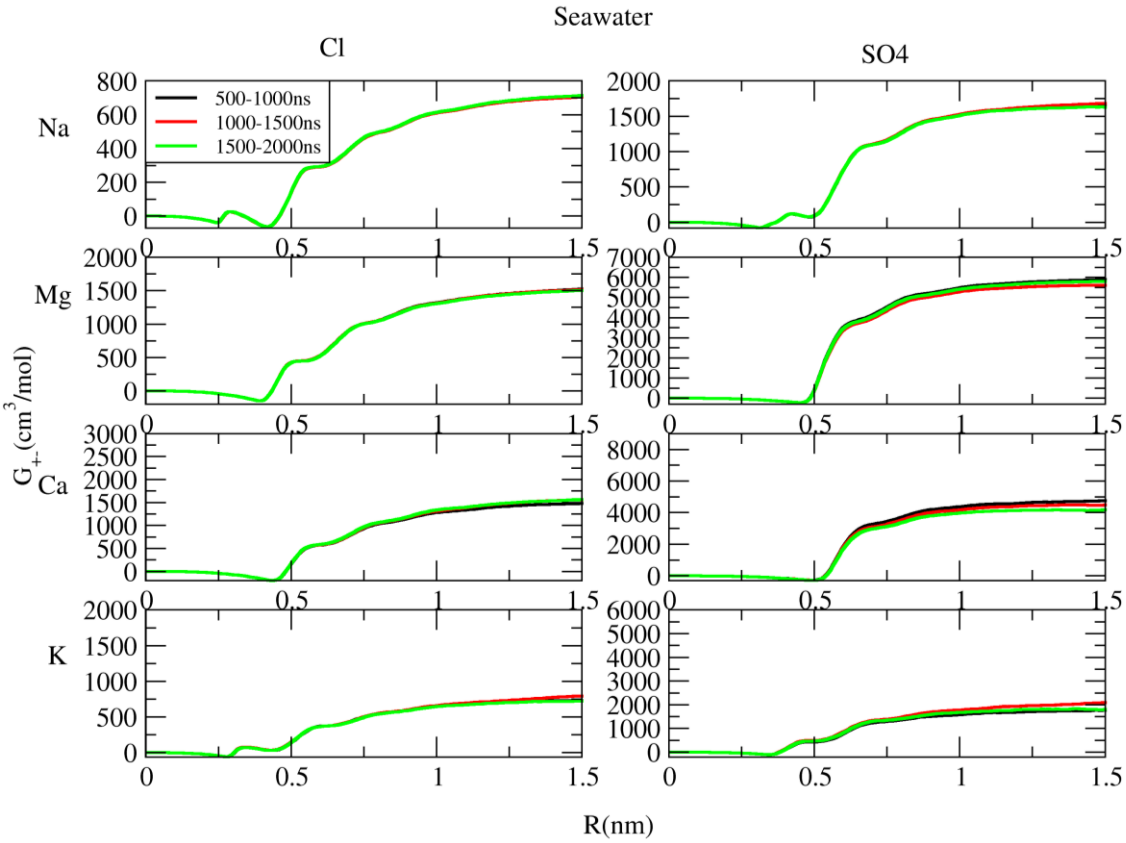

Appendix Figure A.2. The cation-anion KBIs with distance for the seawater system

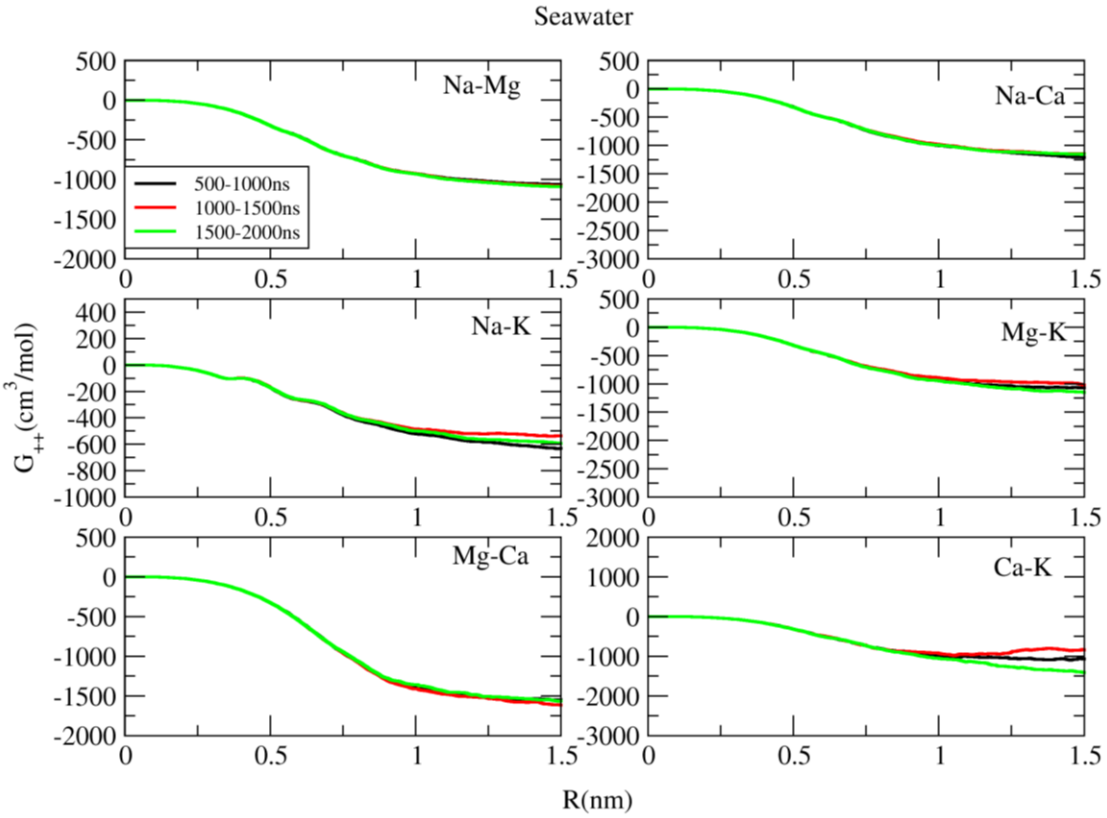

Appendix Figure A.3. The cation-cation KBIs with distance for the seawater system

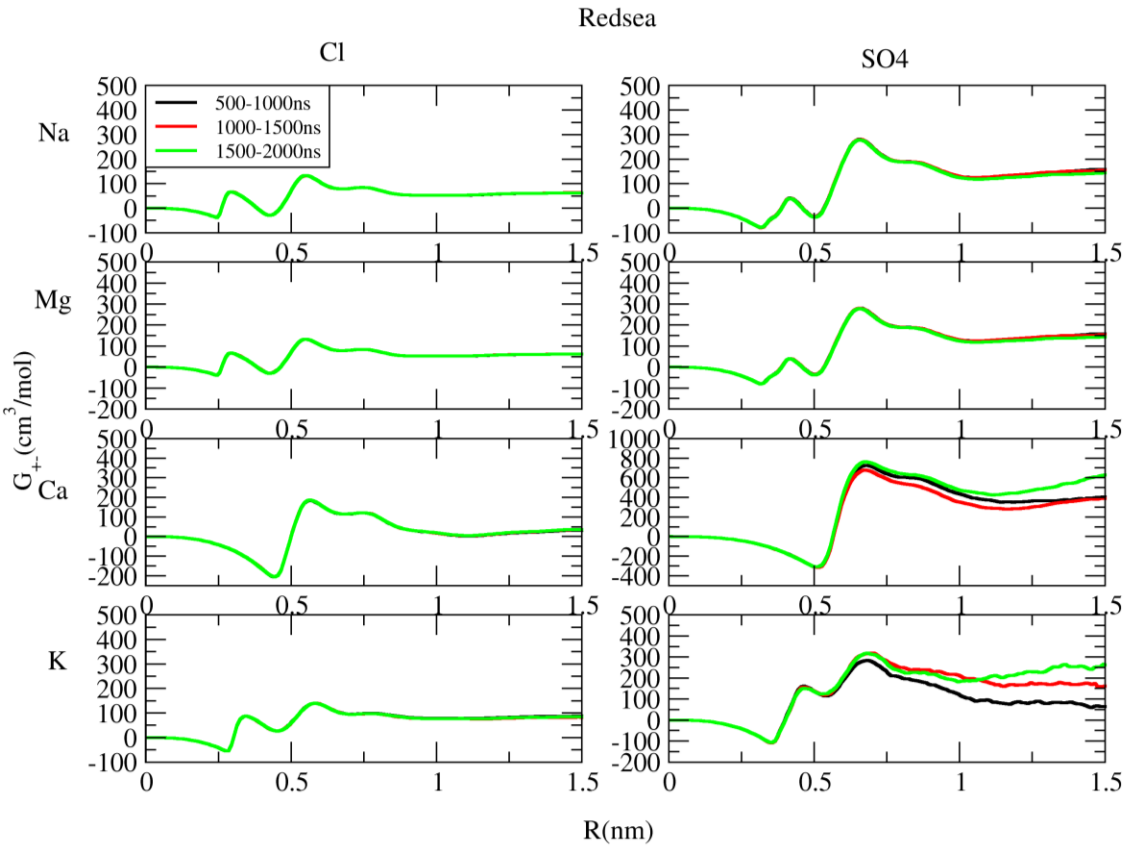

Appendix Figure A.4. The cation-anion KBIs with distance for the red seawater system

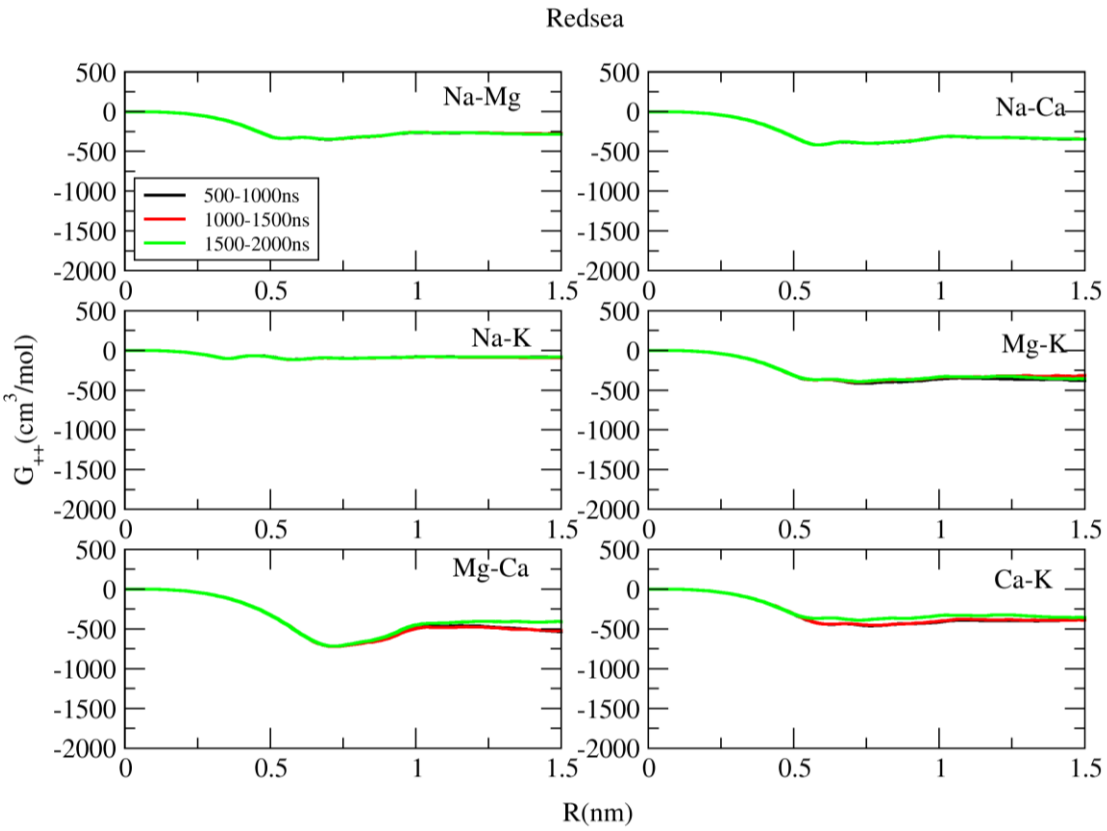

Appendix Figure A.5. The cation-cation KBIs with distance for the red seawater system

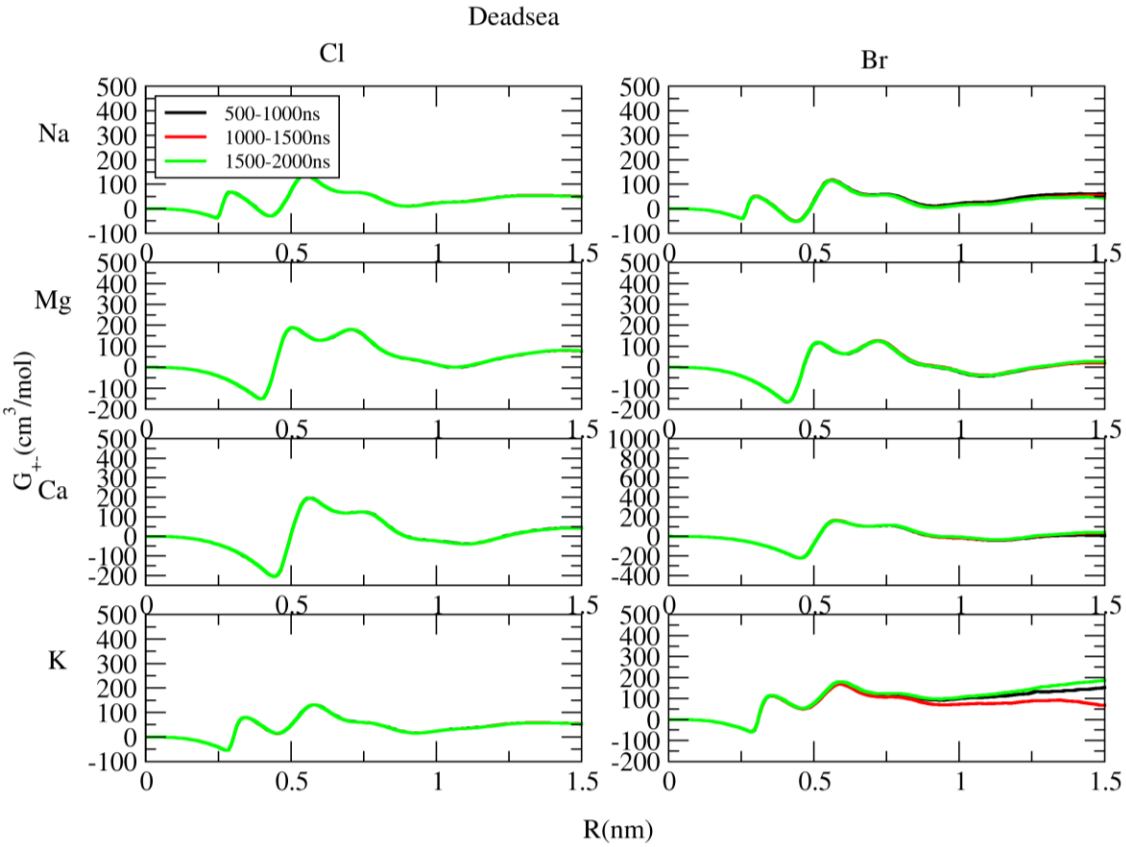

Appendix Figure A.6. The cation-anion KBIs with distance for the dead seawater system

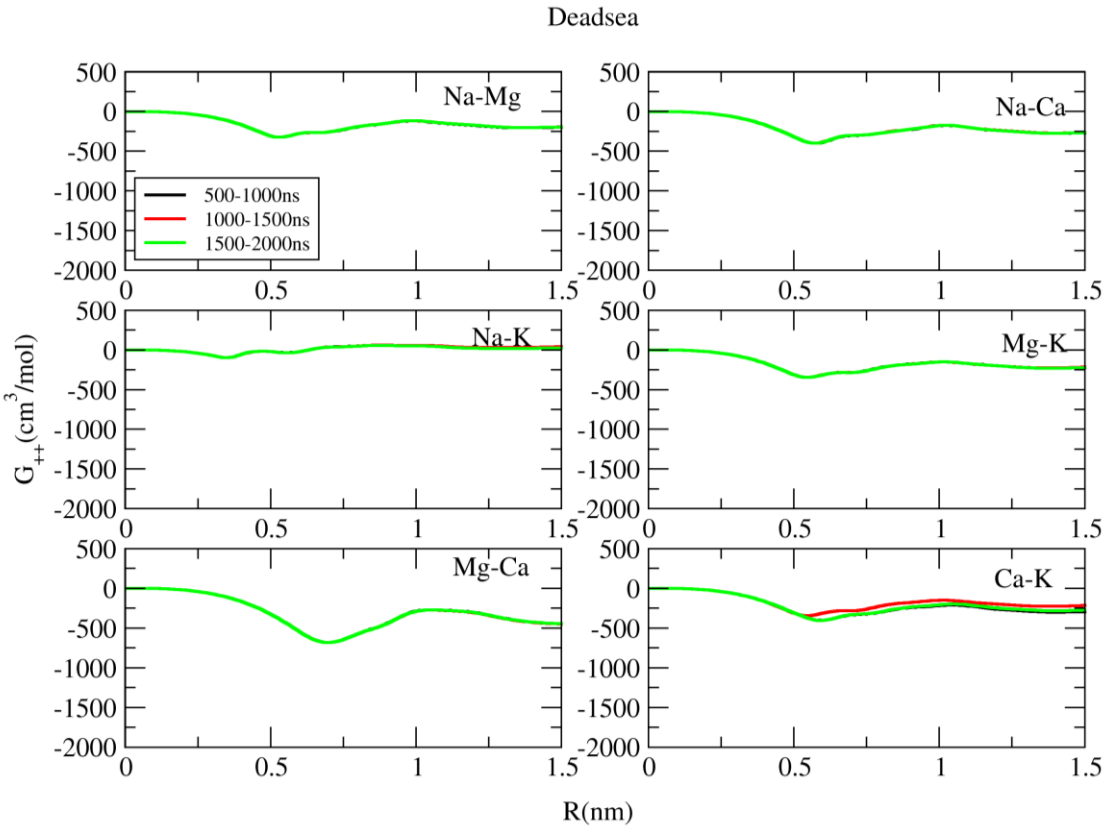

Appendix Figure A.7. The cation-cation KBIs with distance for the dead seawater system

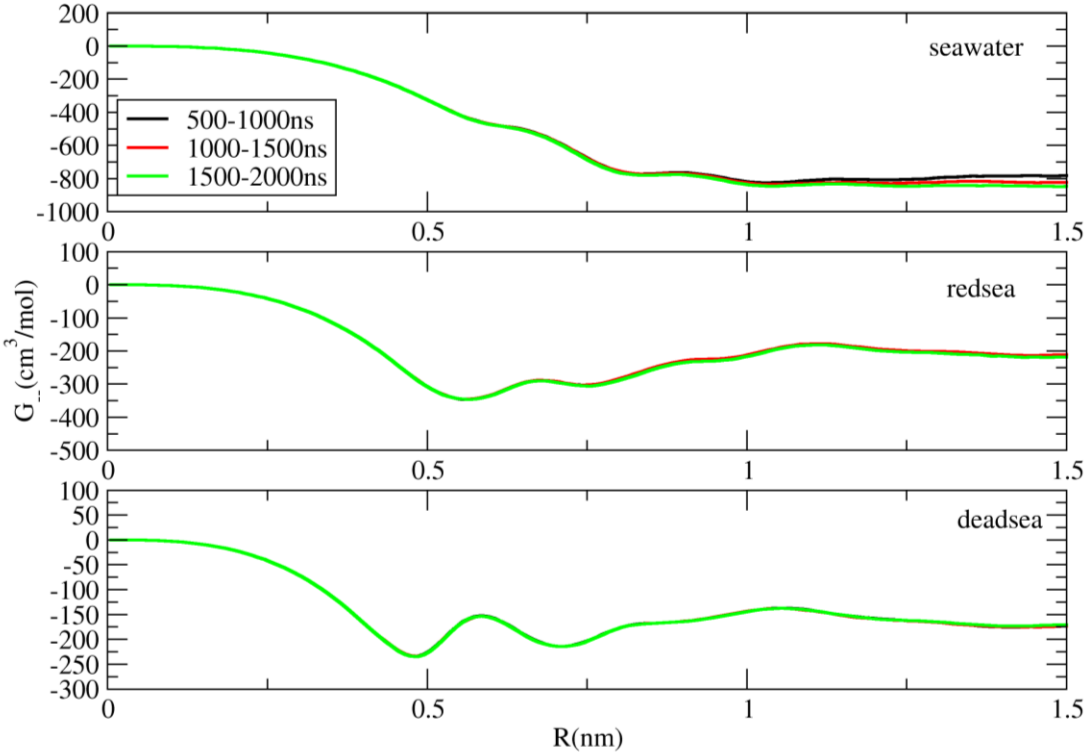

Appendix Figure A.8. The anion-anion KBIs with distance for regular seawater, red seawater, and dead seawater system